The Development of Accurate Stagnation Temperature Probes for Gas Turbine Applications

Clare Bonham

MEng

A Doctoral thesis submitted in partial fulfilment of the requirements for the award of Doctor of Philosophy

Loughborough University

November 17, 2015

Abstract

During gas turbine development testing, measurements of the gas-path stagnation temperature are used to characterise the engine running condition and establish individual engine component performance. These measurements are typically acquired using passively ventilated thermocouple probes, which are capable of achieving absolute stagnation temperature uncertainties of approximately $\pm 0.5\,\%$. Historically, this measurement accuracy has been considered adequate to evaluate gains in turbomachinery efficiency. However, realisable turbomachinery efficiency gains have recently become sufficiently small that an improvement in measurement accuracy is now required. This has resulted in the specification of a target absolute stagnation temperature uncertainty of $\pm 0.1\,\%$. The research presented in this thesis focusses on the development of a new stagnation temperature probe that will achieve a measurement uncertainty close to the target value. The new probe has been designed to utilise a thin-film platinum resistance thermometer (PRT) as the temperature sensitive element. For certain aspects of gas turbine engine testing, this type of sensor offers an improvement in measurement accuracy compared to a thermocouple. The new probe has also been designed for high temperature recovery performance, such that a low level of post-test measurement correction is required. This has been accomplished through the invention of a dual-skin stagnation tube, which reduces the impact of thermal conduction within the probe assembly. The performance of this dual-skin PRT probe has been investigated through a series of tests, which have been conducted in the newly developed Loughborough University probe aerodynamic calibration facility. Under engine representative conditions, the data indicate that the probe is capable of achieving absolute stagnation temperature uncertainties close to the $\pm 0.1\,\%$ target. This result has led to the dual-skin PRT probe being considered for use in future Rolls-Royce engine development programmes. A patent application for the probe has also been submitted.

Keywords: gas turbine engines, stagnation temperature, platinum resistance thermometry, temperature recovery factor

Table of Contents

List of Figures

List of Tables

Acknowledgements

The author would like to acknowledge contributions to this research from members of the Rolls-Royce Loughborough University Technology Centre in Combustion Systems Aero-thermal Processes. Particular recognition goes to Prof. Jon Carrotte and Dr. Steven Thorpe who supervised the work. Special thanks also go to Dr. Mark Brend for his constant encouragement and support. Additionally, the author would like to credit Rolls-Royce plc. for providing funding for this research. Particular gratitude is extended to Mark Erlund and Richard Stevenson for their technical advice and support.

Nomenclature

a	Sonic velocity
A	Area
A_E	Open area of flow restictor plate
A_N	Flow area at nozzle throat
A_{pipe}	Flow area in delivery pipeline
A_{vent}	Total cross sectional area of vent hole array
$A*$	Sonic nozzle area
A_1	Cross sectional area of sensing chamber
A_2	Total cross sectional area of inner vent hole array
A_3	Total cross sectional area of outer vent hole array
B_i	Systematic uncertainty in X_i
B_r	Systematic uncertainty in r
B_J	Systematic uncertainty in J
B_k	Elemental systematic uncertainty
C_D	Discharge coefficient
C_p	Specific heat at constant pressure
d	Probe diameter
d_2	Inner vent hole diameter
d_3	Outer vent hole diameter
f_D	Frictional resistance coefficient
F	Thrust
h	Convective heat transfer coefficient
i	Current
J	Generic measured variable
k	Thermal conductivity

l	Unsupported thermocouple length
L	Probe protrusion length
$\dot{m}$	Mass flow rate
$\dot{m_{fuel}}$	Fuel mass flow rate
M_{pipe}	Mach number in delivery pipeline
M_∞	Free-stream Mach number
N	Sample size
NPR	Nozzle pressure ratio
P_i	Random uncertainty in X_i
P_{ind}	Absolute probe indicated pressure
$P_{ind\,rel}$	Relative probe indicated pressure
P_J	Random uncertainty in J
$P_{o,\infty}$	Free-stream stagnation pressure
P_r	Random uncertainty in r
P_∞	Free-stream static pressure
PR	Compressor pressure ratio
PRT	Platinum resistance thermometer
q	Dynamic pressure
q_{cond}	Conductive heat flux
q_{conv}	Convective heat flux
q_{rad}	Radiant heat flux
q	Heat flux
r	Generic experimental result
R	Specific gas constant
$R_{p,P}$	Probe pressure recovery factor
$R_{p,T}$	Probe temperature recovery factor
R_T	Resistance at T
$R_{w,T}$	Wall temperature recovery factor
R_{0^oC}	Resistance at 0^oC
Re_∞	Free-stream Reynolds number based on probe diameter
S	Sutherland's constant
S_{AB}	Effective Seebeck coefficient
S_X	Sample standard deviation
$s.f.c$	Specific fuel consumption
t	Time

T	Static temperature
T_{gas}	Gas recovery temperature
T_j	Thermocouple junction temperature
$T_{j\,ad}$	Adiabatic thermocouple junction temperature
T_{ind}	Probe indicated temperature
$T_{initial}$	Initial temperature ($t = 0$)
$T_{o,\infty}$	Free-stream stagnation temperature
$T_{recovery}$	Recovery temperature
T_{ref}	Reference temperature
T_w	Adiabatic wall temperature
T_{wall}	Stagnation tube wall temperature
$T_{0,in}$	Compressor inlet temperature
$T_{0,out}$	Compressor outlet temperature
T_∞	Free-stream static temperature
U_r	Expanded uncertainty in r
U_{95}	Expanded uncertainty at 95 % confidence level
V	Velocity
V_A	Voltage induced in thermocouple wire A
V_B	Voltage induced in thermocouple wire B
V_{net}	Net voltage across thermocouple wires A and B
V_1	Gas velocity in sensing chamber
V_2	Gas velocity through inner vent hole array
V_3	Gas velocity through outer vent hole array
V_∞	Free-stream velocity
W	Total number of elemental systematic uncertainties
$\overline{X}$	Sample mean
X_i	Single measured variable used in derivation of r
X_J	Generic measurement of J
X_s	Single measurement from sample
X_{true}	True value of X_J

Greek symbols

α	Constant
β	Systematic error
γ	Ratio of specific heats
δr	Overall uncertainty in r
$\delta r X_i$	Uncertainty in r due to uncertainty in X_i
δX_i	Uncertainty in X_i
ΔP	Stagnation pressure loss
ΔP_{tot}	Overall stagnation pressure loss
ϵ	Random error
λ	Temperature recovery factor (adiabatic)
μ	Parent population mean
μ_∞	Free-stream gas viscosity
μ_{ref}	Reference viscosity
η	Isentropic efficiency
η_p	Polytropic efficiency
ρ	Density
ρ_∞	Free-stream gas density
σ	Parent population standard deviation
σ_B	Boltzman's constant
ξ	Thermocouple surface emissivity
ζ	Constant

CHAPTER 1

Introduction

1.1 Background to research

During the development phase of a gas turbine engine, a whole-engine test campaign is conducted using an instrumented working prototype. The primary objective of this campaign is to verify that the performance of the engine conforms to the intended specification. This is accomplished through the determination of a number of important performance parameters, including the thrust specific fuel consumption (s.f.c). This characterises the rate of fuel burn per unit thrust. Compliance with the target s.f.c is crucial to the commercial success of the engine, since an aircraft operator will generally favour the engine option with the lowest estimated fuel consumption. The cost of fuel represents between 15 % and 20 % of total aircraft running costs, so even a small reduction in s.f.c can facilitate significant cost savings (Rolls-Royce, 2005). Compliance with the target s.f.c is also important for controlling the environmental impact of the engine, since the emission of harmful combustion products is directly related fuel burn rate. Firm

restrictions are placed on engine emissions, with further significant reductions in carbon dioxide (75 %) and nitrous oxide (90 %) production required by 2050 (Dareck *et al.*, 2011). Accordingly, engine manufacturers must invest considerable time and resource in reducing s.f.c.

The s.f.c is governed by the overall efficiency of the engine, which is related to the efficiencies of individual components of turbomachinery (compressor and turbines). During whole-engine test campaigns, major importance is therefore placed on assessing the efficiency of each turbomachinery component. This information is used to establish whether the components are operating as intended, and thus forms the basis on which design refinements are pursued. These refinements can facilitate potential improvements in efficiency and consequently reductions in s.f.c. In the past, extensive engine development programs have delivered significant gains in turbomachinery efficiency. This has been accomplished through a combination of meticulous rig testing and sophisticated computational modelling. Today, the remarkable success of these programs has placed limits on further realisable efficiency gains. As a consequence, engine manufacturers now require the capability to gauge small (≤ 1 %) increments of turbomachinery efficiency during test campaigns.

The efficiency of each turbomachinery component is derived from measurements of the absolute gas-path stagnation pressure and temperature. Generally, the stagnation temperature is measured with a passively ventilated thermocouple probe, whilst the stagnation pressure is measured with a Pitot probe. These devices facilitate the measurement of stagnation quantities by decelerating the flow to a fraction of the approach velocity, which is typically in the high-subsonic Mach number range. The necessary accuracy of the gas-path stagnation measurements is dictated by the smallest increment of component efficiency that must be

resolved. To enable the assessment of component efficiencies to an uncertainty of $\pm 0.5\,\%$, an absolute stagnation temperature uncertainty of $\pm 0.1\,\%$ is required, together with an absolute stagnation pressure uncertainty of $\pm 0.05\,\%$ (see sections 2.1.4 and 2.1.5). These figures currently represent the target accuracies for gas-path stagnation measurements during whole-engine test campaigns.

At engine inlet conditions ($T_{o,\infty} \approx 300\,K$), the $\pm 0.1\,\%$ target uncertainty for absolute stagnation temperature measurements corresponds to an uncertainty of approximately $\pm 0.3\,K$. In an engine test environment, such a low temperature measurement uncertainty is extremely difficult to achieve. Partly, this is related to problems that affect the measurement performance of the temperature sensor on the engine test-bed. These include static calibration drift and electrical noise contamination. Further complexity is introduced by the probe temperature recovery performance, which causes a deficit between the measured temperature and the *true* stagnation temperature. This is governed by temperature recovery effects of the flow over the sensor, together with installation effects such as conduction and radiation. These two difficulties presently limit the achievable uncertainty in absolute gas-path stagnation temperature measurements to approximately $\pm 0.5\,\%$ [1]. To realise the target uncertainty of $\pm 0.1\,\%$, significant advances in stagnation temperature measurement capability are therefore required.

1.2 Research objective

The objective of this research is to develop a new stagnation temperature probe for gas turbine engines that will achieve an absolute stagnation temperature un-

[1] Private communication: Mark Erlund, Measurement Specialist, Rolls-Royce plc.

certainty close to the $\pm 0.1\,\%$ target. This objective will be accomplished by addressing two significant weaknesses of existing stagnation temperature probe designs. Firstly, the performance of the temperature sensor will be improved to alleviate problems including static calibration drift and electrical noise contamination. Secondly, the temperature recovery performance of the probe will be enhanced such that the measured temperature is closer to the *true* stagnation temperature. The combination of these two design advances will result in a significant improvement in stagnation temperature measurement accuracy.

The new stagnation temperature probe is primarily intended for application in low temperature regions of the engine, where the target uncertainty of $\pm 0.1\,\%$ is most difficult to achieve. These regions encompass the engine inlet and the low pressure compression system. As a consequence, there is no requirement for the probe to possess a temperature capability in excess of $390\,K$ (see Table 2.1). However, the probe must be designed to be sufficiently compact, robust and reliable for use in a harsh engine environment.

1.3 Thesis overview

This thesis captures the work undertaken towards the development of a more accurate stagnation temperature probe for use in gas turbine engines. Chapter 2 introduces the subject of stagnation temperature measurement in high-velocity flows, with particular emphasis on gas turbine applications. Also included in chapter 2 is a review of relevant literature, which is focussed on the issues affecting the temperature recovery performance of different probe designs. Described in chapter 3 are the facilities that have been developed as part of this work for the static and aerodynamic calibration of stagnation temperature and pressure

probes. The important matter of establishing uncertainties in the measurements acquired in these facilities is considered in chapter 4. Discussed in chapters 5 and 6 are the issues of temperature sensor measurement performance and probe temperature recovery performance, both of which have an important effect on stagnation temperature measurement accuracy. Chapter 7 presents the development of a new probe design that addresses both of these issues in order to achieve more accurate stagnation temperature measurements. Finally, chapter 8 presents the conclusions of this work and highlights opportunities for further research.

1.4 Publications

The work described in this thesis has resulted in the preparation of a journal article and the submission of a patent application. The work has additionally been presented at two international conferences. Details of each of these publications are provided below:

- Bonham C, Thorpe S J, Erlund M N, Stevenson R D, Stagnation temperature measurement using thin-film platinum resistance sensors, Meas. Sci. Technol. 25, 2014, 015101 (16pp)

- Bonham C, Thorpe S J, Erlund M N, Improved total temperature and pressure probe, 2015, 5113 VJAY

- Bonham C, Thorpe S J, Gas-path performance measurements using combination stagnation pressure and temperature probes, 6th EVI-GTI International Gas Turbine Instrumentation Conference, 2013, Baden, EVI2013-015

- Bonham C, Thorpe S J, The design of gas-path instrumentation for high

probe recovery performance, 4th Joint EVI-GTI PIWG International Gas Turbine Instrumentation Conference, 2012, Florence, EVI2012-011

CHAPTER 2

Stagnation Temperature Measurement

This chapter introduces the topic of gas-path stagnation temperature measurement in gas turbine engines. Firstly, attention is focussed on conventional methods of gas-path temperature measurement, which involve the use of fixed intrusive probes. The design of a typical probe is presented, alongside details of the flow conditions and installation arrangement at each measurement location. Subsequently, the phenomena that affect the accuracy of stagnation temperature measurements are identified and explained. These phenomena are related to the measurement performance of the temperature sensor and the temperature recovery performance of the probe assembly. Finally, consideration is given to the use of post-test measurement corrections as a means of improving stagnation temperature accuracy. This necessitates the development of detailed probe models, or the execution of probe aerodynamic calibrations.

2.1 Gas-path temperature measurement

In gas turbine engines, measurements of the gas-path temperature are acquired in order to assess the efficiency of individual components of turbomachinery. Sections 2.1.1 to 2.1.5 describe some practical aspects of gas-path stagnation temperature measurement, including the probe design, measurement location and present accuracy level.

2.1.1 Static and stagnation properties

For gases moving at velocities in excess of Mach 0.25, there are two temperatures that are of significance (Hottel and Kalitinsky, 1945). Firstly the static temperature, T_∞, which is indicated by a probe that moves at the same velocity as the gas. Secondly the stagnation temperature, $T_{o,\infty}$, which is indicated by a probe that stagnates the gas via an adiabatic process (idealised reversible process with no heat transfer). The static temperature represents the actual temperature of the gas. It is a measure of the kinetic energy that is associated with random motion of the constituent molecules. The stagnation temperature characterises the total energy level of the gas. It is a measure of both the molecular kinetic energy and the directed kinetic energy that is associated with bulk gas motion. The static and stagnation temperatures are related through equation 2.1, which is derived from the 1-D steady flow energy equation under the assumptions of no heat transfer, no work transfer and no change in potential energy (Anderson, 1990). The velocity term in equation 2.1 is sometimes called the dynamic temperature, which is a measure of the directed kinetic energy of the gas.

$$T_{o,\infty} = T_{\infty} + \frac{{V_{\infty}}^2}{2C_p} \tag{2.1}$$

In gas turbine engines, flow velocities are generally in the high-subsonic Mach number range ($\geq$ Mach 0.6). In attempting to measure the gas-path condition, it is therefore necessary to distinguish between the static and stagnation temperature. Fixed intrusive probes represent the current state of the art for gas-path measurements in gas turbine engines (Saravanamuttoo, 1990). Static temperature measurements are clearly not feasible with these probes, due to the requirement for the probe to travel at the same velocity as the gas. Attention is consequently focussed on stagnation temperature measurements, which are achievable with stationary probes that attempt to stagnate the gas adiabatically.

2.1.2 Probe design

Figure 2.1 shows a cross-sectional diagram of a probe that is commonly used to acquire stagnation temperature measurements in gas turbine engines. The probe consists of a thermocouple sensor that is surrounded by a passively ventilated stagnation tube. Typically, either a 'K' or 'N' type thermocouple sensor is chosen due to their high maximum operating temperature of approximately $1600\,K$ (Massini *et al.*, 2010). This allows the sensor to be successfully utilised in a variety of different gas path measurement locations (see Table 2.1). The stagnation tube is normally constructed from a hollow metallic cylinder, with a diameter of less than $5\,mm$ (Saravanamuttoo, 1990). The stagnation tube usually features a number of rearward vent holes, which are used to promote a continuous flow over the thermocouple sensor. This type of probe is sometimes referred to as a Kiel head, owing to similarities with the total-head meters originally developed

by Kiel (1935).

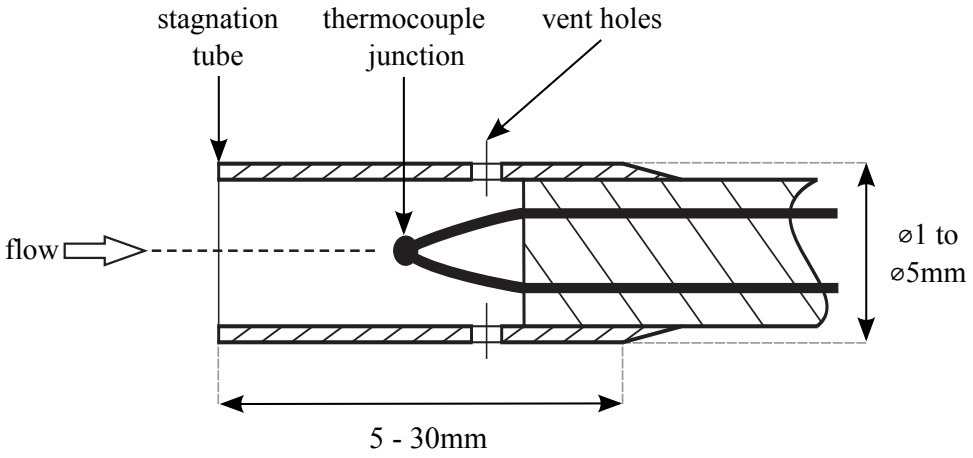

Figure 2.1: A schematic diagram of a stagnation temperature probe incorporating a thermocouple sensor.

When inserted into the gas-path, the probe is positioned such that the inlet of the stagnation tube is aligned with the free-stream flow direction. As gas enters the stagnation tube it undergoes a rapid deceleration, eventually passing over the thermocouple sensor at a sufficiently low ($\leq$ Mach 0.25) velocity that the probe can indicate a temperature close to the gas stagnation temperature (Markowski and Moffatt, 1948). For a given free-stream condition, the gas velocity inside the probe is determined by the inlet-exit area ratio of the stagnation tube. This must be carefully selected in order to attain a rapid response to changes in gas temperature, whilst also creating an environment in which near-stagnation temperatures can be measured. Any discrepancy between the probe indicated temperature and the gas stagnation temperature can be characterised using the probe temperature recovery factor, $R_{p,T}$, which is discussed further in section 2.2.2. The temperature recovery factor accounts for the inability of the probe to stagnate the gas adiabatically, as well as for probe heat transfer effects that can also influence the indicated temperature.

To facilitate higher spatial measurement resolution, stagnation temperature probes

are often converted into combined stagnation pressure and temperature measuring devices. This conversion simply requires the installation of a Pitot tube alongside the thermocouple sensor (see Figure 2.2). In order to accommodate the Pitot tube, combination probes generally utilise oval stagnation tubes. Although this causes an overall increase in size, combination probes remain more compact in comparison with separate stagnation pressure and temperature probes.

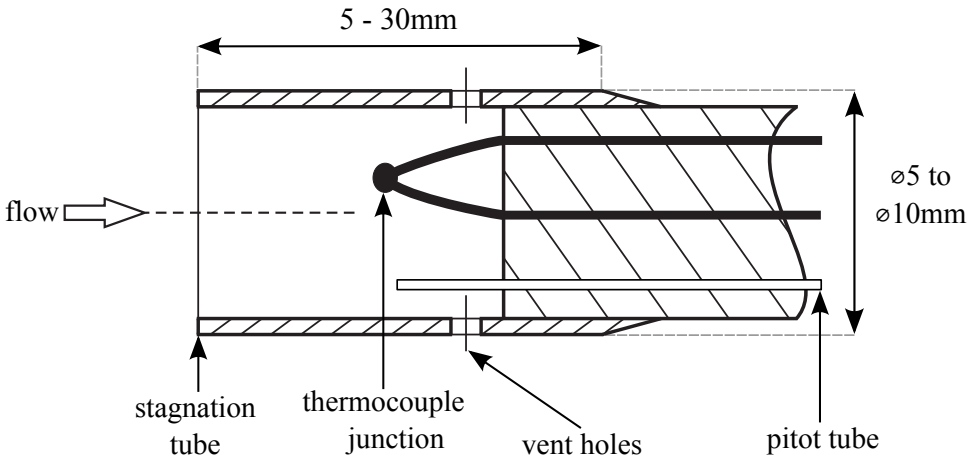

Figure 2.2: A schematic diagram of a combined stagnation pressure and temperature probe.

2.1.3 Measurement location

During development testing, gas-path stagnation temperature measurements are acquired at various axial locations within a gas turbine engine. Figure 2.3 indicates the typical measurement locations in a 3-shaft turbofan, which coincide with the inlet/outlet of the main components of turbomachinery. At each location, probes are installed across the height of the engine annulus at several radial positions.

Across the different gas-path measurement locations, there are significant variations in local flow conditions. For example, pressures and temperatures increase

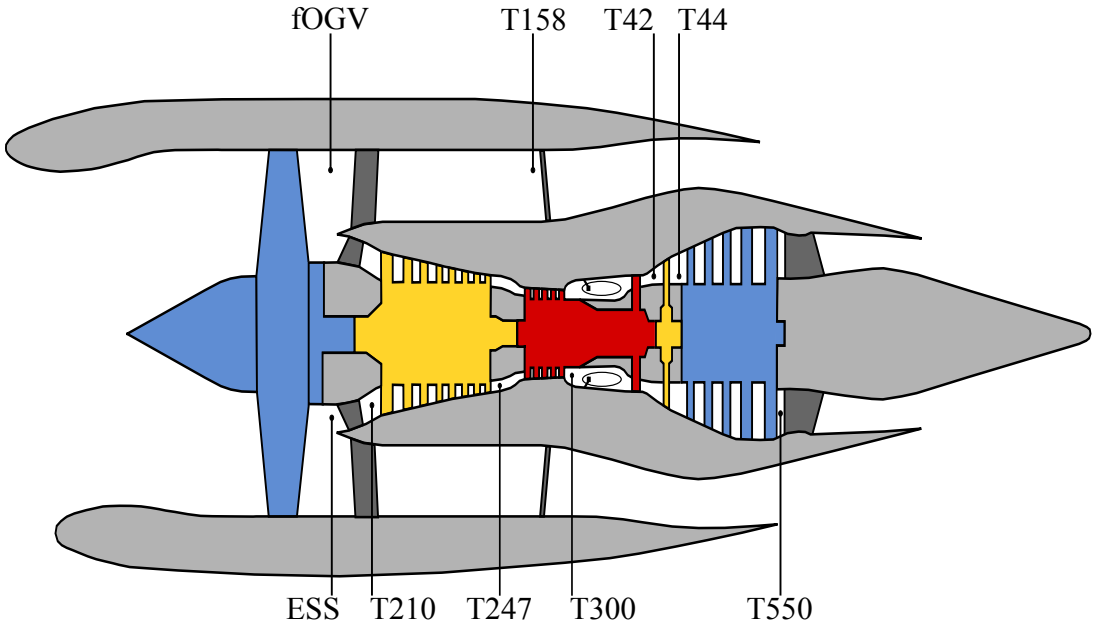

Figure 2.3: Typical gas-path stagnation temperature measurement locations in a 3-shaft turbofan (showing standard Rolls-Royce nomenclature).

from ambient conditions at fan inlet, to values in excess of 55 bar and 1020 K at core compressor outlet. Similarly, Mach numbers differ from values > 1 at fan outlet, to approximately 0.3 in the combustor. Table 2.1 attempts to summarise the flow conditions local to each measurement location indicated in Figure 2.3. From these conditions, it is apparent that no single stagnation temperature probe is suitable for all measurement locations within the engine (Scadron *et al.*, 1952).

Component	Fan	Compressor	Combustor	Turbine
Temperature (K)	230 - 390	270 - 1020	870 - 2220	1820 - 1320
Pressure (bar)	0.5 - 1.5	0.75 - 55	40 - 54	50 - 7
Mach number	< 1	< 1	≈ 0.3	< 1
Measurement location	ESS fOGV T158	T210 T247 T300	N/A	T42 T44 T550

Table 2.1: Temperatures, pressures and Mach numbers at typical gas-path measurement locations in a 3-shaft turbofan (Langley *et al.*, 2012).

Variations also occur in the method used to install stagnation temperature probes at different gas-path measurement locations. At fan outlet, probes are bonded directly on to the surface of the fan outlet guide vane (fOGV) and engine section stator (ESS). Elsewhere within the compression system, probes are arranged along the shafts of aerodynamically profiled bodies, known as rakes. These rakes are inserted into the engine via casing-mounted bosses. Alternatively within the turbine, probes are installed directly onto the leading edge of nozzle guide vanes. Examples of stagnation temperature probes in surface-bonded (a) and rake-mounted (b) configurations are shown in Figure 2.4.

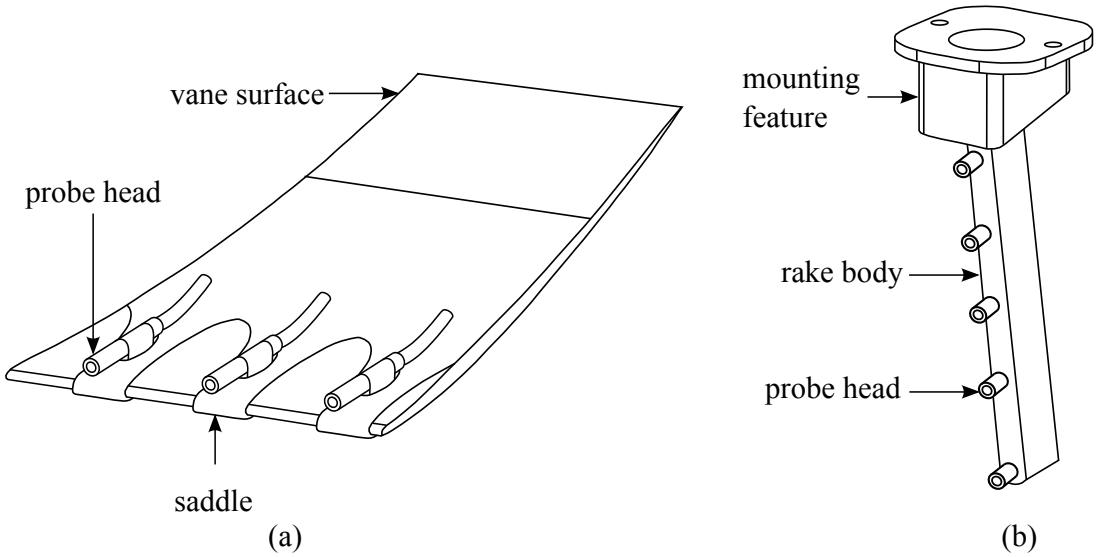

Figure 2.4: Schematic diagrams of stagnation temperature probes in surface-bonded (a) and rake-mounted (b) installations.

2.1.4 Turbomachinery efficiency

An important use of gas-path stagnation temperature measurements is in the determination of turbomachinery efficiency. For example, the isentropic efficiency of a compression system can be derived from measurements of the stagnation temperature at the inlet, $T_{o,in}$, and outlet, $T_{o,out}$, of the system (equation 2.2).

$$\eta = \frac{T_{o,in}}{T_{o,out} - T_{o,in}} \left[PR^{\frac{\gamma-1}{\gamma}} - 1 \right] \tag{2.2}$$

From this expression, it is clear that the accuracy of the isentropic efficiency is sensitive to uncertainties in both the inlet stagnation temperature and the overall stagnation temperature rise. The extent of this sensitivity is indicated in Figure 2.5, which shows the impact of an uncertainty in the inlet stagnation temperature as a function of pressure ratio, PR. Absolute stagnation temperature uncertainties of $\pm 0.5\%$ and $\pm 0.1\%$ have been selected, since these values represent the currently achievable and future targeted (see section 2.1.5) accuracies for gas-path measurements [1].

In Figure 2.5, the largest changes in isentropic efficiency are apparent at low pressure ratios. This result has an important implication for single stage fans, which typically have pressure ratios in the range 1.4-1.8 (3-shaft turbofan). At these pressure ratios, the currently achievable $\pm 0.5\%$ uncertainty in absolute stagnation temperature results in a $\pm 3\%$ uncertainty in derived efficiency. This uncertainty causes appreciable difficulties in determining whether the fan is operating as intended, or whether design refinements are required. For core compressors, pressure ratios are generally in the range 2.5-6 (3-shaft turbofan). At these pressure ratios, a $\pm 0.5\%$ uncertainty in absolute stagnation temperature results in an uncertainty of approximately $\pm 1\%$ in derived efficiency. Although this value is significantly lower than the fan uncertainty, challenges remain in determining whether the core compressors are operating as intended. This is a consequence of successes in past engine development programs, which have limited further realisable turbomachinery efficiency gains to $< 1\%$.

[1] Private communication: Mark Erlund, Measurement Specialist, Rolls-Royce plc.

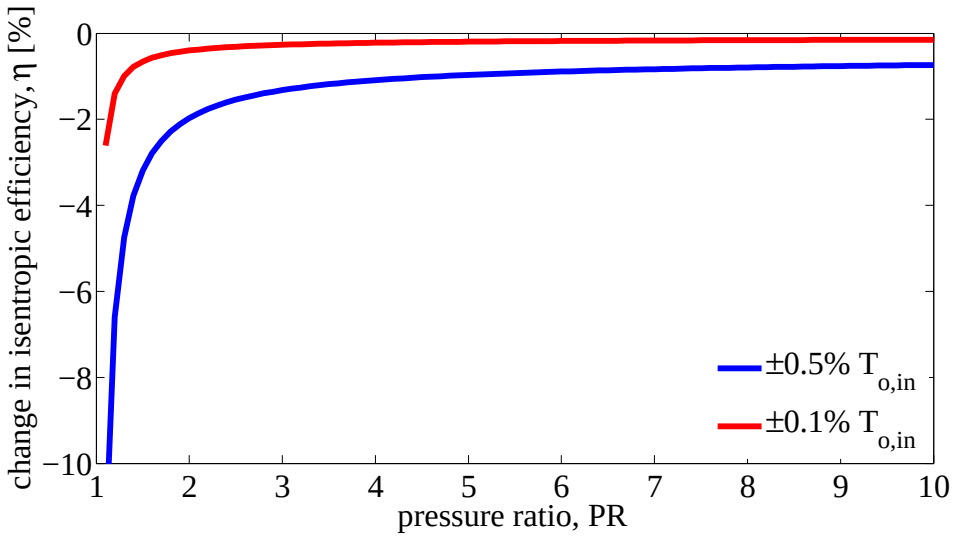

Figure 2.5: A graph showing the impact of ±0.5% and ±0.1% uncertainties in absolute inlet stagnation temperature on the derived isentropic efficiency of a compression system (based on equation 2.2 with $T_{o,in} = 300K$ and $\eta_p = 0.85$).

2.1.5 Specific fuel consumption

The overall efficiency of a gas turbine engine is related to the efficiency of the individual components of turbomachinery. The overall efficiency governs the engine s.f.c, which represents the rate of fuel burn per unit thrust (equation 2.3).

$$s.f.c = \frac{\dot{m_{fuel}}}{F} \tag{2.3}$$

Engine manufacturers make considerable efforts to reduce s.f.c, since this lessens the operating cost and environmental impact of the engine (see section 1.1). These efforts have resulted in a desire to reduce the uncertainty associated with assessments of turbomachinery efficiency to ±0.5%. With these more accurate efficiency assessments, present difficulties in identifying under-performing turbomachinery components will be eased (see section 2.1.4). Targeted design refinements will consequently become feasible, leading to potential efficiency enhancements

and sought after reductions in s.f.c.

To facilitate the evaluation of turbomachinery efficiency to an uncertainty of $\pm 0.5\%$, the uncertainty in measurements of absolute gas-path stagnation temperature must be improved to $\pm 0.1\%$. This is evidenced by the data in Figure 2.5, which shows the impact of an uncertainty in inlet stagnation temperature on the isentropic efficieny of a compression system. For compressor pressure ratios in the range 1.4-1.8 (representative of a single stage fan in a 3-shaft turbofan), a $\pm 0.1\%$ uncertainty in absolute stagnation temperature results in the desired $\pm 0.5\%$ uncertainty in derived compressor efficiency. This is one-sixth of the value that is currently achievable with $\pm 0.5\%$ uncertainty in absolute stagnation temperature (see section 2.1.4).

For fan inlet conditions ($T_{o,\infty} \approx 300\,K$), the target absolute stagnation temperature uncertainty of $\pm 0.1\%$ corresponds to a measurement uncertainty of approximately $\pm 0.3\,K$. In an engine test environment, existing probes cannot attain this accuracy due to problems that affect the measurement performance of the temperature sensor and the temperature recovery performance of the probe assembly. These problems presently restrict the achievable uncertainty in measurements of absolute gas-path stagnation temperature to approximately $\pm 0.5\%$ [2]. Research is therefore required to develop new stagnation temperature probes, which can realise improved measurement uncertainties close to $\pm 0.1\%$.

[2]Private communication: Mark Erlund, Measurement Specialist, Rolls-Royce plc.

2.2 Measurement accuracy

The accuracy of gas-path stagnation temperature measurements is sensitive to a number of well documented phenomena (see for example Moffat, 1962). These phenomena are most appropriately grouped into two categories: those impacting the measurement performance of the temperature sensor (section 2.2.1), and those impacting the temperature recovery performance of the probe assembly (section 2.2.2).

2.2.1 Temperature sensor performance

In gas turbine engines, measurements of the gas-path stagnation temperature are generally acquired using a thermocouple sensor (see section 2.1.2). In part, the measurement accuracy is determined by the ability of the sensor to provide signals that can be correctly related to the junction temperature. This temperature sensor performance is sensitive to three distinct phenomena, which include: (1) the accuracy of the measuring circuit, (2) the transmitted signal integrity, and (3) the thermocouple static calibration retention.

2.2.1.1 Measuring circuit accuracy

When a thermocouple sensor is exposed to a temperature gradient, an electromotive force (e.m.f) is generated due to the Seebeck effect (Seebeck, 1823). This e.m.f is proportional to the temperature difference along the thermocouple, between the measuring junction and the reference junction (see section 5.2). To determine the measuring junction temperature, knowledge of the reference junction temperature must therefore be acquired. On an engine test-bed, this is typ-

ically obtained using an independent resistive temperature device (RTD), which is mounted within the thermocouple measuring instrument. The accuracy of the temperature indicated by the RTD must consequently influence the accuracy of the derived measuring junction temperature. This influence may prove significant, since temperature discrepancies of up to $2.5\,K$ have been reported between the reference junction and the RTD [3]. In order to realise the highest accuracy levels, the reference junction may alternatively be maintained at a constant known temperature (typically $273.15\,K$) using a fixed-point cell (Bentley, 1998b). However, this approach is uncommon in an engine test environment, since it introduces additional cost and complexity to the measurement system.

2.2.1.2 Transmitted signal integrity

The thermocouple sensor is renowned for possessing a weak thermoelectric response, which can compromise the accuracy of the derived measuring junction temperature. For example, the 'N' type device commonly employed in gas turbine engine testing exhibits a sensitivity of approximately $40\,\mu V/K$ (Bentley, 1998b). The transmitted signal can therefore become readily corrupted by electrical noise from the test environment. To prevent electrical noise from influencing the accuracy of the derived measuring junction temperature, it would be advantageous to utilise a thermocouple with a stronger thermoelectric response. Unfortunately, the maximum sensitivity displayed by a thermocouple is approximately $70\,\mu V/K$ for an 'E' type device (Bentley, 1998b). To achieve higher sensitivities, alternative methods of temperature measurement (e.g. resistive techniques) must consequently be explored.

[3] Private communication: Mark Erlund, Measurement Specialist, Rolls-Royce plc.

2.2.1.3 Static calibration retention

Prior to installation in a gas turbine engine, the thermoelectric response of a thermocouple must be characterised via a process known as static calibration. In this process, the e.m.f generated by the thermocouple is measured under known temperature conditions, and a relationship derived between the two parameters. Unfortunately, the static calibration is dependent the thermoelectric properties of the thermocouple wire, which can be modified by exposure to high stress or temperature (Childs *et al.*, 2000). Following installation and operation in an engine environment, the static calibration of the thermocouple can therefore become invalid. To prevent this invalidity influencing the accuracy of the derived measuring junction temperature, regular re-calibration of the thermocouple is ideally required. However, this cannot be practically accommodated during demanding engine test campaigns.

2.2.2 Probe temperature recovery performance

In gas turbine engines, the thermocouple sensors used to acquire gas-path stagnation temperature measurements are commonly mounted within passively ventilated stagnation tubes (see section 2.1.2). The measurement accuracy is therefore dependent on the ability of the stagnation tube to create an environment where the thermocouple junction can attain the gas stagnation temperature (Moffat, 1962). This is impacted by two distinct phenomena. Firstly, junction temperature recovery effects, which are associated with the inability of the probe to stagnate the gas adiabatically. Secondly, heat transfer effects, which are related to conduction, convection and radiation within the probe assembly.

The influence of these two phenomena on the junction temperature is characterised by the probe temperature recovery factor, $R_{p,T}$. This is defined by equation 2.4, which is a function of the probe indicated temperature, T_{ind}, as well as the static, T_∞, and stagnation, $T_{o,\infty}$, temperatures of the gas. When the discrepancy between the probe indicated temperature and the gas stagnation temperature is small, a probe temperature recovery factor close to the maximum value of unity is obtained ($R_{p,T} \approx 1$).

$$R_{p,T} = \frac{T_{ind} - T_\infty}{T_{o,\infty} - T_\infty} \tag{2.4}$$

2.2.3 Temperature recovery effects

Due to ventilation of the stagnation tube, the gas inside the sensing chamber is not stagnated and instead flows over the thermocouple with some residual velocity. As a consequence of this velocity, the temperature of the gas within the sensing chamber is unable to attain the stagnation temperature, $T_{o,\infty}$. In seeking to acquire stagnation temperature measurements, temperature recovery effects associated with flow over the thermocouple must therefore be considered.

When gas within the sensing chamber passes over the thermocouple, a boundary layer is formed where shear forces reduce the flow velocity from the outboard value to zero at the surface. This velocity reduction is associated with a process of viscous dissipation, whereby the directed kinetic energy of the gas is transformed into thermal energy. This energy transformation results in a re-distribution of temperature across the boundary layer. High temperatures are established in regions of low kinetic energy (near the surface), while low temperatures are established in regions of high kinetic energy (outboard of the surface). The velocity

and temperature profiles formed across a generic boundary layer are illustrated in Figure 2.6.

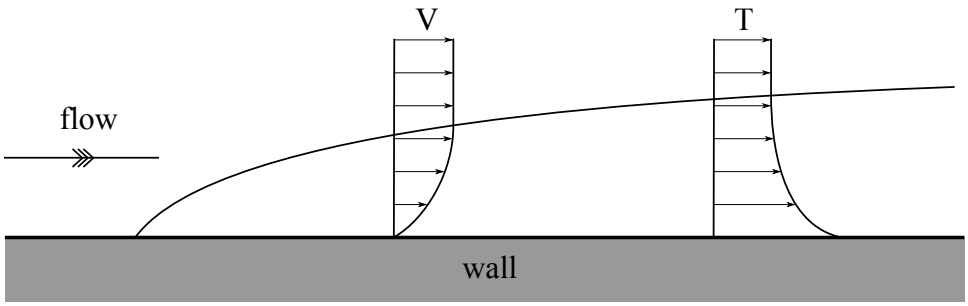

Figure 2.6: Velocity and temperature profiles formed across a generic boundary layer.

At the surface of the thermocouple, it is conceivable that the directed kinetic energy of the gas could be completed converted into thermal energy as a consequence of viscous dissipation (Hottel and Kalitinsky, 1945). In an adiabatic case, the local gas recovery temperature would therefore equal the gas stagnation temperature, $T_{o,\infty}$. However, an adiabatic assumption is invalid, since the temperature gradient formed across the boundary layer promotes thermal conduction back towards the outboard flow (Hottel and Kalitinsky, 1945). This results in a local gas recovery temperature that is below that established solely due to viscous dissipation. The opposing effects of conduction and viscosity therefore limit the gas temperature around the thermocouple junction to $< T_{o,\infty}$ (Moffat, 1962).

In the absence of external heat transfer, the temperature recovery factor, λ, is used to characterise the relationship between the gas stagnation temperature and the thermocouple junction temperature (Simmons, 1957) [4]. The temperature recovery factor is defined by equation 2.5, which is a function of the adiabatic junction temperature, $T_{j\,ad}$, as well as the gas static, T, and stagnation, $T_{o,\infty}$, temperatures. Under adiabatic conditions, it should be noted that the thermo-

[4]Care must be taken to distinguish between λ and $R_{p,T}$. λ excludes external heat transfer effects, while $R_{p,T}$ includes these effects.

couple junction temperature is equal to the local gas recovery temperature.

$$\lambda = \frac{T_{j\,ad} - T_\infty}{T_{o,\infty} - T_\infty} \tag{2.5}$$

The magnitude of the temperature recovery factor, λ, is dependent on both the geometry of the thermocouple and the local flow conditions within the sensing chamber (Scadron *et al.*, 1952). The Prandtl number is of particular significance, since it relates the opposing effects of viscous dissipation and thermal conduction. The Reynolds number is also important, since it determines the boundary layer state (laminar or turbulent).

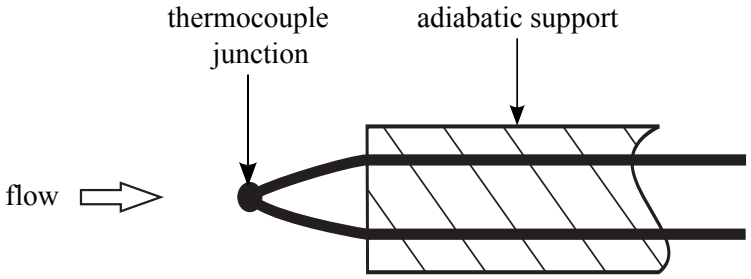

Figure 2.7: A schematic diagram of an unshielded thermocouple probe of the type investigated by Hottel and Kalitinsky (1945).

Hottel and Kalitinsky (1945) have studied the temperature recovery performance of a number of unshielded thermocouples, of the type illustrated in Figure 2.7. For thermocouples aligned with the free-stream flow direction, recovery factors of 0.86 ± 0.09 have been reported. For a Mach number of 0.8 at ambient temperature conditions, these values correspond to under-reads in the measured gas stagnation temperature of approximately $4.77\,K$. This result demonstrates the importance of installing the thermocouple inside a stagnation tube, where the free-stream flow is decelerated to less than Mach 0.25 (see section 2.1.2). Under these conditions, the under-read in the measured gas stagnation temperature is reduced to approximately $0.52\,K$.

2.2.3.1 Conductive heat transfer effects

In order to provide an accurate measurement of the gas stagnation temperature, it is clear that the thermocouple sensor must be surrounded by a stagnation tube (see section 2.2.3). However, this arrangement causes the junction temperature to become sensitive to thermal conduction along the thermocouple wire to the base of the stagnation tube (Moffat, 1962). The conductive heat flows established in a typical stagnation temperature probe are depicted in Figure 2.8

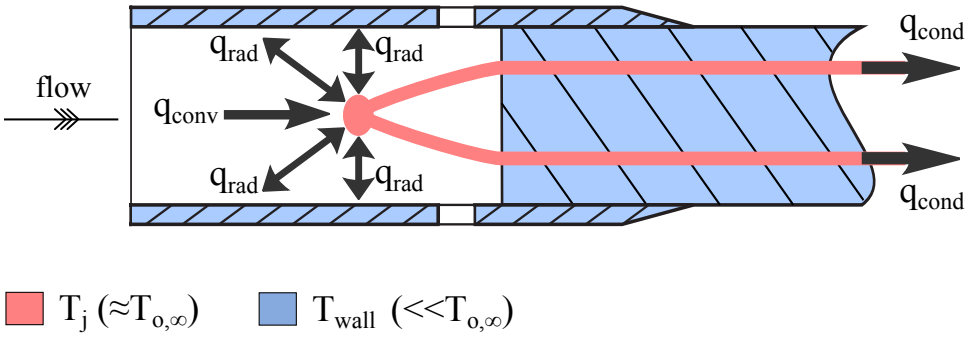

Figure 2.8: A schematic diagram of heat flows in a stagnation temperature probe (arrows indicate heat transfer paths).

The external surfaces of the thermocouple and the stagnation tube are all subjected to the gas recovery temperature (see section 2.2.3). Since the outside of the stagnation tube is exposed to the high free-stream velocity, the local gas recovery temperature is low. Accordingly, the temperature of the stagnation tube, T_{wall}, acquires a value appreciably below $T_{o,\infty}$. Conversely, since the thermocouple is exposed to the low sensing chamber velocity (typically $<$ Mach 0.25), the local gas recovery temperature is high. The thermocouple junction temperature, T_j, therefore attains a value significantly closer to $T_{o,\infty}$. This temperature difference $(T_j - T_{wall})$ drives conductive heat loss from the thermocouple to the stagnation tube, resulting in a consequent under-read in the measured gas stagnation temperature.

The conductive heat flux along the thermocouple wire is determined by equation 2.6, which is Fourier's law for steady unidirectional conduction (McAdams, 1954).

$$q_{cond} = -k\frac{(T_j - T_{wall})}{l} \tag{2.6}$$

From this equation, it is apparent that thermal conduction between the thermocouple and the stagnation tube can be reduced via three distinct techniques. Firstly, the temperature difference established between the thermocouple junction and the stagnation tube $(T_j - T_{wall})$ can be decreased. Secondly, the unsupported length of the thermocouple, l, can be increased. Thirdly, the thermal conductivity of the thermocouple wire, k, can be reduced. Further descriptions of these three techniques are provided in the following sub-sections.

Reduced thermocouple conductivity Practically, a reduction in thermal conductivity is difficult to achieve, since it is dictated by the thermocouple wire materials. For the 'K' and 'N' type devices commonly used in gas turbine engines, thermal conductivities are fixed at $20 - 30\,W/mK$. In order to reduce thermal conduction between the thermocouple and the stagnation tube, attention must therefore be focussed on alternative approaches.

Increased thermocouple length Moffat (1962) recommends using an unsupported thermocouple length that is > 10 thermocouple diameters. The benefits of adopting this approach have been demonstrated by Wilson *et al.* (2012), who considered the influence of thermal conduction on a cooled turbine traverse probe (see Figure 2.9). By increasing the unsupported thermocouple length, the underread in the measured stagnation temperature was reduced by over $100\,K$ in a

Mach 0.8 flow at $800\,K$.

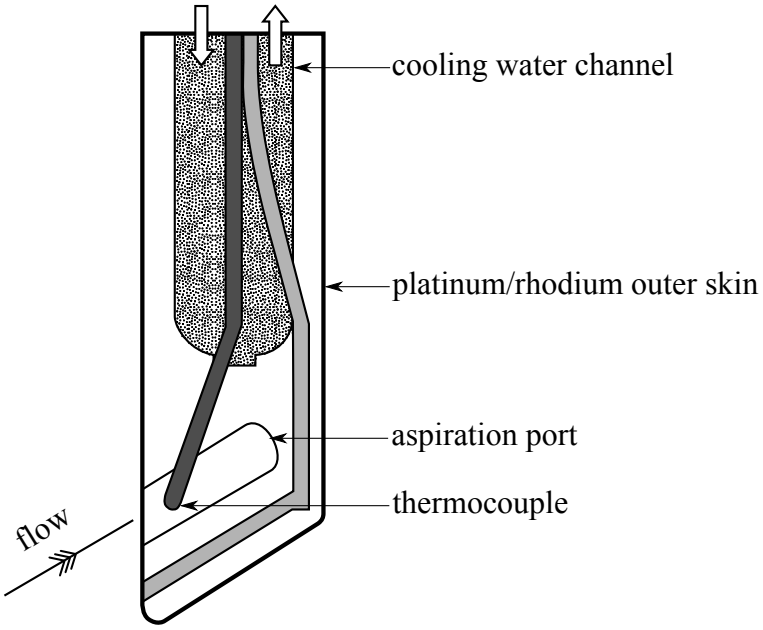

Figure 2.9: Cooled turbine traverse probe investigated by Wilson *et al.* (2012).

Decreased temperature difference Stanworth (1962) recommends decreasing the temperature difference between the thermocouple junction and the stagnation tube by the application of low thermal conductivity materials. The benefits of this approach have been demonstrated by Scadron *et al.* (1952), who investigated the performance of stagnation temperature probes constructed from Inconel ($k = 11.4W/mK$) and bakelite ($k = 0.2W/mK$). The bakelite probe displayed a higher temperature recovery factor, $R_{p,T}$, compared to the Inconel probe, indicating a smaller under-read in the measured gas stagnation temperature.

Mullikin (1941) described an alternative approach for decreasing the temperature difference between the thermocouple junction and the stagnation tube, which involved the application of an electrical heater (see Figure 2.10). In this arrangement, the heater was used to achieve thermal equilibrium between the thermocouple and the stagnation tube. However, this approach was judged to

be excessively cumbersome, with particular difficulties encountered in flows with rapid temperature variations (Moffat, 1962).

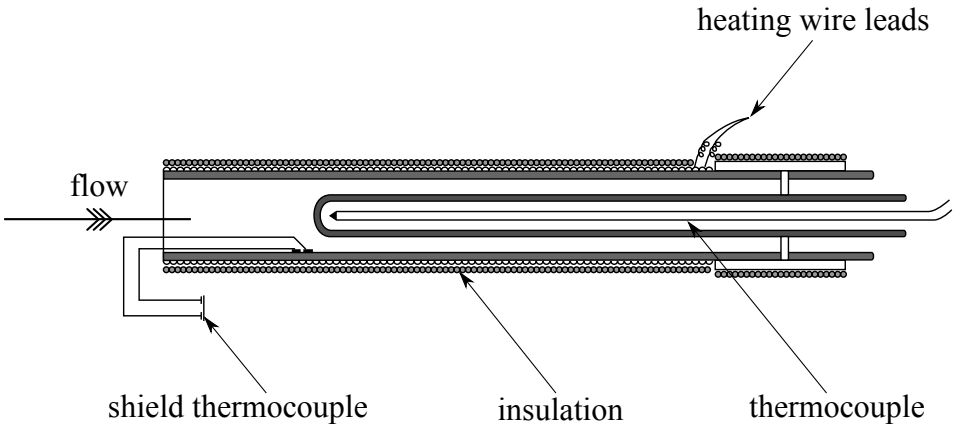

Figure 2.10: Electrically heated probe described by Mullikin (1941).

2.2.3.2 Radiative heat transfer effects

In addition to conductive heat transfer, the temperature of the thermocouple junction is sensitive to radiant heat transfer to the surroundings. In a typical probe arrangement, the thermocouple primarily radiates to the internal surface of the stagnation tube, as indicated in Figure 2.8. The low velocity within the sensing chamber allows the thermocouple junction to attain a temperature, T_j, close to $T_{o,\infty}$. Conversely, free-stream temperature recovery effects limit the temperature of the stagnation tube, T_{wall}, to a value below $T_{o,\infty}$ (see section 2.2.3.1). The temperature of the stagnation tube is also influenced by radiant heat transfer from the surrounding components of the engine. Since component metal temperatures are generally below $T_{o,\infty}$, this leads to further reductions in T_{wall} (Gorton, 1969). The temperature difference between the thermocouple and the stagnation tube ($T_j - T_{wall}$) therefore drives radiative heat loss from the thermocouple junction. As a consequence of this heat loss, a further under-read in the measured gas stagnation temperature is sustained.

Although the temperature difference between the thermocouple and the stagnation tube may be modest, it is the absolute temperature level that governs radiant heat transfer effects. For example, radiative heat losses are approximalety 250 times higher in gases at $1200\,K$ than in gases at $300\,K$ (Moffat, 1962). As a consequence, radiant heat transfer is the most important factor that influences the measurement performance of stagnation temperature probes under high temperature ($> 900\,K$) conditions (Zeisberger, 2007). Under low temperature conditions, radiant heat transfer is negligible and thermal conduction effects have the controlling influence on probe measurement performance.

The radiant heat flux between the thermocouple and the stagnation tube is governed by equation 2.7, which is known as the Stefan-Boltzman law (McAdams, 1954).

$$q_{rad} = \xi \sigma_B ({T_j}^4 - {T_{wall}}^4) \tag{2.7}$$

From this equation, it is clear that thermal radiation between the thermocouple and the stagnation tube can be reduced by two alternative approaches. Firstly, the temperature of the stagnation tube, T_{wall}, can be increased to match the thermocouple junction temperature, T_j. Secondly, reductions in the emissivity, ξ, of the thermocouple surface can be effected. Detailed descriptions of these two approaches are presented in the following sub-sections.

Increased stagnation tube temperature King (1943) considered the use of multiple radiation shields as a means of increasing the temperature of the internal surface of the stagnation tube. These shields take on the form of simple concentric cylinders, which are arranged around the thermocouple junction (see

Figure 2.11). The shields serve to isolate the internal surface of the stagnation tube from the low gas recovery temperatures ($\ll T_{o,\infty}$) established around the external body of the probe. By employing multiple concentric shields, the inner shield is capable of attaining a temperature sufficiently close to $T_{o,\infty}$ that radiative heat losses are significantly reduced. Since this arrangement is necessarily bulky, however, it is impractical for use in applications where space is restricted (Moffat, 1962).

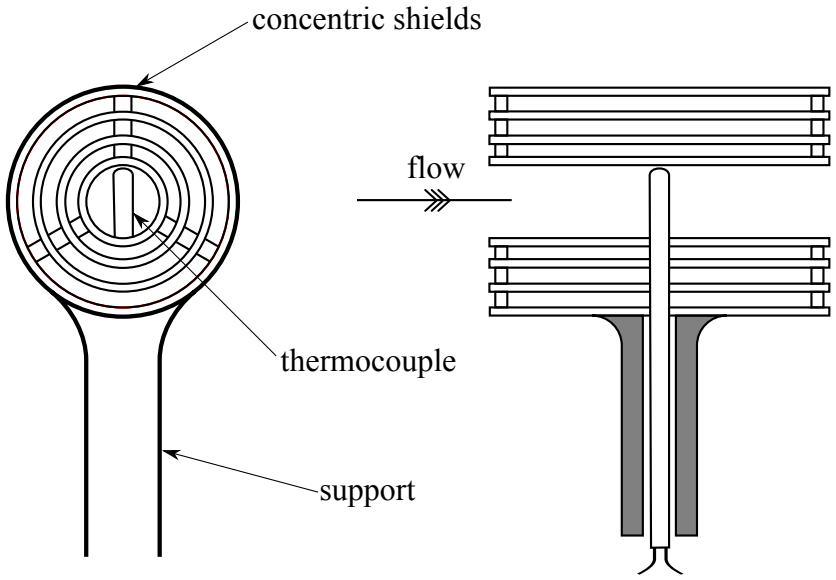

Figure 2.11: Stagnation temperature probe featuring multiple radiation shields (King, 1943).

Reduced thermocouple emissivity Dahl and Fiock (1949) demonstrated a technique for coating thermocouple surfaces in gold and silver ($\xi \approx 0.05$). In regard to reducing radiant heat transfer in a stagnation temperature probe, this technique was reported to be as effective as four concentric radiation shields. However, the coated thermocouple surfaces were found to quickly tarnish, particularly in environments containing combustion products. Unless frequent inspections are feasible, the surface emissivity therefore cannot be relied upon for decreasing radiant heat transfer between the thermocouple and the stagnation

tube (Moffat, 1962).

2.2.3.3 Convective heat transfer effects

The thermocouple junction acquires heat from the surrounding gas as a consequence of forced convection (Scadron *et al.*, 1950). By facilitating sufficient convective heat transfer to the thermocouple junction, the impact of conductive and radiative heat losses can therefore be diminished. The convective heat flux between the thermocouple and the oncoming gas is described by equation 2.8, which is known as Newton's law of cooling (McAdams, 1954).

$$q_{conv} = h(T_{gas} - T_j) \tag{2.8}$$

In this equation, the temperature difference between the thermocouple, T_j, and the surrounding gas, T_{gas}, is fixed by temperature recovery effects (see section 2.2.3). As a consequence, the only means of increasing convective heat transfer to the thermocouple junction is through raising the convective heat transfer coefficient, h.

The convective heat transfer coefficient is proportional to flow Reynolds number, which can be increased by raising the gas velocity within the sensing chamber (Flock, 1953). For a given free-stream Mach number, M_∞, an increase in sensing chamber velocity can be realised by enlarging the sectional area ratio between the inlet and outlet of the stagnation tube (Saravanamuttoo, 1990). At high area ratios, the impact of conductive and radiative heat transfer effects can therefore be considerably reduced. However, the benefits of this approach are eventually negated by temperature recovery effects, which cause the gas recovery tempera-

ture around the thermocouple junction to fall (see section 2.2.3). Flock (1953) reports that optimum probe measurement performance can be achieved when the sectional area ratio between the inlet and outlet of the stagnation tube equals 10.

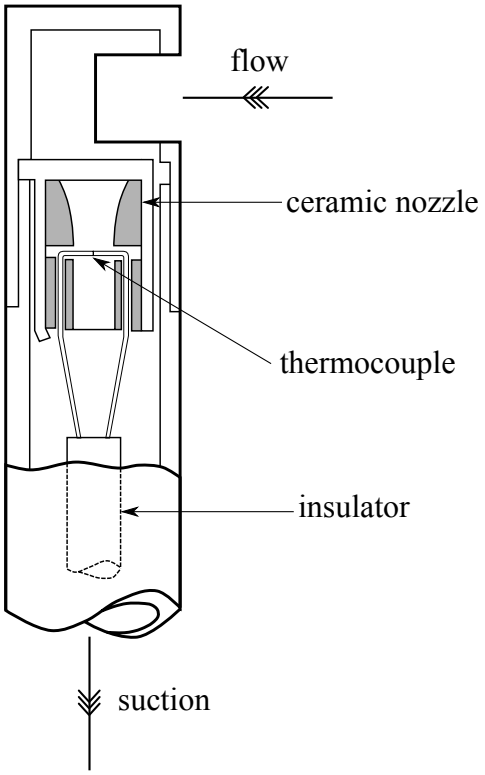

Figure 2.12: The aspirated thermocouple probe described by Stanworth (1962).

The advantages and disadvantages of a high convective heat transfer coefficient have been demonstrated by Stanworth (1962), who described a probe intended for application in the exhaust of a gas turbine engine. This probe consisted of a thermocouple sensor that was installed within an aspirated stagnation tube (see Figure 2.12). The thermocouple junction was positioned at the throat of a convergent nozzle, where pressures were maintained at sufficiently low values to generate sonic velocity flows. The provision of such velocities ensured that the impact of conductive and radiative heat losses from the thermocouple junction were negated by high convective heat transfer from the surrounding gas. However,

substantial post-test corrections had to be applied to probe measurements in order to account for temperature recovery effects.

2.3 Post-test measurement correction

To improve stagnation temperature accuracy, post-test corrections are commonly applied to measured temperatures in order to correct for probe temperature recovery performance (see section 2.2.2). The magnitude of the necessary corrections can be established using two distinct approaches. Firstly, a process of probe aerodynamic calibration can be performed. Secondly, the development of theoretical or numerical models can be undertaken. Sections 2.3.1 and 2.3.2 describe these two approaches in further detail.

2.3.1 Probe aerodynamic calibration

For a given probe design, the value of the probe temperature recovery factor, $R_{p,T}$, can be determined over a range of free-stream Mach numbers via an aerodynamic calibration process. This procedure can be performed using a free-jet test facility, of the type illustrated in Figure 2.13 (Saravanamuttoo, 1990). In this arrangement, the probe under test is positioned downstream of a convergent nozzle, through which a high-velocity jet is discharged. Measurements are acquired of the probe indicated temperature, T_{ind}, and the reference stagnation temperature, $T_{o,\infty}$. These measurements are subsequently utilised to calculate the probe temperature recovery factor, $R_{p,T}$, through equation 2.4. By repeating this process over a range of jet velocities, a calibration curve can be established detailing the variation in probe temperature recovery factor with free-stream Mach number.

Using this calibration curve, appropriate corrections can ultimately be applied to measured data acquired during engine test campaigns.

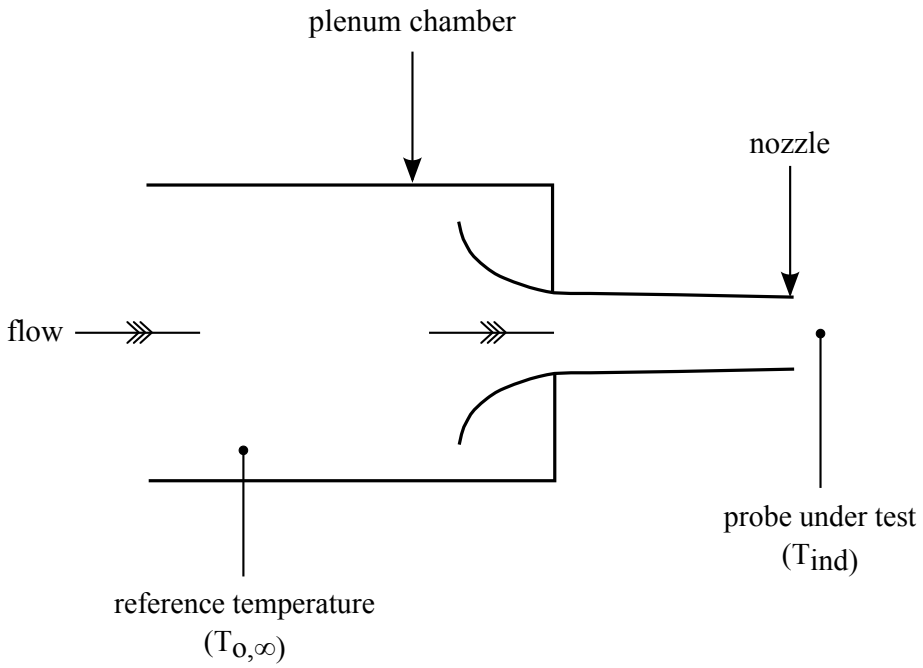

Figure 2.13: A schematic diagram of a typical free-jet test facility used for probe aerodynamic calibration (Saravanamuttoo, 1990).

Following the application of a post-test correction, the residual uncertainty in the corrected stagnation temperature is associated with the applied probe temperature recovery factor, $R_{p,T}$. This value is subject to experimental uncertainties in the aerodynamic calibration process, which are described in chapter 4. These experimental uncertainties propagate to the measurement correction and consequently limit the accuracy of the corrected stagnation temperature. The impact of uncertainties in the probe temperature recovery factor is necessarily greater for a large measurement correction. To achieve the highest level of stagnation temperature accuracy, the magnitude of any measurement correction must therefore remain small.

2.3.2 Probe models

Due to cost and time constraints, it is impractical to perform aerodynamic calibrations for all probe installation arrangements over a comprehensive range of engine operating conditions (Moffatt, 1952). As a consequence, several investigators have developed probe models to determine the magnitude of the necessary post-test correction at any given condition. For example, Moffatt (1952) produced a set of theoretical equations to correct the temperature indicated by a stagnation temperature probe featuring multiple radiation shields. A simple 1-D heat balance was additionally used by Zeisberger (2007) to predict heat flows in a conventional stagnation temperature probe mounted onto the leading edge of a rake. Finally, Wilson *et al.* (2012) used a commercial computational fluid dynamics code to develop a 3-D conjugate heat transfer model of a turbine traverse probe.

To validate the performance of these models, the investigators compared the modelling results to experiential aerodynamic calibration data. In each instance, a general trend-wise agreement was achieved between the model and the experiment. However, discrepancies in the absolute temperature levels were observed. These discrepancies were attributed to simplifications employed in the models (e.g. 1-D assumption), as well as uncertainties in the input boundary conditions (e.g. values of h and ξ). As a consequence, it is recommended that the use of modelling is restricted to probe design work (Moffatt, 1952). The modelling results are insufficiently accurate to be used as a basis for post-test measurement corrections.

2.3.3 Improved probe design

In view of the difficulties associated with both modelling and aerodynamic calibration, the best approach is to design a probe that can acquire sufficiently accurate measurements that a low level of post-test correction is required (Markowski and Moffatt, 1948). This probe must simultaneously control the impact of heat transfer and temperature recovery phenomena by employing a selection of the techniques described in section 2.2. If the probe can attain a sufficiently high temperature recovery factor ($R_{p,T} \approx 1$), no post-test correction will be required.

CHAPTER 3

Probe Aerodynamic Calibration Facility

3.1 Introduction

To facilitate investigations into the recovery performance of stagnation temperature probes, an aerodynamic calibration facility has been developed as part of the current work. This chapter provides a comprehensive description of this new facility. Initially, attention is focussed on the facility infrastructure, which comprises the compressed air supply system, the flow delivery pipework and the working section. The working section has been specifically developed for the purpose of this work, whereas the remaining elements of the facility infrastructure were already in place. Additionally, details are provided of the pressure and temperature instrumentation that is used to monitor the facility operating conditions. This instrumentation was also developed specifically as part of this work. Finally, the facility performance is reviewed in terms of the jet flow uniformity,

as well as the stagnation pressure and temperature measurement accuracy. This review is based on both new and historical test data.

3.2 Facility description

The existing Loughborough University high-pressure nozzle test rig (see for example Behrouzi and McGuirk, 2014) has been used as a basis on which to develop an aerodynamic calibration facility for stagnation temperature probes. The facility is serviced by a high-pressure compressed air system, capable of generating flows with stagnation pressures up to 8 *bar* at stagnation temperatures close to ambient. Compressed air is delivered to the facility working section via a convergent nozzle that produces a high-velocity jet. The working section is designed to allow the installation of instrumentation hardware in a variety of test configurations, including different mounting arrangements and flow incidence angles (see section 3.2.4). A schematic diagram of the test facility is provided in Figure 3.1, which features the compressed air supply system, the flow delivery pipework and the working section. These three aspects of the facility are described in further detail in sections 3.2.1 to 3.2.3. A photograph of the laboratory that houses the test facility is shown in Figure 3.2.

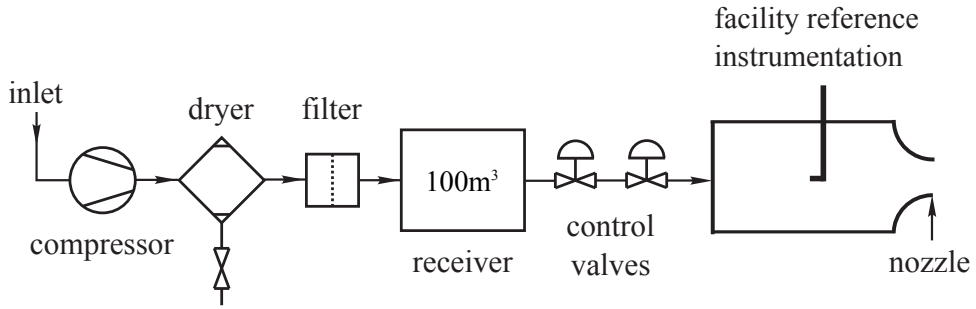

Figure 3.1: A schematic diagram of the probe aerodynamic calibration facility.

Figure 3.2: A photograph of the laboratory housing the probe aerodynamic calibration facility.

3.2.1 Air supply system

The test facility is supplied with air by two Kaeser screw compressors that can pressurise up to $1\,kg/s$ of ambient air to $14\,bar$. Air delivered from the compressors is initially fed into a $5\,m^3$ holding tank before being discharged through a desiccant (adsorption) dryer that performs gaseous water vapour removal to a dew point of $233\,K$ (-40° C). Downstream of the dryer, the compressed air is passed through a coalescing filtration system that removes liquid aerosols and solid particulate down to diameters of $0.01\,\mu m$. The dry, filtered air is then stored in a receiver tank with a $100\,m^3$ holding capacity. When the facility is running in continuous mode, the large volume of this tank acts as a buffer to damp any pressure fluctuations. It also provides a means of generating elevated mass flow rates ($\geq 1\,kg/s$) when the facility is operating in blow-down mode.

3.2.2 Flow delivery pipework

A 6" diameter pipeline transports compressed air from the receiver tank to the laboratory housing the test facility. This pipeline includes two in-series control valves that regulate the flow from the $14\,bar$ supply pressure down to the target working section delivery pressure ($\leq 8\,bar$). The first (coarse) stage of pressure control is provided by a Severn Glocon piston actuated valve that instigates the bulk of the flow pressure drop required. A Spirax Sarco globe valve then refines the flow pressure to within 1 % of the target value, providing the second (fine) stage of pressure control. Inside the test cell, the 6" pipeline delivers the regulated air to a convergent nozzle with a $60\,mm$ throat diameter. This contraction serves to accelerate the flow, forming a circular jet with velocities up to Mach 1.0.

3.2.3 Working section configuration

At the nozzle exit, the high-velocity air jet is discharged into the facility working section which houses the probe under test. For the purpose of aerodynamic calibration, the working section can be configured in two distinct ways. Firstly, as a free-jet that operates at atmospheric static pressure, and secondly as an enclosed-jet that operates at elevated static pressure. These two arrangements primarily allow probe calibrations to be obtained as a function of jet Mach number; however, the later configuration also allows trends with Reynolds number to be explored through variations in jet static pressure.

Figure 3.3 (a) shows a drawing of the working section in a free-jet configuration, in which the nozzle issues directly into the laboratory. This arrangement allows

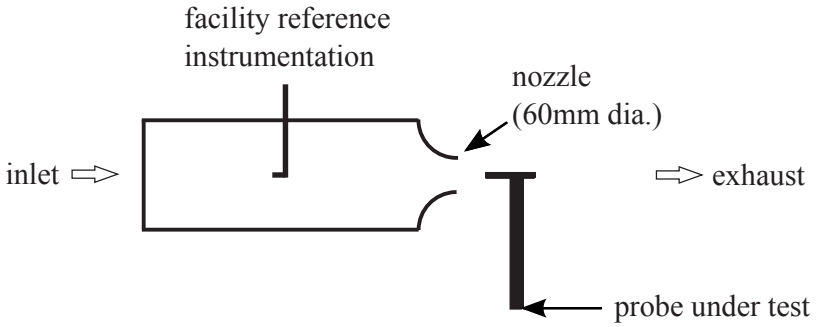

(a) free-jet configuration

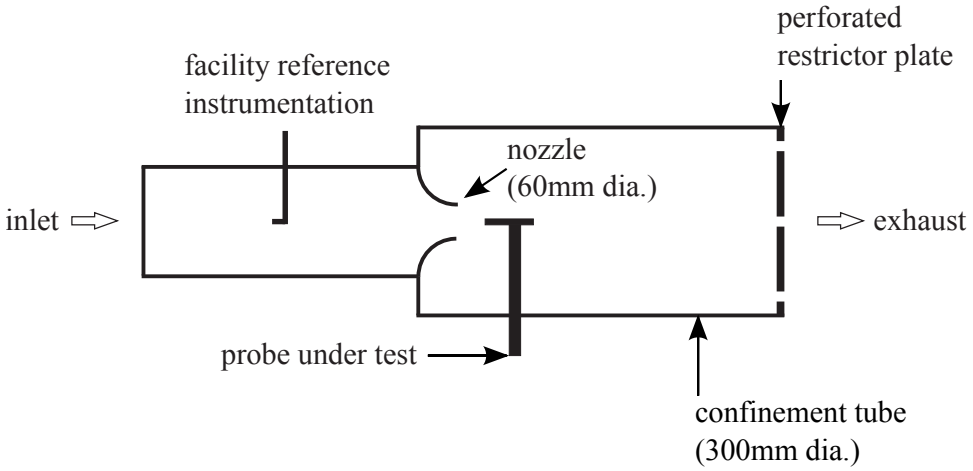

(b) enclosed-jet configuration

Figure 3.3: Schematic diagrams of the facility working section.

probe temperature recovery performance to be assessed under atmospheric conditions that are representative of a gas turbine inlet environment (see Table 2.1). Testing is typically performed over a range of jet velocities up to Mach 0.85, corresponding to Reynolds numbers (based on a $5\,mm$ probe diameter) of up to 100,000.

Figure 3.3 (b) shows the working section in an enclosed-jet configuration. In this arrangement, the nozzle issues into a large diameter ($300\,mm$) confinement tube that is capped with a perforated restrictor plate. The static pressure within the confinement tube can be increased up to values of $4\,bar$ by manually manipulating the open area of the restrictor plate. This allows probe temperature recovery

performance to be assessed at elevated Reynolds number conditions that are representative of the low and intermediate pressure compression system of a gas turbine engine (see Table 2.1). Once again, testing is typically performed over a range of jet Mach numbers up to 0.85, corresponding to Reynolds numbers (based on a $5\,mm$ probe diameter) of up to 200,000 at the highest static pressure conditions.

3.2.4 Test piece installation

In both working section configurations, the probe under test is positioned on the jet centreline with the leading edge located $60\,mm$ downstream of the nozzle throat. In the free-jet arrangement, the probe is mounted to a rotary traverse table that is capable of imparting changes in yaw angle. The rotary traverse is attached to a 3-D linear traverse, which is used to reposition the probe on the jet centre-line. This enables the angular sensitivity of the probe to be investigated. In the enclosed-jet arrangement, the probe is mounted to a simple sting that is held in the side-wall of the confinement tube. Testing in this configuration is therefore restricted to the case of 0^o yaw.

Probes may be tested in both sting-mounted and rake-mounted arrangements, as illustrated by the schematic diagrams in Figure 3.4 and the photographs in Figure 3.5. In the rake-mounted arrangement, the probe head is held within a cylindrical cavity in an aerodynamically profiled stainless-steel block. Thermally conductive paste is used to bond the probe to the cavity surface such that thermal contact is achieved. This type of installation is intended to simulate core-compressor and turbine instrumentation, both in terms of the aerodynamic situation around the probe head and the thermal boundary conditions to which it is subjected

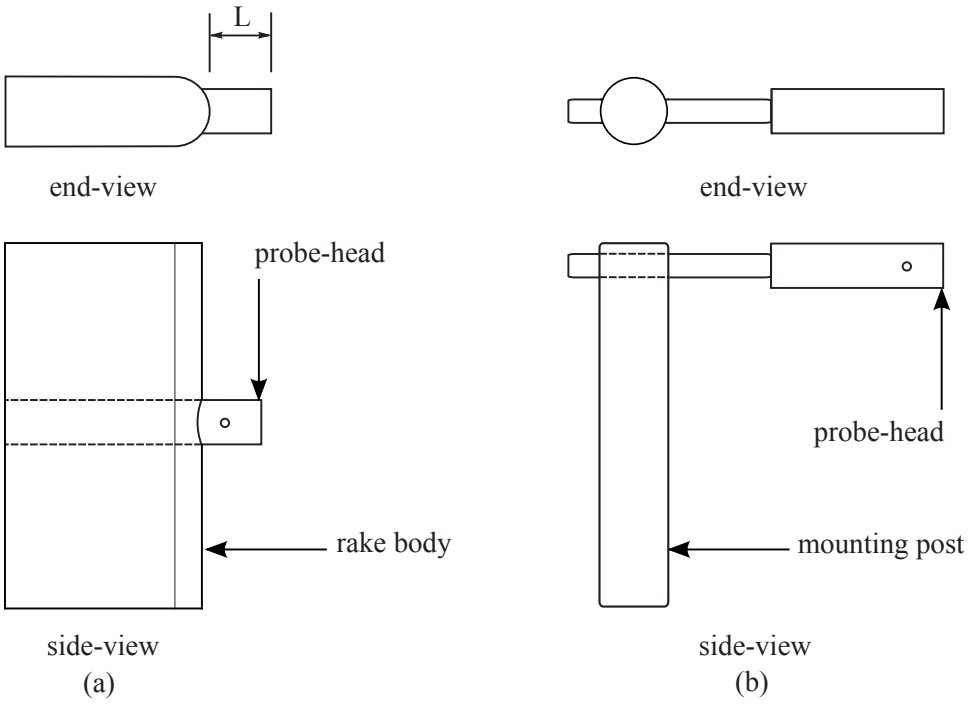

Figure 3.4: Schematic diagrams of rake-mounted (a) and sting-mounted (b) probe arrangements (also showing the definition of the probe protrusion length, L, for the rake-mounted case).

(see section 2.1.3). In the sting-mounted case, the probe head is attached to a long stainless-steel tube which is clamped to a simple mounting post. The sting arrangement allows probe performance to be assessed in isolation of aero-thermal installation effects, which is useful for the cross-comparison of alternative probe designs. This type of installation is also intended to simulate surface-bonded instrumentation, which is commonly found on the fan outlet guide vane and engine section stator (see section 2.1.3).

3.3 Facility instrumentation

During aerodynamic calibration, a number of different measurement systems capture the key variables that are needed to determine the probe temperature recov-

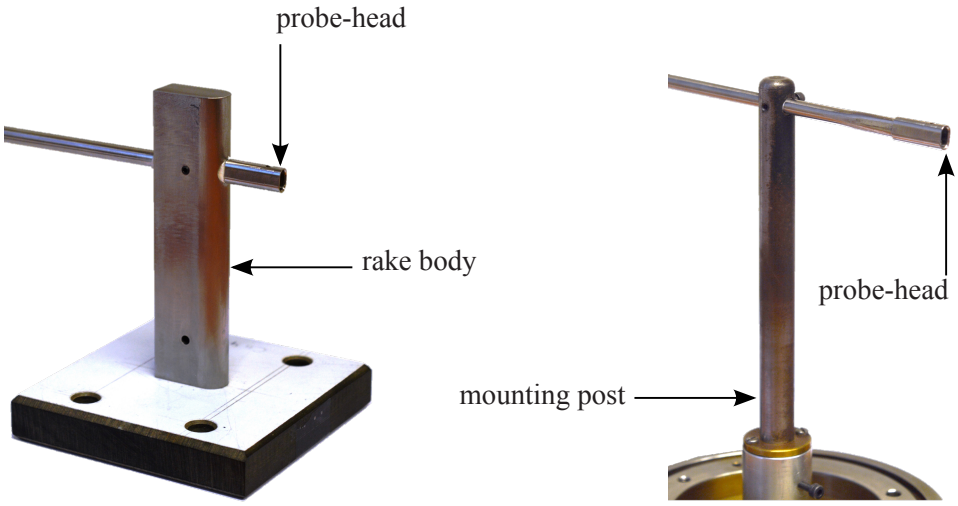

Figure 3.5: Photographs of the rake-mounted (a) and sting-mounted (b) probe arrangements.

ery factor over a range of flow conditions. These systems are most appropriately grouped into two categories: those providing temperature measurement data (section 3.3.1) and those providing pressure measurement data (section 3.3.2).

3.3.1 Temperature measurement systems

Two key temperature measurements are required for the assessment of probe temperature recovery performance. These are the temperature indicated by the probe under test, T_{ind}, and the reference free-stream stagnation temperature, $T_{0\infty}$. It is the difference between these two temperature measurements that is indicative of probe temperature recovery performance.

The reference free-stream stagnation temperature is measured at a location in the 6" pipeline upstream of the nozzle throat, as indicated in Figure 3.3. In this region, flow velocities are sufficiently low (less than Mach 0.16) that the impact of temperature recovery effects is reduced to a low level. The temperature measured

at this location can therefore be considered representative of the *true* stagnation temperature of the flow (see section 3.4.3 for further analysis). Measurements are made using a bespoke passively ventilated thin-film PRT probe that is pictured in Figure 3.6. This probe is connected in 4-wire mode to a Pico PT-104 resistance measuring instrument, which is linked to a desktop computer running LabVIEW data acquisition software.

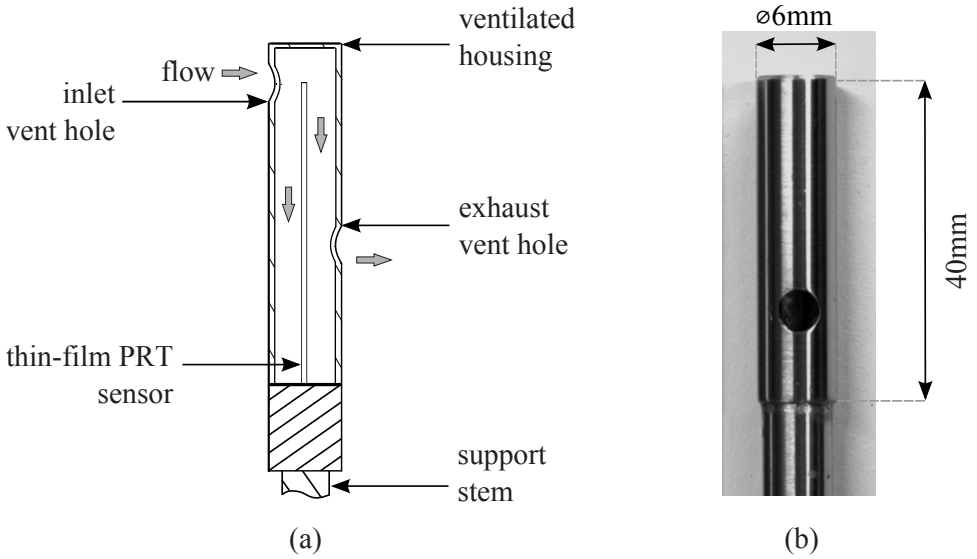

Figure 3.6: A cross-section diagram (a) and photograph (b) of the passively ventilated thin-film PRT probe used for reference stagnation temperature measurements.

The probe under test is positioned on the jet centreline at a distance 60 mm downstream of the nozzle throat (see section 3.2.4). At this location, probe temperature recovery performance can be investigated by monitoring changes in the probe temperature, T_{ind}, indicated at different jet Mach number conditions. The probe indicated temperature is recorded by one of two measuring instruments, specified according to sensor type. For minature PRT-based probes, measurements are made with the same Pico PT-104 unit employed with the reference stagnation temperature probe. For thermocouple-based probes, measurements are instead made using a National Instruments SCXI device with an external

cold junction ($273.15\,K$) reference. In either case, measurements from the probe under test are recorded simultaneously with measurements from the reference stagnation probe, using LabVIEW data acquisition software.

Ultimately, the acquired measurements of probe indicated temperature and free-stream stagnation temperature can be used in the computation of probe temperature recovery factor, $R_{p,T}$, through equation 2.4. However, from equation 2.4 it is clear that knowledge of the free-stream static temperature, T_∞, is also required to determine the value of $R_{p,T}$. This is established from the measured flow stagnation temperature via equation 3.1, which introduces the free-stream Mach number, M_∞.

$$T_\infty = \frac{T_{o,\infty}}{1 + \frac{\gamma-1}{2} M_\infty^2} \tag{3.1}$$

In order to calculate the probe temperature recovery factor, knowledge of the free-stream Mach number is therefore required. The derivation of this parameter is described in section 3.3.2.

3.3.2 Pressure measurement systems

The free-stream jet Mach number is established from measurements of the jet static pressure, P_∞, and stagnation pressure, $P_{o,\infty}$ using equation 3.2.

$$M_\infty = \left[\left[\left(\frac{P_{o,\infty}}{P_\infty} \right)^{\frac{\gamma-1}{\gamma}} - 1 \right] \frac{2}{\gamma - 1} \right]^{\frac{1}{2}} \tag{3.2}$$

The stagnation pressure is measured in the 6" pipeline upstream of the nozzle, at

a location coincident with the stagnation temperature measurement plane. The benefits of this location from a pressure recovery perspective are described in section 3.3.1. The stagnation pressure is measured using a conventional Pitot tube, with a typical pressure recovery factor, $R_{p,P}$, of approximately 0.99 (Folsom, 1955). The pressure is monitored uisng a Huba Controls 691 series absolute pressure transducer, coupled to the Pitot tube via a length of flexible tubing. The output from the transducer is connected to a National Instruments voltmeter, which is linked to a desktop computer running LabVIEW data acquisition software.

The location selected for the measurement of static pressure is dependent on the configuration of the working section. In an enclosed-jet arrangement, static pressure measurements are obtained using a tapping located in the working section side-wall. For a free-jet arrangement, measurements are instead based on the ambient pressure in the laboratory. In either situation, the pressure is monitored via a Huba Controls 691 series transducer that is connected to a National Instruments voltmeter. The measured static pressure is logged simultaneously with measurements of the jet stagnation pressure, using LabVIEW data acquisition software.

In some instances, the probe under test may incorporate a Pitot tube that facilitates the combined measurement of flow stagnation pressure and temperature (see Figure 2.2). The probe pressure recovery performance may be investigated by monitoring changes in the probe indicated pressure, P_{ind}, at different jet Mach number conditions. This information can be utilised to quantify the probe pressure recovery factor, $R_{p,P}$, through equation 3.3.

$$R_{p,P} = \frac{P_{ind} - P_{\infty}}{P_{o,\infty} - P_{\infty}} \tag{3.3}$$

The probe indicated pressure is measured relative to the jet stagnation pressure using a Sensor Technics BTE5000 differential pressure transducer. Based on this measurement, $P_{ind\,rel}$, the absolute probe indicated pressure may be determined from equation 3.4.

$$P_{ind} = P_{o,\infty} - P_{ind\,rel} \tag{3.4}$$

The output from the probe pressure transducer is monitored using a National Instruments voltmeter, which is configured to transmit data to LabVIEW acquisition software. The probe pressure measurements are logged simultaneously with measurements of the jet static and stagnation pressure.

3.3.3 Static calibration

Static calibration is the most effective means of reducing the systematic (bias) uncertainty in a measurement system. To minimise experimental uncertainties, all instrumentation must therefore be statically calibrated to a traceable standard prior to use in the test facility. The procedures utilised for the calibration of temperature and pressure instrumentation are described in section 3.3.3.1 and section 3.3.3.2 respectively.

3.3.3.1 Temperature instrumentation

Each item of temperature instrumentation is calibrated as a complete measurement system, incorporating both the probe and the associated data acquisition

unit. The static calibration is conducted using a suite of thermal calibration equipment that is traceable to UKAS standards. The primary components of this system are semi-standard reference PRT probe, an Isotech TTI-7 resistance measuring instrument and an Isotech Europa temperature controlled stirred water bath. A photograph of this equipment is shown in Figure 3.7.

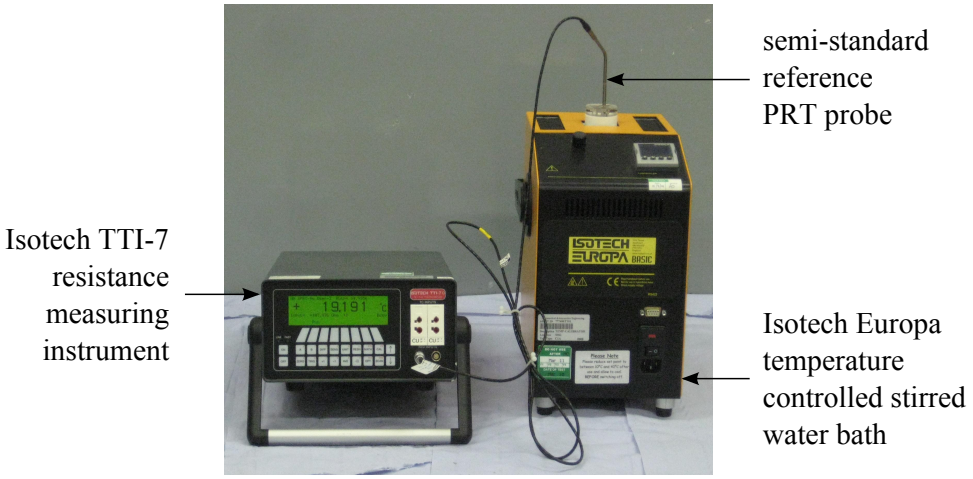

Figure 3.7: Temperature probe calibration equipment.

The calibration is performed by immersing the temperature probe within the stirred water bath, alongside the semi-standard PRT. The bath temperature is then cycled through a series of set points representative of anticipated experimental operating conditions (typically $278 - 298\,K$). Temperature responses from the two devices are recorded, and a linear relationship derived relating the probe measured temperature to the *true* temperature indicated by the semi-standard PRT. This relationship can subsequently be applied to all data acquired from the temperature measurement system, reducing a source of systematic uncertainty in the experimental results.

3.3.3.2 Pressure instrumentation

As with all temperature instrumentation, each item of pressure instrumentation is calibrated as a complete measurement system that includes both the transducer and data acquisition unit. The static calibration is performed by connecting the transducer to a G.E. Measurement & Control PACE 6000 device, as shown in Figure 3.8. The PACE 6000 provides an accurate and controllable pressure source that is traceable to a measurement standard. By adjusting the controller set point, the transducer can be exposed to a range of source pressures that are representative of experimental operating conditions. This enables a relationship to be derived relating the supply pressure to the transducer output voltage. The resulting relation can subsequently be used to interpret all data obtained from the pressure measurement system, reducing a further source of systematic experimental uncertainty.

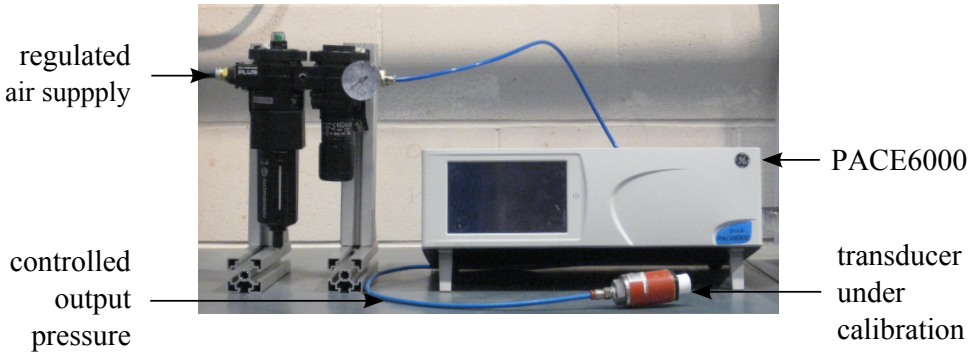

Figure 3.8: Pressure transducer calibration equipment.

3.4 Facility performance

Prior to the commencement of probe aerodynamic calibration studies, numerous investigations have been conducted into the performance of the test facility and

associated reference instrumentation. These have included analyses of the jet flow uniformity, as well as the stagnation pressure and temperature measurement accuracy.

3.4.1 Jet uniformity

An analysis of the flow field uniformity downstream of the 60 mm diameter convergent nozzle was conducted by Wilson *et al.* (2012) as part of a previous research project. In this study, a two component Dantec Dynamics laser Doppler anemometer was used to diagnose the axial jet velocity at a distance 0.5 diameters downstream of the nozzle throat. The measuring optics were mounted on a 3-D linear traverse system in order to establish a detailed map of the axial velocity field. The resulting traverse data are plotted in Figure 3.9 for a range of Mach numbers that are representative of those used in probe aerodynamic calibration (see section 3.2.3). These data indicate a maximum deviation in axial velocity of approximalety $\pm 0.5\,\%$ over the central 20 mm of the flow field. This region corresponds to the inviscid jet core, which is the main area of interest for probe aerodynamic calibration studies.

3.4.2 Jet stagnation pressure

The jet stagnation pressure is measured using a conventional Pitot tube, installed in the 6" pipeline upstream of the nozzle throat (see section 3.3.2). This measurement is used to determine the free-stream jet Mach number via Equation 3.2. This calculation relies on the assumption that no stagnation pressure loss occurs between the Pitot measurement plane and the working section. Behrouzi

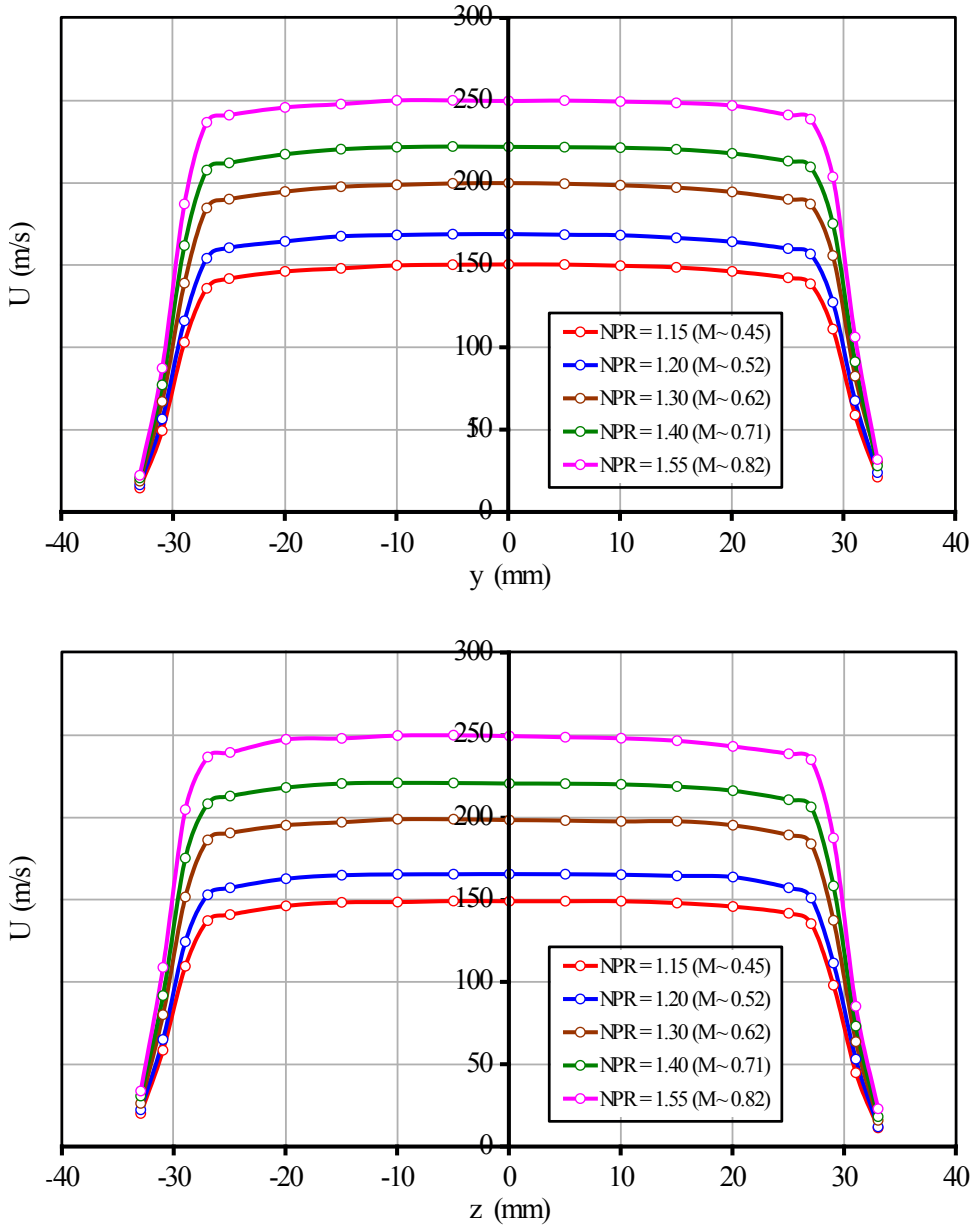

Figure 3.9: Measurements of axial velocity across the nozzle (Wilson *et al.*, 2012).

and McGuirk (2010) have explored the validity of this assumption by comparing the stagnation pressure measured in the 6" pipeline to the stagnation pressure measured by a second Pitot located 60 mm downstream of the nozzle throat. Selected results from this investigation are presented in Table 3.1 for a range of Mach numbers that are representative of those used in probe aerodynamic calibration (see section 3.2.3). The data reveal measured deviations in stagnation pressure of between 0 % and 0.39 %, with the largest variations occurring at the highest Mach numbers considered. These values are consistent with expected deviations incurred due to pressure recovery phenomena acting on the downstream Pitot tube ($R_{p,P} \approx 0.99$). Based on this rationale, the flow measurements indicate no evidence of pressure loss between the 6" pipeline and the working section. This result suggests that the downstream probe is operating within the inviscid jet core.

Jet Mach number	Upstream stagnation pressure (bar)	Downstream stagnation pressure (bar)	Pressure deviation (%)
0.45	1.15	1.150	0
0.50	1.2	1.199	0.083
0.62	1.3	1.298	0.154
0.70	1.4	1.398	0.143
0.81	1.55	1.544	0.39

Table 3.1: A comparison of stagnation pressures measured upstream and downstream of the nozzle throat (Behrouzi and McGuirk, 2010).

3.4.3 Jet stagnation temperature

Measurements of jet stagnation temperature are made using a passively ventilated thin-film PRT probe, located in the 6" pipeline upstream of the nozzle throat (see section 3.3.1). Mach numbers in this measurement region are gen-

erally low, however the residual flow velocity will introduce probe temperature recovery effects that may compromise indicated stagnation temperature accuracy. To determine the magnitude of this effect, assessments have been made of the residual velocity in the measurement region and the probe temperature recovery factor. Using these two parameters the deficit in probe indicated temperature relative to the *true* free-stream stagnation temperature can be predicted for given jet Mach number, via equations 2.4 and 3.1.

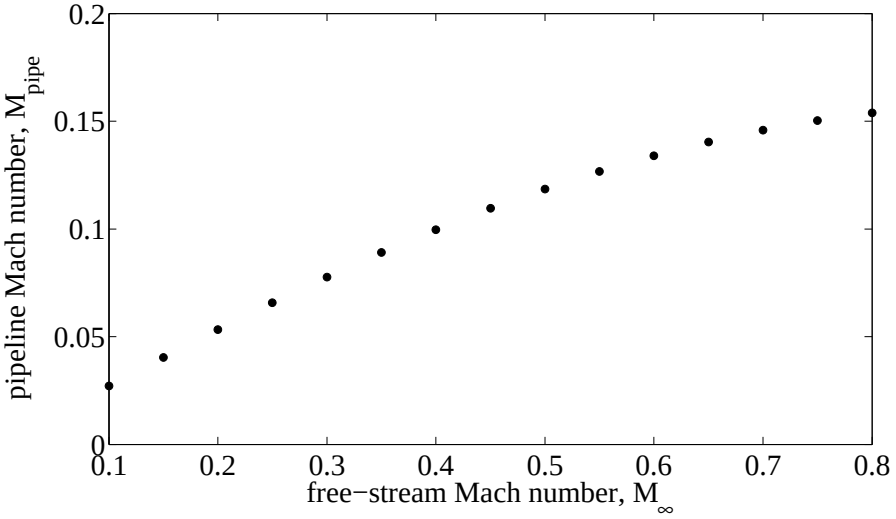

Figure 3.10: The estimated Mach number in the 6" pipeline upstream of the nozzle throat.

Figure 3.10 shows the Mach number in the measurement region plotted as a function of the Mach number of the jet. These values have been derived from the area-Mach number equation, which relates the Mach number at a given location to the local pipe area and the sonic nozzle area.

$$\left(\frac{A_{pipe}}{A*}\right)^2 = \frac{1}{{M_{pipe}}^2}\left[\frac{2}{\gamma+1}\left(1+\frac{\gamma-1}{2}{M_{pipe}}^2\right)\right]^{(\gamma+1)/(\gamma-1)} \tag{3.5}$$

Over a range of Mach numbers that are representative of those used in probe aerodynamic calibration (see section 3.2.3), the data indicate that the Mach

number in the 6" pipeline attains a maximum value of 0.16. This implies that any shortfall in indicated stagnation temperature arising due to recovery effects will be small. To quantify the magnitude of this shortfall, the temperature recovery factor of the passively ventilated thin-film PRT probe has been determined. This has been achieved through a process of aerodynamic calibration, in which probes of identical design have been used both as the stagnation reference and the device under test. The calibration has been restricted to a range of moderate free-stream jet Mach numbers in order to minimise recovery effects on the temperature reference.

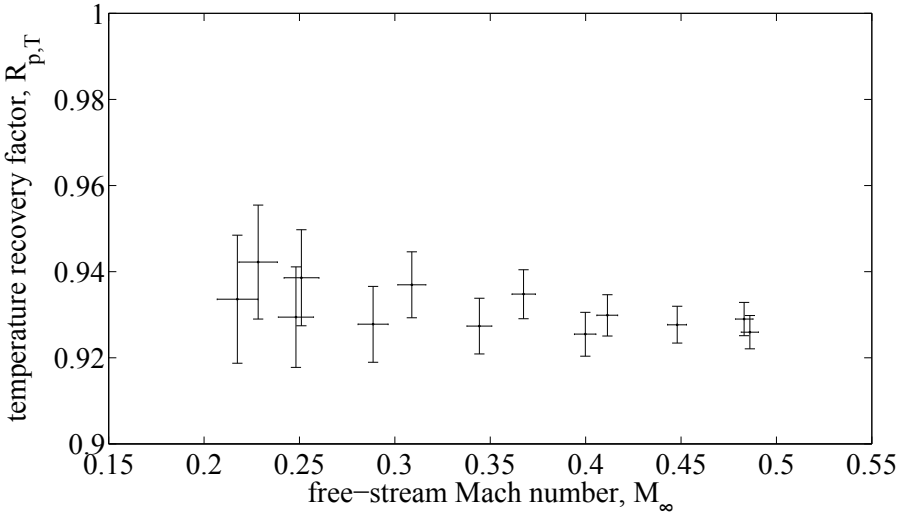

Figure 3.11: The temperature recovery factor of the passively ventilated thin-film PRT probe.

The aerodynamic calibration data for the passively ventilated thin-film PRT probe is plotted in Figure 3.11, which reveals an average probe temperature recovery factor of 0.93. This level of temperature recovery ($R_{p,T} \approx 1$) is characteristic of a minor deficit between the probe indicated temperature and *true* flow stagnation temperature.

Figure 3.12 shows the predicted shortfall in indicated stagnation temperature

based on the assessments of local flow velocity and probe temperature recovery factor. Data is plotted for a range jet Mach numbers with a nominal free-stream stagnation temperature of 300 K. At Mach 0.9, the data reveal a maximum deficit of 0.1 K between probe indicated temperature and *true* stagnation temperature. This deficit diminishes with Mach number, reducing to a value of approximately 0.02 K at Mach 0.3.

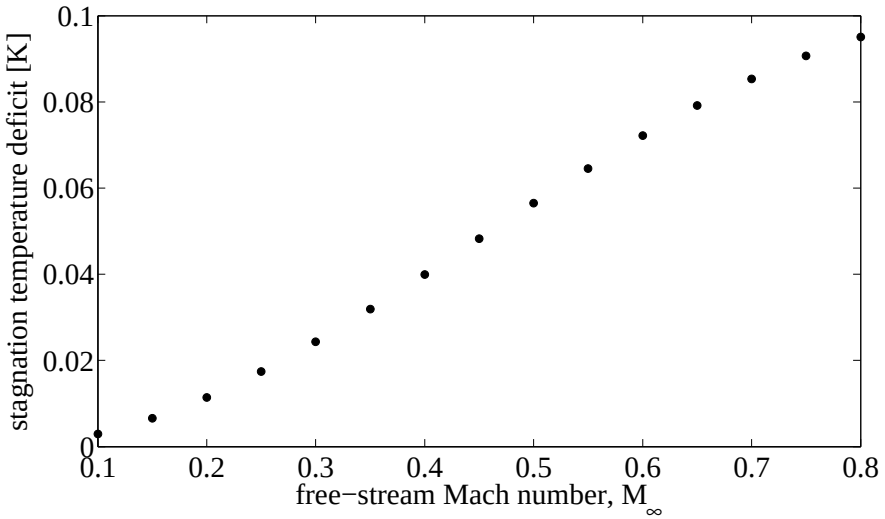

Figure 3.12: The predicted shortfall in the stagnation temperature indicated by the passively ventilated thin-film PRT probe.

CHAPTER 4

Measurement Uncertainty Analysis

4.1 Introduction

The previous chapter provides details the of aerodynamic calibration facility that has been developed at Loughborough University to study the recovery performance of stagnation temperature probes. In order to establish confidence in the measured probe temperature recovery factors, an analysis is required to determine the magnitude of experimentally induced uncertainties. This chapter describes the estimation of random and systematic uncertainties in each experimentally measured variable. It also describes the propagation of these uncertainties to the derived experimental results.

4.2 Methodology

The methodology adopted for the current analysis is based on the approach of Coleman and Steele (1995), which is similar to that described in the international standard for the expression of uncertainty in measurement (BIPM *et al.*, 1995). Firstly, attention is focused on estimating the uncertainties associated with variables measured during probe aerodynamic calibration. These consist of random and systematic uncertainties that are reported at the 95 % confidence limit. The Taylor series method is then used to propagate these measurement uncertainties through the appropriate data reduction equations to estimate the random and systematic uncertainty in each experimental result (temperature recovery factor, pressure recovery factor, Mach number, Reynolds number). Finally, the overall uncertainty in each result is established from an expanded uncertainty estimate, determined at the 95 % confidence limit.

4.3 Measured variables

An error will be associated with each variable, J, measured during probe aerodynamic calibration. The error in a general measurement, X_J, can be considered to consist of two components: a systematic error, β, and random error, ϵ (Coleman and Steele, 1995). The systematic error represents a fixed offset relative to the *true* value of the measured variable, whereas the random error leads to scatter in repeated measurements.

To demonstrate the statistical implications of these errors, it is useful to consider the probability density function that represents the *parent* population of a measured variable. A typical example is shown in Figure 4.1.

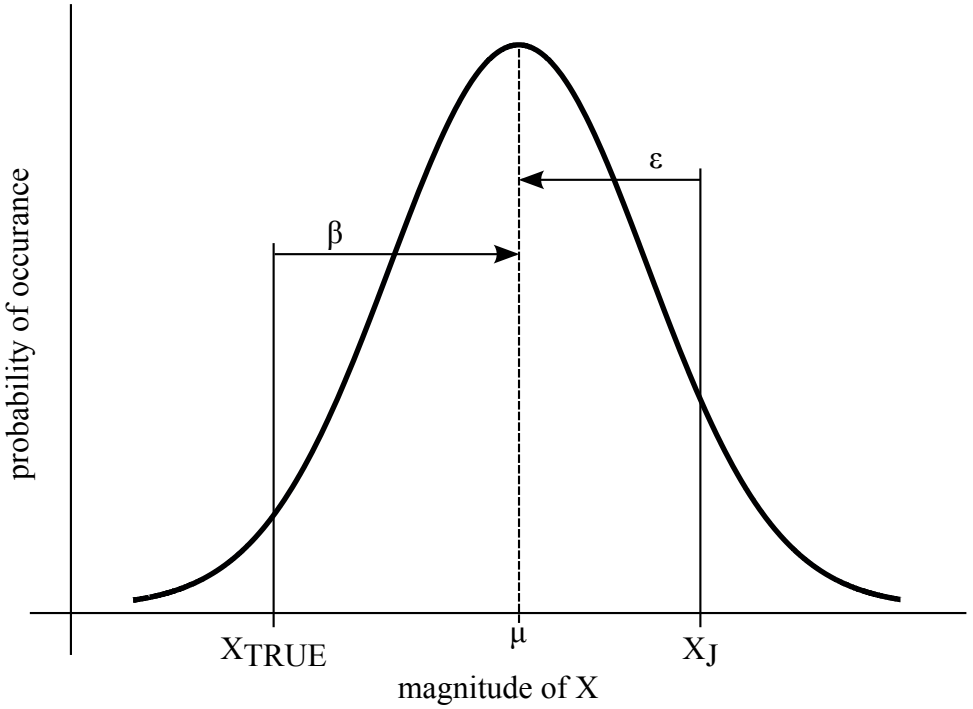

Figure 4.1: Definitions of systematic (β) and random (ϵ) errors for a single measurement drawn from a normally distributed population.

The *parent* population represented in Figure 4.1 is comprised of an infinite number of measurements acquired under constant conditions. The distribution of these measurements is described by the curve of the probability density function, which coincides with the normal, or Gaussian, distribution (Coleman and Steele, 1995). This distribution parametrises the *parent* population by a mean value, μ, and a standard deviation, σ.

The impact of systematic error on the *parent* population is revealed by an offset between the population mean and the *true* value of the measurand, X_{true}. The difference between these two values can be used to calculate the magnitude of the systematic error, via equation 4.1.

$$\beta = \mu - X_{true} \tag{4.1}$$

Since the parameters μ and X_{true} both represent fixed values, the contribution of systematic error remains constant across all measurements contained within the population.

The influence of random error on the *parent* population is indicated by the scatter of measurements about the population mean. For a single measurement, X_J, drawn from the population, the random error can be calculated from the difference between the mean and the measured value. This is expressed by equation 4.2.

$$\epsilon = X_J - \mu \tag{4.2}$$

Across the population, the magnitude of the random error will vary according to the specific location of X_J within the measurement distribution. A measurement drawn from the tail of the distribution will be associated with a necessarily larger error than a measurement drawn from the centre. This variation may be characterised by the standard deviation of the population, which quantifies the dispersion of measurements from the mean.

Under experimental conditions, the components of systematic and random error associated with a measurement, X_J, can prove difficult to quantify. In the case of the systematic component, the magnitude of the error cannot be computed since the value of X_{true} is unknown. In the case of the random component, the inherent variability of the error limits calculation to instances in which a *parent* measurement population is defined. To resolve these problems, estimates must be produced of the limits within which the systematic and random errors are expected to lie, to some level of confidence. These estimates are known as the systematic and random uncertainties in the measured variable. An uncertainty estimated at the 95 % level of confidence will define the limits of an interval con-

taining 95 % of the expected error values (Coleman and Steele, 1995). Convention dictates the use of a 95 % confidence level, however a 99 % confidence level is also occasionally employed.

The methods that may be used to determine these systematic and random uncertainties are described in sections 4.3.2 and 4.3.1, respectively.

4.3.1 Random uncertainty

The random uncertainty, P_J, in a measured variable is an estimate of the expected limits of random measurement error. These limits may be established from the standard deviation of a population of measurements, acquired under constant conditions. This is indicated by the histogram shown in Figure 4.2.

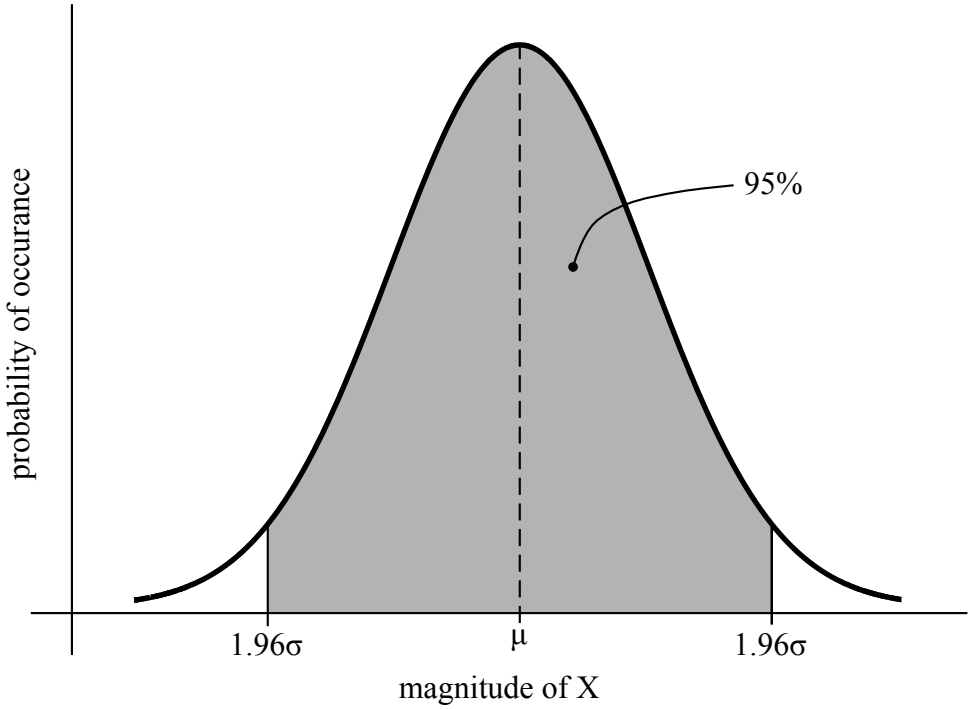

Figure 4.2: The 95 % confidence interval around the mean of a normally distributed population.

The probability density function plotted in Figure 4.2 represents the *parent* popu-

lation of a measured variable, which is described by the normal distribution. This distribution is defined such that 95 % of the population measurements fall within 1.96 standard deviations, σ, of the mean, μ (Coleman and Steele, 1995). For a single measurement drawn from the population, this implies 95 % confidence that an interval described by $\pm 1.96\sigma$ will include the *true* value of the random error. The limits of $\pm 1.96\sigma$ therefore represent a 95 % confidence estimate of the random error associated with a measurement. This statement is expressed by equation 4.3.

$$P_J = 1.96\sigma \quad \text{for 95 \% confidence} \tag{4.3}$$

From equation 4.3, it follows that the principal difficulty in evaluating the expected limits of random measurement error lies in determining the standard deviation of the *parent* population (Moffat, 1988). Since the *parent* population is of infinite size, however, sufficient experimental measurements to quantify this parameter can never be acquired. In reality, time and resource constraints limit experimental measurements to a finite sample, drawn from the *parent* population (Coleman and Steele, 1995). A histogram that represents such a sample is shown in Figure 4.3.

The measurement sample plotted in Figure 4.3 is characterised by a mean value, $\overline{X}$, and a standard deviation, S_X. These parameters provide approximations of the mean, μ, and standard deviation, σ, of the *parent* population. The sample standard deviation may therefore be used to estimate the expected limits of random measurement error specified in equation 4.3.

Since the measurement sample does not follow the normal distribution, however,

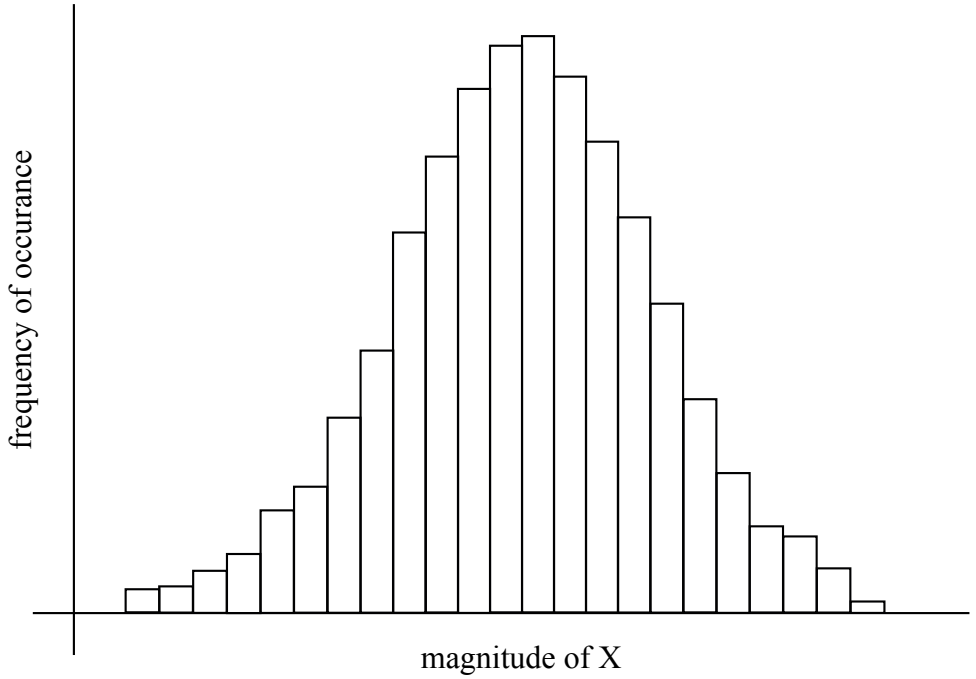

Figure 4.3: The distribution of a finite sample of measurements drawn from a normal population.

a factor of 1.96 can no longer be applied to the sample standard deviation to define the limits of the 95 % confidence interval. Rather, the sample standard deviation must be multiplied by an alternative factor taken from Student's t distribution. For 95 % confidence, the magnitude of this factor is determined by the size, N, of the measurement sample.

For $N \geq 10$, a large sample approximation can be employed, whereby the Student's t factor is rounded to an integer value of 2 (Coleman and Steele, 1995). In this situation, the limits of $\pm 2S_X$ represent a 95 % confidence estimate of the random error associated with a measurement. This statement is expressed by equation 4.4.

$$P_J \simeq 2S_X \quad \text{for 95 \% confidence } (N \geq 10) \tag{4.4}$$

4.3.1.1 Sample standard deviation

Based on the preceding analysis, the challenge of estimating the random uncertainty in a measured variable reduces to the task of determining the standard deviation, S_X, of a suitable measurement sample. This sample standard deviation may be computed from equation 4.5, where $\overline{X}$ is the sample mean.

$$S_X = \left[\frac{1}{N-1} \sum_{s=1}^{N} (X_s - \overline{X})^2 \right]^{1/2} \tag{4.5}$$

Since the sample must be drawn from a single *parent* population, the acquisition of individual measurements, X_s, must be performed under constant conditions. During an experiment, such conditions are difficult to achieve. However, in a static calibration scenario, a prescribed measurement environment may be established and maintained over time. The calculation of S_X is therefore commonly based on a measurement sample comprised of results from repeat static calibrations (Dieck, 2007). To facilitate use of the large sample approximation (see equation 4.4), the number of repeat static calibrations must be ≥ 10. These calibrations must be distributed over an appropriate time interval to capture the relevant random measurement variation (Moffat, 1988). They must also be performed under conditions that are representative of the experiment.

The following sections describe the application of this methodology to each of the variables measured during probe aerodynamic calibration. Typical conditions corresponding to each of these measurements are listed in Table 4.1. These conditions are representative of a free-stream Mach number of 0.6 and an ambient stagnation temperature of $288\,K$.

Experimental condition	Value
Free-stream stagnation temperature [K]	288
Free-stream stagnation pressure [bar]	1.276
Jet static pressure [bar]	1.000
Probe indicated temperature ($R_{p,T} = 0.9$) [K]	286
Probe indicated pressure deficit ($R_{p,P} = 0.99$) [bar]	0.003

Table 4.1: Typical experimental conditions corresponding to a free-stream Mach number of 0.6 and an ambient temperature of 288 K.

Temperature measurement systems Two key temperature measurements are acquired during probe aerodynamic calibration. These are the temperature indicated by the probe under test and the reference free-stream stagnation temperature (see section 3.3.1). The random variation in each measurement is dependent on both the temperature sensor and measuring instrument employed. For each distinct measurement system configuration, a separate standard deviation must therefore be determined. Based on the description of temperature instrumentation provided in section 3.3.1, three combinations of temperature sensor and measuring instrument can be identified. These are summarised in Table 4.2.

Measurement system	Temperature sensor	Measuring instrument
Reference stagnation probe	thin-film PRT	Pico PT-104
Probe under test	miniature PRT	Pico PT-104
Probe under test	N-type thermocouple	NI SCXI

Table 4.2: Temperature measurement system configurations.

For each temperature measurement system, the standard deviation is determined from a sample of measurements derived from the results of 10 repeat static calibrations. Each static calibration is performed in accordance with the procedure described in section 3.3.3.1, which leads to the formulation of 10 linear relationships that correlate the system measured temperature to the *true* temperature

indicated by the standard. For a nominal measured temperature, these calibration equations can be used to produce a sample of 10 corrected temperatures that indicate the random variation in the measurement system. An appropriate standard deviation may therefore be calculated from this sample via equation 4.5.

The outcome of this procedure is summarised in Table 4.4 for each of the temperature measurements identified in Table 4.2. In each case, the calculated standard deviation is based on the typical measurement condition stated in Table 4.1.

Pressure measurement systems During all probe aerodynamic calibrations, measurements of the jet static and stagnation pressure must be acquired in order to determine the free-stream Mach number condition (see section 3.3.2). For calibrations involving a combined pressure and temperature probe, measurements must additionally be acquired of the stagnation pressure deficit indicated by the probe under test. The combination of pressure transducer and measuring instrument employed in these three measurement systems is summarised in Table 4.3.

Measurement system	Pressure transducer	Measuring instrument
Jet stagnation pressure	Huba Controls 691	NI voltmeter
Jet static pressure	Huba Controls 691	NI voltmeter
Probe under test	Sensor Technics BTE5000	NI voltmeter

Table 4.3: Pressure measurement system configurations.

As with the temperature measurement systems, a separate standard deviation must be determined for each distinct pressure measurement system configuration. This standard deviation may be computed from equation 4.5, based on a sample of measurements derived from the results of 10 repeat static calibrations. These

calibrations follow the procedure described in section 3.3.3.2, which correlates the system supply pressure to the transducer output voltage. For a nominal measured voltage, a sample of 10 equivalent pressures may therefore be produced that reflects the random variation in the measurement system.

The standard deviation calculated from this measurement sample is summarised in Table 4.4 for each of the pressure measurements identified in Table 4.3. In each case, the result corresponds to the typical measurement condition stated in Table 4.1.

4.3.1.2 Calculation of random uncertainty

Based on the sample standard deviation quoted in Table 4.4, the random uncertainty associated with each of the variables measured during probe aerodynamic calibration may be calculated from equation 4.4. These uncertainties are summarised in Table 4.4 for the experimental measurement conditions outlined in Table 4.1 (free-stream Mach number of 0.6 and ambient stagnation temperature of $288\,K$). Since equation 4.4 defines a 95 % confidence interval, each value represents a 95 % confidence estimate of the expected random measurement error.

Measured variable	Standard deviation	Random uncertainty
Free-stream stagnation temperature [K]	5.939 x 10^{-3}	1.188 x 10^{-2}
Free-stream stagnation pressure [bar]	1.062 x 10^{-3}	2.124 x 10^{-3}
Jet static pressure [bar]	1.145 x 10^{-3}	2.290 x 10^{-3}
Probe indicated temperature (PRT) [K]	4.182 x 10^{-3}	8.364 x 10^{-3}
Probe indicated temperature (N-type) [K]	6.886 x 10^{-3}	1.377 x 10^{-2}
Probe indicated pressure deficit [bar]	5.199 x 10^{-5}	1.040 x 10^{-4}

Table 4.4: The sample standard deviation and random uncertainty in each measured variable, determined at the experimental conditions in Table 4.1 (95 % confidence).

4.3.2 Systematic uncertainty

The systematic uncertainty, B_J, in a measured variable can be attributed to the combined influence of a number of elemental systematic error sources. To establish the overall value of B_J, the systematic uncertainty corresponding to each elemental error source must be estimated and collated using equation 4.6 (Coleman and Steele, 1995). For W elemental sources of systematic error, this equation states that the overall systematic uncertainty is equal to the root-sum-square of the elemental systematic uncertainty terms.

$$B_J = \sqrt{\sum_{k=1}^{W} B_k^2} \tag{4.6}$$

The elemental systematic uncertainties, B_k, can originate from a variety of different error sources which include: measurement system static calibration, probe installation in the test environment and experimental approximation (Moffat, 1988). To estimate the magnitude of each elemental uncertainty, reference must be made to manufacturer specifications, analytical calculations or previous experimental experience (Coleman and Steele, 1995). Convention dictates that these estimates be reported at the 95 % confidence limit, such that the interval described by $\pm B_k$ contains 95 % of the expected error values (Moffat, 1988). Accordingly, the subsequent combination of the elemental systematic uncertainty terms represents a 95 % confidence estimate of the overall systematic measurement error. The limits of $\pm B_J$ therefore serve in a manner equivalent to a $\pm 2S_X$ estimate of the overall systematic error associated with a measurement (Moffat, 1988).

4.3.2.1 Static calibration

The discussion in section 3.3.3 described how static calibration could be employed to reduce the systematic error in a measurement. Any calibration correction, however, is subject to an uncertainty that is introduced by errors in measurements obtained from the calibration standard. During an experiment, this calibration uncertainty is fossilised in all corrected data acquired from an individual measurement system. The residual uncertainty arising from a static calibration procedure is therefore considered systematic.

Temperature measurement systems For the temperature measurement systems described in section 3.3.1, static calibrations are performed using a traceable semi-standard PRT probe connected to Isotech TTI-7 resistance measuring instrument (see section 3.3.3.1). The residual uncertainty associated with the temperature calibration procedure contains a contribution from both of these devices. The magnitude of each contribution can be established from the 95 % confidence uncertainty estimate quoted on the respective equipment calibration certificate. These values are summarised in Table 4.5 for an operational temperature range corresponding to between 273.15 K and 348.15 K.

Source	Systematic uncertainty
Semi-standard PRT probe [K]	2.0 x 10^{-2}
TTI-7 resistance instrument [K]	3.4 x 10^{-3}

Table 4.5: The systematic uncertainties associated with the temperature measurement standard (95 % confidence).

Pressure measurement systems The pressure measurement systems described in section 3.3.2 are statically calibrated relative to a traceable G.E. Mea-

surement & Control PACE 6000 precision pressure source (see section 3.3.3.2). The residual uncertainty associated with the pressure calibration procedure can be attributed to this device. Equation 4.7 shows the estimated source pressure uncertainty (at the 95 % confidence limit) quoted by the manufacturer as part of the equipment specification. Note that a 3.5 *bar* (full-scale) pressure control module is used for the calibration of jet reference instrumentation, whereas the calibration of probe specimens is performed with a 200 *mbar* (full-scale) module.

$$U_{95} = 0.005\% \text{ reading} + 0.005\% \text{ full-scale} \tag{4.7}$$

4.3.2.2 Probe installation

The installation of a probe within the test environment can lead to additional measurement errors, brought about by disturbances and interactions that occur between the probe and its surroundings (Moffat, 1988). Such phenomena are typically excluded from static calibration, as the environment in which the measurement system is calibrated generally differs from the experimental case. Separate consideration must therefore be given to the influence of probe installation on the systematic uncertainty associated with a measurement.

Probe under test Aerodynamic calibration seeks to assess the influence of the installation environment on the temperature measurement performance of a probe under test. This environment includes the aerodynamic situation around the probe head, as well as the thermal boundary conditions to which it is subjected. In this situation, an estimate of the systematic uncertainty attributed to probe installation effects is not required.

For an aerodynamic calibration to provide a true indication of probe temperature and pressure recovery performance, the probe installation environment must be well quantified. This relies on the provision of an accurate jet stagnation temperature reference, as well as the accurate measurement of jet static and stagnation pressures (for derivation of Mach number). The stagnation quantities are measured by probes mounted in the 6" pipeline upstream of the nozzle, whilst the static values are measured from a tapping located in the working section. Consideration is required to estimate the impact of these installation environments on the systematic uncertainty in each measured variable.

Stagnation temperature probe The reference stagnation temperature is measured using a passively ventilated thin-film PRT probe, located in the 6" pipeline upstream of the nozzle throat. The accuracy of this measurement is dependent on the impact of temperature recovery phenomena on the installed measuring device (see section 3.4.3). These phenomena arise from the local flow velocity in the measurement region, and result in a shortfall in probe indicated temperature relative to the *true* free-stream stagnation temperature. The magnitude of this deficit is related to the probe temperature recovery factor, $R_{p,T}$, which has been determined by aerodynamic calibration as around 0.93 (see Figure 3.11). Based on this recovery factor and the local flow velocity (plotted in Figure 3.10), estimates of the probe temperature measurement shortfall can be determined. These data are plotted in Figure 3.12 for an ambient stagnation temperature of $288\,K$ at different jet Mach number conditions. Since the estimated temperature deficit is fixed for a particular jet Mach number, this can be considered a source of systematic uncertainty in the reference stagnation temperature measurement. The magnitude of this uncertainty can be inferred directly from the data contained in Figure 3.12, which has been complied in Table 4.6 for

reference. These values are assumed to correspond to 95 % confidence estimates.

Jet Mach number	Temperature deficit [K]
0.3	2.431 x 10^{-2}
0.4	3.997 x 10^{-2}
0.5	5.652 x 10^{-2}
0.6	7.215 x 10^{-2}
0.7	8.534 x 10^{-2}
0.8	9.504 x 10^{-2}

Table 4.6: The estimated shortfall in measured stagnation temperature due to probe temperature recovery effects (ambient stagnation temperature of 288 K).

The systematic uncertainty in the reference stagnation temperature measurement will also be influenced by any change in flow temperature between the probe location and the working section. Such a deviation may occur due to heat transfer between the laboratory and the compressed air stream, as flow moves through the conveying pipework towards the nozzle throat. Since aerodynamic calibrations are carried out under ambient temperature conditions, however, the laboratory will sit at a similar temperature to the compressed air. Only a small temperature difference ($\leq 1\,K$) will therefore exist to drive the transfer of heat. Coupled with a short transition time between the probe measurement location and the working section ($\leq 0.1\,s$), this implies that laboratory heat transfer will have negligible impact on the temperature of the air stream. Accordingly, no additional source of uncertainty need be included in the systematic uncertainty estimate for the reference stagnation temperature measurement.

Stagnation pressure probe Measurements of stagnation pressure are acquired with a Pitot tube, installed in the 6" pipeline alongside the reference stagnation temperature probe. In this measurement region the flow velocity is

sufficiently high to induce probe pressure recovery phenomena, which limit the probe indicated pressure to below the *true* free-stream stagnation pressure. The magnitude of this pressure deficit is related to the pressure recovery factor, $R_{p,P}$, of a conventional Pitot tube, which previous investigators have reported to be in excess of 0.99 (see for example Folsom, 1955). Based on the local flow velocity (plotted in Figure 3.10), this characteristic recovery factor can be used to estimate the pressure measurement shortfall associated with the Pitot device. The resulting values determined at a variety of different jet Mach numbers are reported in Table 4.7. Since the estimated pressure deficit is constant for a particular jet Mach number condition, these data represent an additional contribution to the systematic uncertainty associated with the stagnation pressure measurement. A 95 % confidence limit is assumed.

Jet Mach number	Pressure deficit [bar]
0.3	4.485 x 10^{-5}
0.4	7.728 x 10^{-5}
0.5	1.160 x 10^{-4}
0.6	1.591 x 10^{-4}
0.7	2.044 x 10^{-4}
0.8	2.500 x 10^{-4}

Table 4.7: The estimated shortfall in measured stagnation pressure due to probe pressure recovery phenomena.

The systematic uncertainty associated with the measured stagnation pressure will also be impacted by pressure losses between the probe measurement location and the working section. Such losses have previously been considered by Behrouzi and McGuirk (2010), who compared the stagnation pressure measured in the 6" pipeline to the stagnation pressure measured 60 mm downstream of the nozzle throat (see section 3.4.2). The findings of this investigation revealed pressure

deviations that were consistent with the expected pressure recovery performance ($R_{p,P} \approx 0.99$) of the Pitot tubes employed in the measurement process. This result implies negligible pressure loss between the probe measurement location and the working section, which is symptomatic of the inviscid jet core. No additional source of uncertainty need therefore be included in the systematic uncertainty estimate for the stagnation pressure measurement.

Static pressure tapping The jet static pressure is measured from a pressure tapping located in the working section downstream of the nozzle. The accuracy of this measurement is dependent on the influence of the tapping on the local static pressure field. Common problems include local increases in static pressure caused by the deflection of flow streamlines towards the hole, and local decreases in static pressure attributed to flow separation at the hole leading edge (Chue, 1975). In practice, such pressure variations can be reduced by ensuring that the tapping is installed perpendicular to the flow, and manufactured to be both square-edged and burr-free. The tapping diameter should also be kept small compared to the overall working section dimensions (Shaw, 1960). Since the present tapping design has followed these guidelines, local pressure variations will remain small and the indicated pressure will be representative of the *true* free-stream static value. Accordingly, no corresponding source of systematic uncertainty need be included in the uncertainty estimate for the static pressure measurement.

4.3.2.3 Experimental approximation

An experimental approximation is introduced when a measurement at a discrete point location is used to infer the field-average value of a variable. Such an approach can lead to errors, brought about by the non-uniform distribution of

the variable across the field. To account for this phenomenon, the difference between the point and field-average value must be estimated and included as a contributor to the systematic uncertainty associated with the measurement (Moffat, 1988).

Probe-based measurements Experimental approximations are inherent to probe-based measurement techniques, such as those employed to monitor stagnation pressure and temperature during aerodynamic calibration (see section 3.3). The error associated with these approximations is dependent on the significance of the spatial gradients that exist across the measurement field. For fields containing sizeable gradients, the magnitude of the error is necessarily large. In this instance, however, traverse data reported by Wilson *et al.* (2012) have indicated the existence of uniform stagnation pressure and temperature distributions across the central $20\,mm$ portion of the flow field (see section 3.4). This region corresponds to the inviscid jet core, which is the main area of interest for probe aerodynamic calibration studies. Provided the stagnation probes are located within this area, the indicated pressure and temperature will therefore be representative of the relevant field-average properties. Consequently, experimental approximation may be excluded as a source of systematic uncertainty for the probe-based measurements.

4.3.2.4 Combination of uncertainties

For each variable measured during probe aerodynamic calibration, the overall systematic uncertainty can be calculated from equation 4.6 based on the elemental contributions of measurement system static calibration, probe installation environment and experimental approximation. These uncertainties are summarised

in Table 4.8 for the experiential conditions outlined in Table 4.1 (free-stream Mach number of 0.6 and ambient stagnation temperature of 288 K). Since the elemental systematic uncertainties are defined at the 95 % confidence limit, their combination represents a 95 % confidence estimate of the overall systematic measurement error.

	Uncertainty		
Measured variable	Calibration	Installation	Combined
Free-stream stagnation temperature [K]	2.0 x 10^{-2}, 3.4 x 10^{-3}	7.215 x 10^{-2}	7.480 x 10^{-2}
Free-stream stagnation pressure [bar]	2.388 x 10^{-4}	1.591 x 10^{-4}	2.870 x 10^{-4}
Jet static pressure [bar]	2.250 x 10^{-4}	-	2.250 x 10^{-4}
Probe indicated temperature (PRT) [K]	2.0 x 10^{-2}, 3.4 x 10^{-3}	-	2.029 x 10^{-2}
Probe indicated temperature (N-type) [K]	2.0 x 10^{-2}, 3.4 x 10^{-3}	-	2.029 x 10^{-2}
Probe indicated pressure deficit [bar]	1.015 x 10^{-5}	-	1.015 x 10^{-5}

Table 4.8: The systematic uncertainty in each measured variable, determined at the experimental conditions in Table 4.1 (95 % confidence).

4.4 Derived parameters

In most experiments, the result of interest cannot be measured directly. Rather, it must be derived from some combination of experimentally measured variables using an appropriate data reduction equation (Coleman and Steele, 1995). This is demonstrated by equation 4.8, where r is an experimental result determined from J measured variables, X_i.

$$r = r(X_1, X_2, X_2, ..., X_J) \tag{4.8}$$

Each measured variable included in equation 4.8 is associated with a systematic and random uncertainty. These measurement uncertainties propagate through

the data reduction equation to generate the systematic and random uncertainty in the derived result. The magnitude of the resultant uncertainties may be determined using the Taylor series method of uncertainty propagation (Dieck, 2007). This method impresses the effect of individual measurement uncertainties on to the derived experimental result. The same procedure is followed for both systematic and random uncertainties, however the two components are dealt with separately.

4.4.1 The general Taylor series method

For an experiential result calculated from a combination of measured variables, the effect of an uncertainty in a single variable, X_i, may be established using equation 4.9 (Moffat, 1988). In this equation, the partial derivative of r with respect to X_i characterises the sensitivity of the derived result to the measured variable. This parameter is used to convert the uncertainty in the measured variable, δX_i, to the corresponding uncertainty in the result, δr_{X_i}.

$$\delta r_{X_i} = \frac{\partial r}{\partial X_i} \delta X_i \tag{4.9}$$

A separate value of δr_{X_i} must be computed for each measured variable, X_i, included in the calculation of the experimental result. Each term represents the contribution of the uncertainty in the measured variable to the overall uncertainty in the result.

Based on the contributions of the individual measured variables, the overall uncertainty in the derived experiential result, δr, may be determined using equation 4.10 (Moffat, 1988). In this equation, a root-sum-square method is employed to

combine the values of δr_{X_i} associated with each measured variable.

$$\delta r = \left(\sum_{i=1}^{J} {\delta r_{X_i}}^2 \right)^{1/2} \tag{4.10}$$

This method of uncertainty combination requires each constituent uncertainty term to be expressed at the same percentage confidence. Accordingly, the overall uncertainty in the experimental result inherits this common confidence limit.

4.4.2 Random and systematic uncertainty

For probe aerodynamic calibration, four main parameters are commonly derived from experimentally measured variables (see section 3.3). These parameters include the probe temperature and pressure recovery factor, as well as the free-stream Mach and Reynolds number. To propagate random and systematic measurement uncertainties to these derived experimental results, the Taylor series method must be employed. This is achieved via the application of equations 4.11 and 4.12, which have been developed from the general uncertainty propagation equations in section 4.4.1 (Coleman and Steele, 1995).

$${P_r}^2 = \sum_{i=1}^{J} \left(\frac{\partial r}{\partial X_i} \right)^2 P_i^2 = \left(\frac{\partial r}{\partial X_1} \right)^2 {P_1}^2 + \left(\frac{\partial r}{\partial X_2} \right)^2 {P_2}^2 + \cdots + \left(\frac{\partial r}{\partial X_J} \right)^2 {P_J}^2 \tag{4.11}$$

$${B_r}^2 = \sum_{i=1}^{J} \left(\frac{\partial r}{\partial X_i} \right)^2 B_i^2 = \left(\frac{\partial r}{\partial X_1} \right)^2 {B_1}^2 + \left(\frac{\partial r}{\partial X_2} \right)^2 {B_2}^2 + \cdots + \left(\frac{\partial r}{\partial X_J} \right)^2 {B_J}^2 \tag{4.12}$$

Appendix A documents the use of equations 4.11 and 4.12 to propagate random (P_i) and systematic (B_i) measurement uncertainties to each of the experimental results derived for probe aerodynamic calibration. The components of random (P_r) and systematic (B_r) uncertainty determined from the propagation procedures are summarised in the first two columns of Table 4.9. These values are based on the random and systematic uncertainties associated with each measured variable, which are defined in Tables 4.4 and 4.8. Since the individual measurement uncertainties are specified at the 95 % confidence limit, each propagated uncertainty constitutes a 95 % confidence estimate of the error in the experimental result.

4.4.3 Expanded uncertainty

For probe aerodynamic calibration, the components of random and systematic uncertainty defined in Table 4.9 may be used to produce estimates of the expanded uncertainty, U_r, in each derived experimental result. This is achieved via the application of equation 4.13, which employs a root-sum-square method to combine the contributions of random and systematic uncertainty.

$$U_r = \sqrt{B_r^2 + P_r^2} \tag{4.13}$$

The expanded uncertainties determined from equation 4.13 are summarised in third column of Table 4.9. Since the components of random and systematic uncertainty are specified at the 95 % confidence limit, each value of U_r constitutes a 95 % confidence estimate of the overall error in the experimental result.

All of the uncertainties reported in Table 4.9 correspond to the measurement

Derived parameter	Uncertainty		
	Systematic	Random	Expanded
Probe temperature recovery factor (PRT)	3.639×10^{-3}	1.354×10^{-3}	3.882×10^{-3}
Probe temperature recovery factor (N-type)	3.639×10^{-3}	1.467×10^{-3}	3.923×10^{-3}
Probe pressure recovery factor	3.948×10^{-5}	3.963×10^{-4}	3.983×10^{-4}
Mach number	4.057×10^{-4}	3.611×10^{-3}	3.634×10^{-3}
Reynolds number	5.261×10^{1}	4.158×10^{2}	4.191×10^{2}

Table 4.9: The propagated uncertainties in derived results, determined at the experimental conditions in Table 4.1 (95 % confidence).

conditions outlined in Table 4.1, which represent a free-stream Mach number of 0.6 and ambient stagnation temperature of $288\,K$. These are the conditions at which the random and systematic uncertainties in each measured variable are defined in Tables 4.4 and 4.8 respectively.

CHAPTER 5

Temperature Sensor Performance

5.1 Introduction

In seeking to design a new stagnation temperature probe that will achieve an absolute measurement uncertainty close to the 0.1 % target, consideration must be given to the performance of the temperature sensor. This chapter provides a general description of two types of temperature sensor that are suitable for use in such an application. Firstly, attention is focused on thermocouples, which are commonly employed in gas turbine engine testing. Thermocouples offer a simple and low cost measurement solution, yet deliver poor measurement accuracy. Secondly, attention is shifted to platinum resistance thermometers (PRTs), which are less routinely employed in an engine test environment. PRTs offer similar advantages to thermocouples, but additionally deliver high measurement accuracy. For this reason, the adoption of PRTs in preference to thermocouples is recommended. This recommendation is supported by the results of a feasibility study, which addresses concerns over sensor calibration retention and vibration

sensitivity.

5.2 Thermocouples

In its simplest form, a thermocouple consists of a pair of wires that are drawn from two dissimilar metals. At one end, the wires are joined together to form a measuring junction. At the other, the wires are terminated at a voltage measuring instrument, which is referred to as the reference junction. This arrangement is illustrated by the circuit diagram in Figure 5.1.

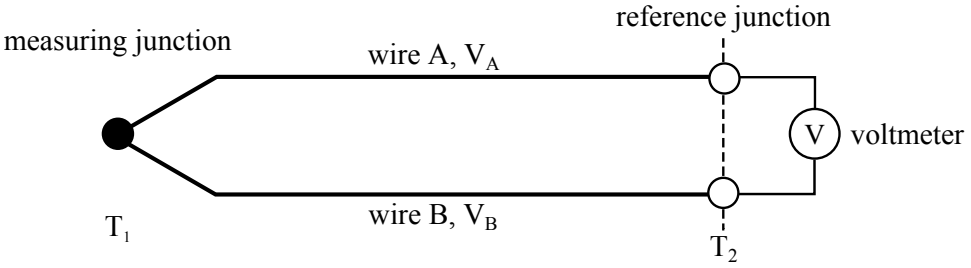

Figure 5.1: A schematic diagram of a simple thermocouple circuit.

When the thermocouple is exposed to a thermal gradient, an electromotive force (e.m.f) is generated in each wire due to the Seebeck effect (Seebeck, 1823). Since the magnitude of this e.m.f is a function of the wire material, a net e.m.f is registered at the voltmeter. This net e.m.f is related to the temperature difference along the thermocouple wires via equation 5.1. The coefficient S_{AB} is known as the effective Seebeck coefficient, which represents the sensitivity of the thermocouple to temperature change. This may be quantified through sensor calibration.

$$V_{net} = V_A - V_B = \int_{T2}^{T1} S_{AB} \cdot dT \tag{5.1}$$

To determine the temperature at the measuring junction (T_1) from equation 5.1, the temperature of the reference junction (T_2) must be known. This is typically established from an independent resistive temperature device (RTD), mounted inside the voltmeter close to the connection terminals. The introduction of this second temperature sensor leads to additional complexity in the measurement system. It also contributes a further source of uncertainty to the calculated measuring junction temperature. The requirement for a reference temperature measurement at the measuring instrument is therefore a significant weakness of the thermocouple method.

Another disadvantage of the thermocouple is its low thermoelectric response, which is approximately $40\,\mu V/K$ for a 'N' type device (Bentley, 1998b). This level of sensitivity makes the thermocouple signal difficult to measure with high accuracy. For example, a minimum temperature difference of just $0.25\,K$ can be measured using a typical voltmeter with $10\,\mu V$ resolution. The relatively weak thermocouple signal can also be readily corrupted by electrical noise. This can lead to errors in the indicated junction temperature under noisy operating conditions.

The final drawback of the thermocouple is its poor stability. This is attributed to the sensitive thermoelectric properties of the wires, which can be modified by exposure to high stresses or temperatures (Childs *et al.*, 2000). Such modifications alter the thermoelectric response of the sensor, which invalidates the established voltage-temperature calibration. Without a subsequent recalibration process, this can result in errors in the calculated junction temperature. This phenomenon is known as calibration drift.

One advantage of the thermocouple is its wide temperature range, which can ex-

tend from $3\,K$ to $2023\,K$ depending on the wire materials chosen (Childs *et al.*, 2000). This enables the thermocouple to be successfully employed in a variety of measurement applications. Another advantage of the thermocouple is the compact junction size ($\leq 1\,mm$), which essentially facilitates point temperature measurements. The small junction size also promotes a fast response time, which is desirable for monitoring temperature variations. Further benefits of the thermocouple include its low cost and simplicity of operation (self-generating signal). It is these practical qualities that motivate the extensive use of the thermocouple despite its limited measurement accuracy. However, these qualities are also possessed by a number of other temperature sensors, including PRTs. In certain applications, these alternative sensors may also offer an improvement in measurement accuracy compared to the thermocouple. For situations in which temperature measurement accuracy is important, viable alternatives to the thermocouple must consequently be explored.

5.3 Platinum resistance thermometers

PRTs exploit the temperature dependence of electrical resistance as a method for temperature measurement. This technique was originally developed by Callendar (1887), who described the resistance-temperature response of platinum (for $T \geq 0$) using equation 5.2. In this formulation, α and ζ are constants that may be determined by sensor calibration.

$$R_T = R_{273.15\,K}\left[1 + \alpha T + \zeta\left(\frac{T}{100}\right)\left(1 - \frac{T}{100}\right)\right] \tag{5.2}$$

The resistance-temperature response of platinum is both stable and repeatable

(Childs *et al.*, 2000). This makes PRTs ideal for high accuracy measurement applications, including those in thermal calibration systems. Traditionally, wire-wound PRTs have been used as laboratory reference standards, these being constructed from fine gauge platinum wire that is coiled around a ceramic core (Bentley, 1998a). However, problems related to vibration, together with a relatively large sensor size, have limited the widespread application of these devices.

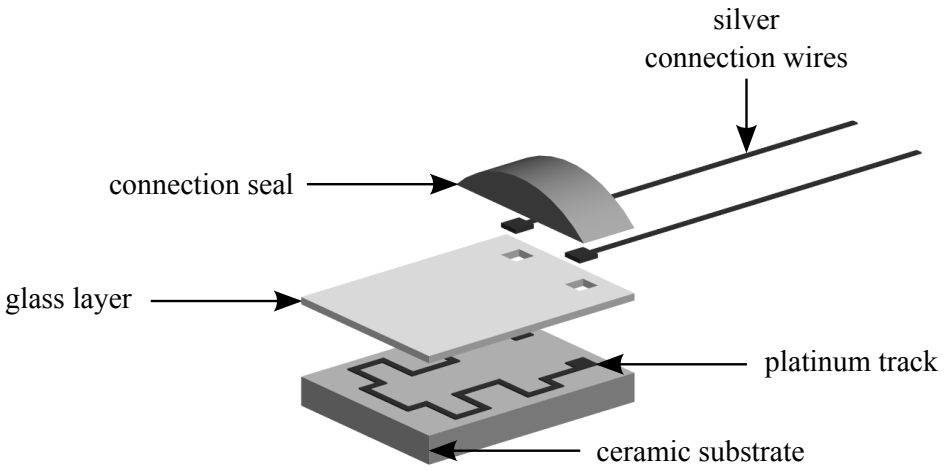

Figure 5.2: An exploded diagram of a thin-film PRT sensor.

The more recent availability of commercially produced miniature thin-film devices has allowed the consideration of PRTs in a more extensive range of applications (Gam *et al.*, 2011). The thin-film PRT (shown in Figure 5.2) consists of a ceramic substrate, which is overlaid with a thin platinum track. Silver connection wires ($\sim 10\,mm$ in length) are attached to the two ends of the track to facilitate resistance measurement. The platinised side of the ceramic, including the connection wire interface, is coated with a protective glass layer in order to prevent damage and corrosion. In common with other resistance thermometers, the thin-film device is constructed with a particular electrical resistance at $273.15\,K$ ($0\,^oC$). The value selected for industrial applications is typically $100\,\Omega$ (Bentley, 1998a).

To connect the thin-film PRT to a resistance measuring instrument, the two silver

connection wires commonly require extension. For high accuracy applications, a 4-wire configuration is employed, in which two extension leads are attached to each leg of the sensor. This arrangement is illustrated by the circuit diagram in Figure 5.3. In this circuit, one pair of leads connect the sensor to a constant current source. For a sensor of nominal $100\,\Omega$ resistance, this is typically adjusted to a value of $1\,mA$ (Childs *et al.*, 2000). The other pair of leads connect the sensor to a voltmeter with high input impedance ($\geq 100\,M\Omega$). This effectively eliminates the flow of current through the measuring branch of the circuit. The measured voltage is therefore principally dependent on the resistance of the sensor, with negligible contribution from the lead wires. Based on knowledge of the excitation current, this resistance may be determined from the voltage measurement using Ohm's law.

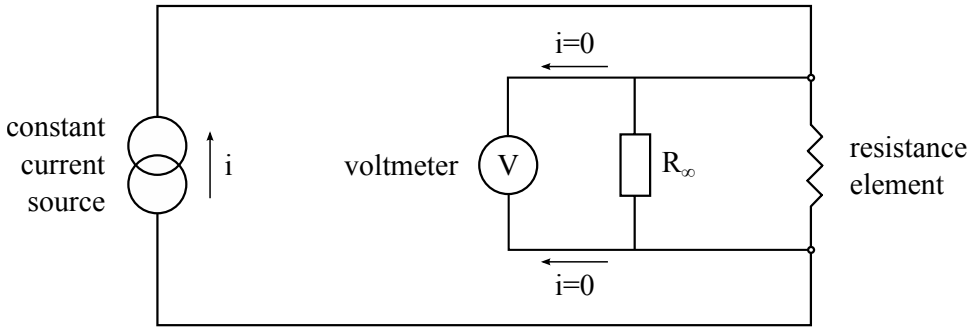

Figure 5.3: A 4-wire circuit for a PRT.

The miniature thin-film PRT offers superior accuracy to the thermocouple in certain temperature measurement applications. This enhanced performance may be attributed to three main factors. Firstly, the output signal of the thin-film PRT is solely dependent on the temperature of the platinum sensing element. Unlike the thermocouple, this implies that knowledge of a reference temperature at the measuring instrument is not required (see section 5.2). As a consequence, the complexity of the measurement system is reduced and a potential source of temperature error is eliminated. Secondly, the thin-film PRT has a thermoelec-

tric response that is an order of magnitude higher than that of the thermocouple (see section 5.2). A $100\,\Omega$ sensor supplied with an excitation current of $1\,mA$ has a typical sensitivity of $400\,\mu V/K$ (Childs *et al.*, 2000). Disturbances from sources such as electrical noise are therefore less likely to introduce errors into the temperature measurement. Finally, due to the selection of platinum as the temperature sensitive element, the thin-film PRT offers superior stability compared to the thermocouple. Platinum is renowned for possessing stable thermoelectric properties that promote sensor calibration retention (Bentley, 1998a). Accordingly, temperature measurements exhibit excellent repeatability over time.

The primary disadvantage of the thin-film PRT is its temperature capability, which is constrained by material properties to approximately $673\,K$ (Saravanamuttoo, 1990). This limit is around one-third of the maximum temperature rating of the thermocouple (see section 5.2), which restricts applications of the PRT to the low and intermediate pressure regions of a gas turbine engine (see Table 2.1). Another drawback of the thin-film PRT is its physical size, which is necessarily much larger than that of the thermocouple. This places limitations on the achievable time response, as well as the spatial measurement resolution. Finally, the thin-film PRT is known to suffer from hysteresis in the resistance-temperature characteristic, caused by repeated thermal cycling (Childs *et al.*, 2000). This hysteresis could potentially compromise measurement accuracy in applications that involve large temperature variations. However, its impact has been reported to be less than $0.05\,K$ following a small number of initial thermal cycles between $273.15\,K$ and $773.15\,K$ (Gam *et al.*, 2011).

5.4 Stagnation temperature measurements

The measurement of stagnation temperature in gas turbine engines relies on the extensive use of passively ventilated thermocouple probes (see section 2.1.2). The application of thermocouples is primarily motivated by practical considerations that include low cost, simplicity of operation and ease of installation within compact probe assemblies. The application of thermocouples is also driven by their wide operational temperature range, which is compatible with a large number of engine measurement locations. Unfortunately, the engine test environment tends to limit the measurement accuracy that is attainable using thermocouples (see section 2.2.1). This is related to a combination of factors that includes the limited accuracy of the test-bed reference junction, signal corruption caused by electrical noise and calibration drift induced by exposure to high temperature and stress. Together with probe temperature recovery performance, these factors limit the stagnation temperature uncertainty to a value of $\pm 0.5\,\%$ [1].

Historically, the measurement accuracy delivered by passively ventilated thermocouple probes has been adequate to evaluate gains in turbomachinery efficiency. Today, the achievable efficiency gains are sufficiently small that improvements in measurement accuracy are required (see section 1.1). This has led to the specification of a target absolute stagnation temperature uncertainty of $\pm 0.1\,\%$ (see section 2.1.5). To satisfy this uncertainty target, consideration has been given to the application of thin-film PRTs as an alternative to thermocouples (Erlund, 2012). In certain measurement locations, it is anticipated that thin-film PRTs will deliver a relative improvement in measurement accuracy. This is a consequence of a number of factors that includes the elimination of the test-bed

[1] Private communication: Mark Erlund, Measurement Specialist, Rolls-Royce plc.

reference junction, low sensitivity to electrical noise and reduced susceptibility to calibration drift. Together, these factors will facilitate the achievement of absolute stagnation temperature uncertainties that are closer to the $\pm 0.1\,\%$ target.

5.5 Feasibility study for thin-film PRTs

To encourage the adoption thin-film PRTs, a feasibility study has been conducted to demonstrate their suitability for use in gas turbine stagnation temperature probes. This study has included the identification of an appropriate sensor model, as well as analyses of static calibration retention and vibration sensitivity. These matters are described in sections 5.5.1 to 5.5.3 respectively.

5.5.1 Sensor selection

The initial study into the use of thin-film PRTs in stagnation temperature probes has focussed on the selection of an appropriate sensor. This choice is largely determined by the sensor size, which must be minimised in order to facilitate installation within the probe assembly (see section 2.1.2). Based on this requirement, the Minco S100144PD12 has been identified as a favourable option (Erlund, 2012). This sensor (pictured in Figure 5.4) has a plan-form area of $1.3 \times 1.7\,mm^2$ and a thickness of $0.7\,mm$. These dimensions are ideal for compact probe assemblies, which typically feature internal diameters $\leq 5\,mm$ (Saravanamuttoo, 1990).

The Minco S100144PD12 has an operational temperature capability that extends from $223\,K$ to $673\,K$. As a consequence, it may be successfully employed in stag-

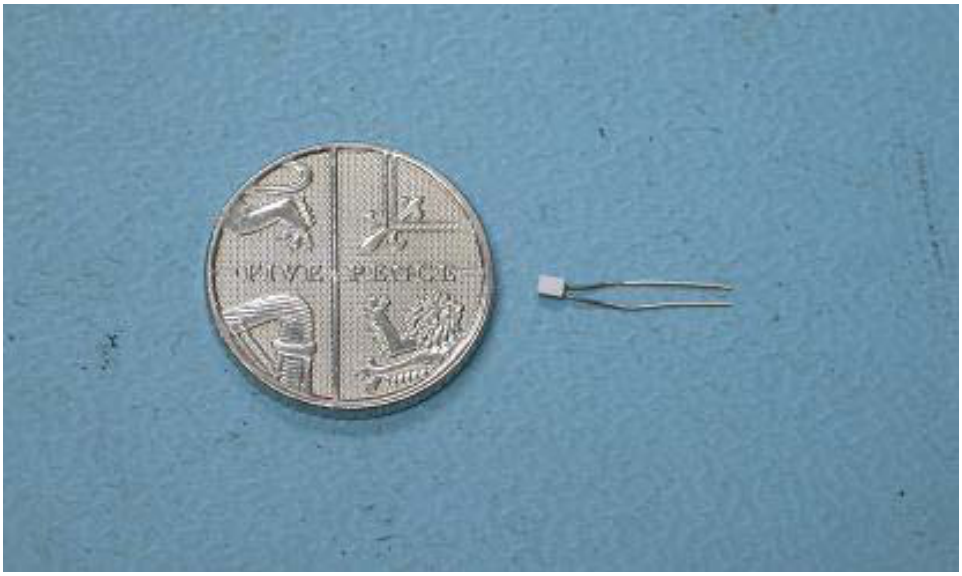

Figure 5.4: A photograph of the Minco S100144PD12 (Erlund, 2012).

nation temperature probes that are located between the inlet flow-screen to the rear of the intermediate pressure compressor (see Table 2.1). Initially, applications of the Minco S100144PD12 are intended for measurement locations around the fan. This includes the fOGV and ESS, together with the T210 rake (see Figure 2.3). In these locations, the flow stagnation temperature is sufficiently low ($\approx 300\,K$) that the target $\pm 0.1\,\%$ measurement uncertainty ($0.3\,K$) is extremely difficult to achieve.

5.5.2 Static calibration repeatability

In order to deliver accurate stagnation temperature measurements, the Minco S100144PD12 must exhibit stable and repeatable performance. To evaluate these characteristics, a series of static calibrations have been conducted on a randomly selected sensor from a production sample. The temperature range considered in this exercise extends from $283\,K$ to $303\,K$, which is representative of typical measurement conditions encountered in the fan (see Table 2.1). The static cal-

ibrations have been performed using a suite of thermal calibration equipment, which is comprised of a semi-standard reference PRT probe, an Isotech TTI-7 resistance measuring instrument and an Isotech Europa stirred water bath. The response of the Minco S100144PD12 has been recorded using a Pico PT-104 resistance measuring instrument, connected in 4-wire configuration. Further details of this measuring equipment is provided in sections 3.3.1 and 3.3.3.

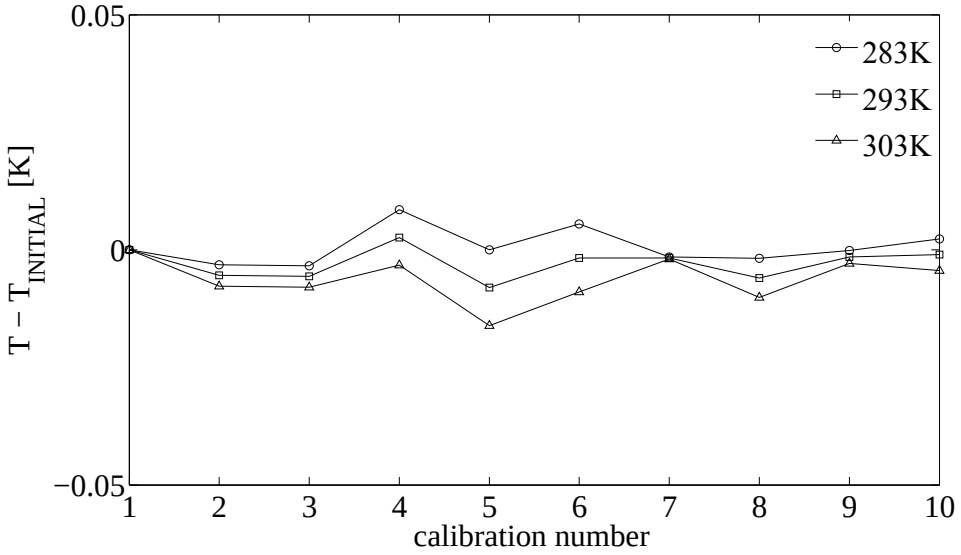

Figure 5.5: Repeat static calibration tests of a miniature thin-film PRT sensor plotted relative to an initial reference calibration (data acquired over a 4-month period).

Figure 5.5 shows data from 10 sensor calibrations that were performed over a period of four months. The data is presented as the change in indicated temperature relative to the initial sensor calibration, for nominal temperature conditions of $283\,K$, $293\,K$ and $303\,K$. The results reveal a maximum deviation in indicated temperature of less than $0.015\,K$ (0.005%), signifying excellent stability and repeatability. This figure is comparable to the uncertainty associated with the temperature measuring equipment, which has been quantified in section 4.3.

5.5.3 Sensitivity to vibration

To be suitable for use in an engine test environment, the Minco S100144PD12 must exhibit low sensitivity to vibration. In order to evaluate this sensitivity, the performance of the sensor has been examined following periods of vibration delivered by an electro-dynamic shaker. The shaker has been configured to oscillate the sensor at a frequency of 100 Hz, with a sinusoidal displacement of 1 mm (peak-peak) and a maximum acceleration of 20 g. This corresponds to a vibration condition typically experienced by core-mounted engine instrumentation [2]. After prescribed intervals of vibration, the sensor has been statically calibrated in order to identify any change in performance. These calibrations have utilised the same measuring equipment that is described in section 5.5.2.

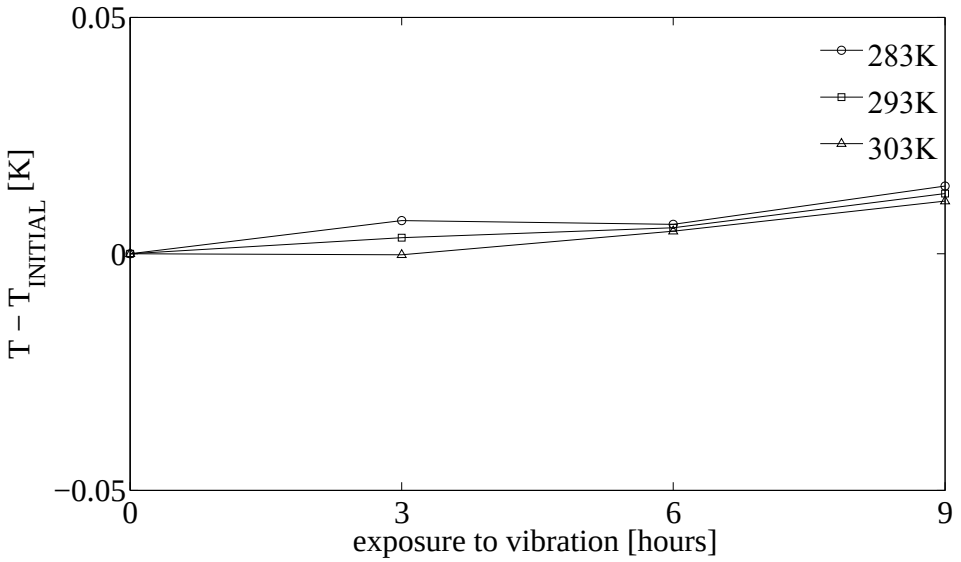

Figure 5.6: Repeat static calibration tests of a miniature thin-film PRT sensor, after periods of 3, 6 and 9 hours of vibration, plotted relative to an initial reference calibration.

Figure 5.6 shows data from sensor calibrations that were performed after 3, 6 and 9 hours of vibration. The data is presented as the change in indicated

[2]Private communication: Richard Stevenson, Measurement Specialist, Rolls-Royce plc.

temperature relative to an initial sensor calibration obtained prior to vibration (0 hours). At nominal temperature conditions of $283\,K$, $293\,K$ and $303\,K$, the sensor appears to show little evidence of vibration sensitivity. The observed temperature deviations are of a similar magnitude to those recorded in the study of sensor calibration retention (see Figure 5.5).

CHAPTER 6

Probe Temperature Recovery Performance

6.1 Introduction

In order to approach the target absolute measurement uncertainty of 0.1 %, the new stagnation temperature probe must be designed to achieve high temperature recovery performance. This chapter considers the role of conductive and convective heat transfer mechanisms in determining the temperature recovery performance of stagnation temperature probes that incorporate thin-film PRT sensors. Firstly, attention is focused on a stainless-steel probe, which exhibits a low temperature recovery factor that varies with both free-stream Mach and Reynolds number. This probe is similar to the passively ventilated thermocouple probes that are commonly used in gas turbine engine testing. Secondly, attention is shifted to an acrylic probe, which exhibits a comparatively higher temperature recovery factor that is insensitive to both free-stream Mach and Reynolds num-

ber. This probe is geometrically identical to the stainless-steel probe, differing only in regard to the thermal conductivity of the probe body. Based on this result, the adoption of a low thermal conductivity design is recommended for PRT probes that require high temperature recovery performance.

6.2 Stagnation temperature probe designs

In order to obtain an accurate indication of flow stagnation temperature, the temperature sensing device must be located in a region of low velocity (see section 2.1.1). In an engine environment, the provision of such a condition is complicated by the generally high-subsonic Mach number of the flow ($\geq$ Mach 0.6). As a consequence, the temperature sensor is typically installed within a vented stagnation tube (see section 2.1.2). The stagnation tube acts to decelerate the flow over the sensor to a sufficiently low velocity ($\leq$ Mach 0.25) that temperature recovery effects are reduced to a low level (Markowski and Moffatt, 1948).

6.2.1 Temperature probe

Figures 6.1 and 6.2 show a stagnation temperature probe that incorporates a thin-film PRT sensor. This design is based on the passively ventilated thermocouple probe that is used extensively in gas turbine engine testing (see Figure 2.1). In this instance, the thermocouple has been replaced by a thin-film PRT in order to facilitate the attainment of higher measurement accuracy (see section 5.4). Future references to this device will use the designation *Baseline* PRT probe.

In the *Baseline* probe design, the thin-film PRT is shrouded by a stainless-steel

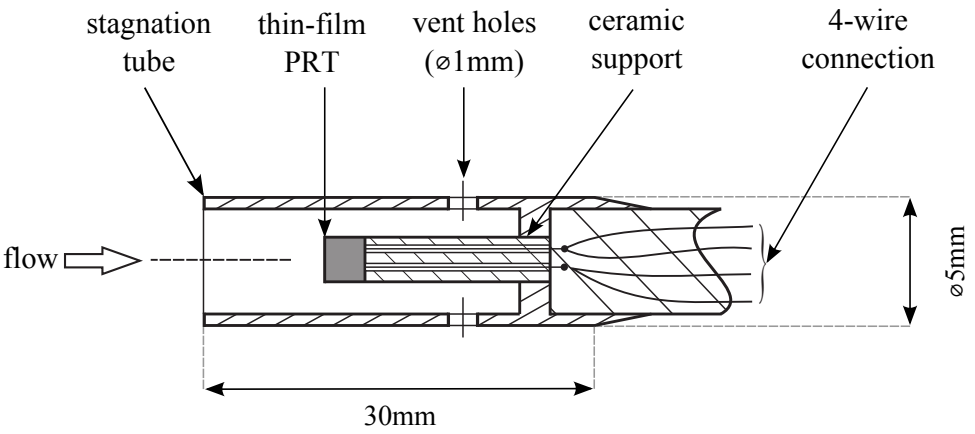

Figure 6.1: A schematic diagram of a stagnation temperature probe incorporating a thin-film PRT sensor. This design is referred to as the *Baseline* PRT probe.

Figure 6.2: A photograph of the *Baseline* PRT probe.

stagnation tube with an outer diameter of $5\,mm$. Air is drawn through the device using a pair of $1\,mm$ diameter vent holes, located towards the rear of the stagnation tube. The thin-film PRT is bonded to a short ceramic (mullite) support, which contains two fine-bore holes that accommodate the sensor lead wires. At the rear of the ceramic support, a pair of extensions are attached each lead wire to create a 4-wire connection. The ceramic support offers both electrical and thermal insulation. This is important for electrically isolating the sensor lead wires, as well as reducing thermal conduction between the sensor and the stagnation tube.

6.2.2 Combined pressure and temperature probe

An equivalent probe for the combined measurement of stagnation pressure and temperature is shown in Figures 6.3 and 6.4. Apart from the addition of a Pitot tube, this design closely resembles that of the *Baseline* PRT probe. Future references to this device will use the designation combination *Baseline* PRT probe.

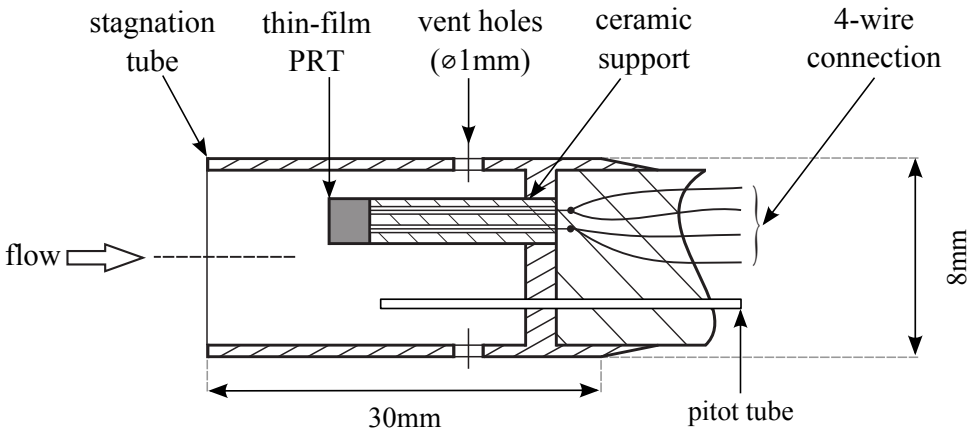

Figure 6.3: A schematic diagram of a combined stagnation pressure and temperature probe incorporating a thin-film PRT sensor. This design is referred to as the combination *Baseline* PRT probe.

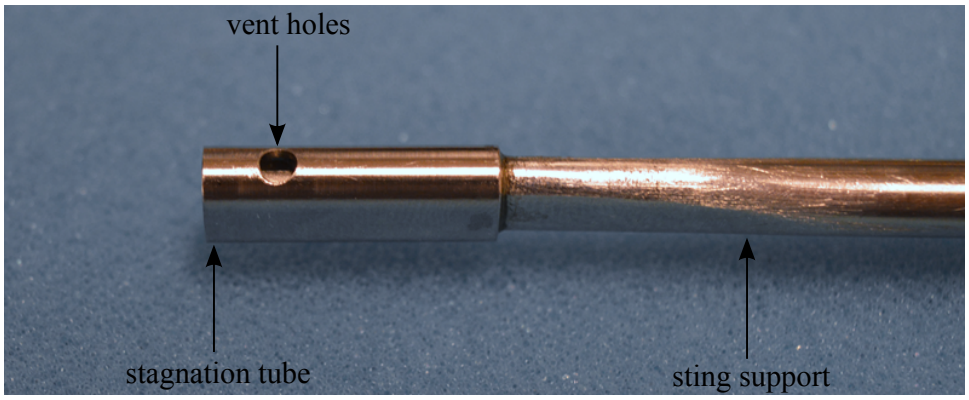

Figure 6.4: A photograph of the combination *Baseline* PRT probe.

To accommodate the installation of a Pitot tube alongside the thin-film PRT, the combination *Baseline* PRT probe utilises an oval stagnation tube. The cross-sectional dimensions of this tube are approximately $5\,mm$ by $8\,mm$. The internal diameter of the Pitot tube is approximately $1\,mm$.

6.3 Baseline PRT probe

To investigate the temperature recovery performance of the *Baseline* PRT probe, two sensitivity studies have been conducted using the Loughborough University probe aerodynamic calibration facility. The results of these studies are reported in sections 6.3.1 and 6.3.2 for free-stream Mach and Reynolds number sensitivities respectively.

6.3.1 Mach number sensitivity

Figure 6.5 shows the temperature recovery factor (blue) and stagnation temperature measurement shortfall (red) for the *Baseline* PRT probe, plotted as a function of free-stream Mach number. This data has been gathered under atmospheric conditions ($T_{o,\infty} \approx 300\,K$ and $P_{\infty} \approx 1\,bar$), with the calibration facility operating in a free-jet configuration. The probe has been tested in a sting-mounted arrangement (as indicated in Figure 3.4), at zero flow incidence angle.

The temperature recovery factor of the *Baseline* PRT probe varies between 0.85 and 0.89 over the Mach number range considered. These values correspond to stagnation temperature measurement shortfalls of $1.09\,K$ and $3.19\,K$ respectively. These shortfalls are sufficiently large that post-test measurement corrections must be applied to the probe indicated temperatures in order to determine accurate stagnation values. These measurement corrections are based on the probe temperature recovery factor and are calculated using equation 6.1.

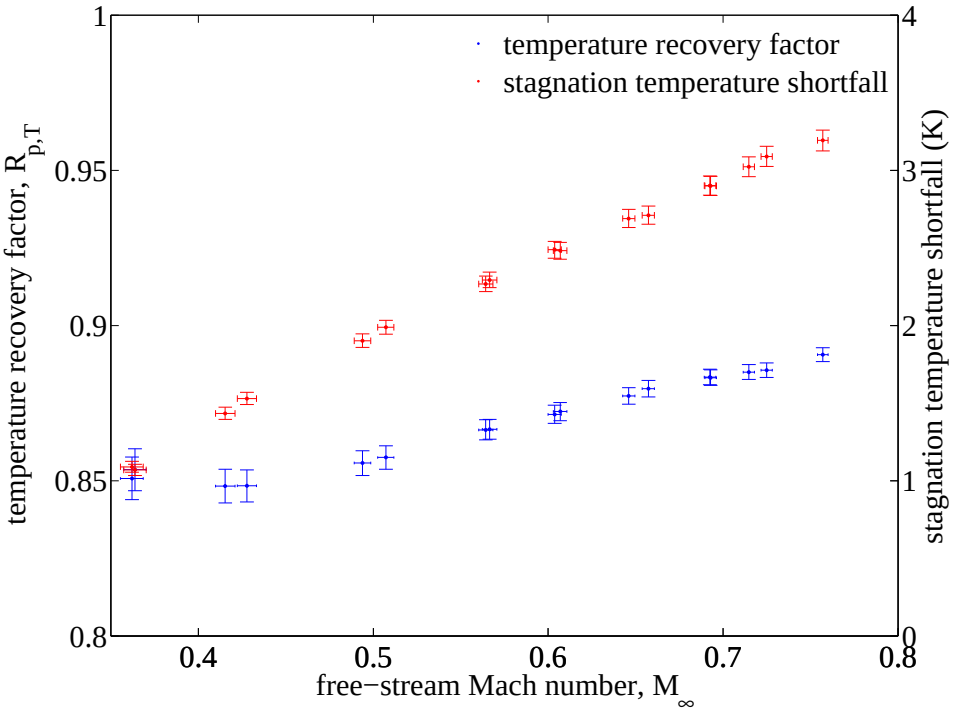

Figure 6.5: A graph showing the measured temperature recovery factor, $R_{p,T}$, and the stagnation temperature shortfall of the Baseline PRT probe as a function of free-stream Mach number (sting-mounted, zero flow incidence, ambient static pressure).

$$T_{o,\infty} = \frac{T_{ind} + T_{\infty}(R_{p,T} - 1)}{R_{p,T}} \tag{6.1}$$

Since the probe temperature recovery factor is established from an aerodynamic calibration procedure, its value is subject to experimental uncertainties. These uncertainties necessarily propagate to the measurement correction and consequently limit the accuracy of the corrected stagnation temperature. In order to achieve the target absolute stagnation temperature uncertainty of 0.1 %, the uncertainty associated with the measurement correction must remain small. This essentially requires the magnitude of the measurement correction to be reduced to a low level. Accordingly, an alternative to the *Baseline* PRT probe must be identified that will deliver significantly higher temperature recovery performance

($R_{p,T} \approx 1$).

6.3.2 Reynolds number sensitivity

The results presented in Figure 6.5 indicate that the temperature recovery factor of the *Baseline* PRT probe increases with free-stream Mach number condition. It is hypothesised that this behaviour is related to the rate of convective heat transfer to the PRT sensor, which increases with Mach number due to the necessary increase in Reynolds number (see section 2.2.3.3). In order to verify this hypothesis, the probe temperature recovery factor has been determined over a range of Mach numbers at different static pressure conditions. This has enabled the effects of Reynolds number to be investigated alongside the effects of Mach number.

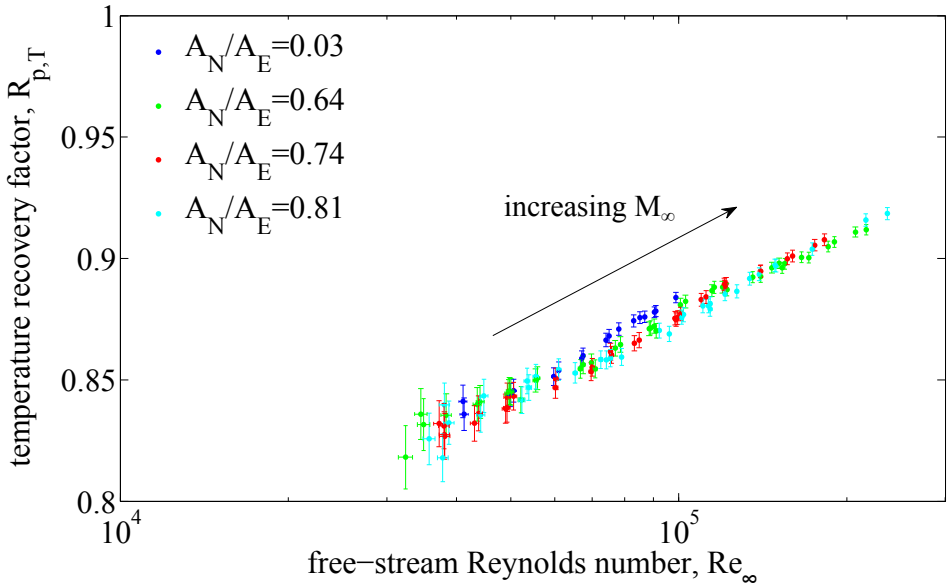

Figure 6.6: A graph showing the measured temperature recovery factor, $R_{p,T}$ of the Baseline PRT probe as a function of free-stream Reynolds number (sting-mounted, zero flow incidence).

Figure 6.6 shows the temperature recovery factor of the *Baseline* PRT probe

plotted as a function of free-stream Reynolds number. These results have been acquired with the calibration facility operating in a enclosed-jet configuration. This has enabled changes in static pressure to be realised by manipulating the ratio between the nozzle area and the resistor plate area (A_N/A_E). Four different area ratios have been considered in this instance, corresponding to values of 0.03 (ambient static pressure), 0.64, 0.74 and 0.81. At each area ratio, the free-stream Mach number has been varied between values of 0.3 and 0.75. For each free-stream Mach number, results have therefore been acquired at four different Reynolds number conditions.

From Figure 6.6, it clear that the probe temperature recovery factors determined at each value of A_N/A_E collapse on to a single curve that is a function of free-stream Reynolds number. The general increase that is observed in probe temperature recovery factor therefore arises due to increases in Reynolds number, rather than increases in Mach number. This result supports the hypothesis that the temperature recovery performance of the *Baseline* PRT probe is sensitive to convective heat transfer effects. At higher Reynolds number conditions, the convective heat transfer coefficient, h, at the surface of the PRT sensor is necessarily greater. Accordingly, there is an increase in the rate of heat transfer to the sensor from the surrounding (near-stagnated) gas. A high rate of convective heat transfer is beneficial to temperature recovery performance, since it counteracts the detrimental impact of conductive heat transfer to the probe body (see section 2.2.3.1). As a consequence, an increase in the probe temperature recovery factor is observed at higher free-stream Reynolds number conditions. The balance between convective and conductive heat transfer mechanisms is therefore a controlling influence on the temperature recovery performance of the *Baseline* PRT probe.

6.4 Thermal conduction effects

The results presented in section 6.3 have demonstrated that the temperature recovery performance of the *Baseline* PRT probe is influenced by the balance between convective and conductive heat transfer mechanisms (see section 2.2.2). The conductive heat transfer mechanism is driven by a temperature difference between gas surrounding the PRT sensor and gas flowing over the external surfaces of the probe. Since the PRT sensor is located in a region of low velocity ($\leq$ Mach 0.25), the gas temperature is close to the free-stream stagnation value. Conversely, since the external surfaces of the probe are exposed to high velocities (generally $\geq$ Mach 0.6), recovery effects limit the wall temperature to below the free-stream stagnation value. In an effort to characterise the gas recovery temperature, an experiment has been conducted to measure the adiabatic wall temperature, T_w, on the external surfaces of a probe-like body. The details of this experiment are reported in sections 6.4.1 and **??**.

6.4.1 Thin-walled cylinder

To simplify measurements of the adiabatic wall temperature, a plain cylinder has been used to approximate the external geometry of the *Baseline* PRT probe. Figure 6.7 shows a schematic diagram of the plain cylinder, which is instrumented internally at 8 axial locations using miniature 'K' type thermocouples. The cylinder is constructed from thin-walled ($0.2\,mm$) stainless steel tubing with an outer diameter of $6.35\,mm$. The thin-walled tube provides a near-adiabatic wall condition, with low levels of heat transfer through the cylinder surface into the internal stagnant air pocket. The leading edge of the cylinder is sealed with an acrylic cap that restricts heat transfer from the forward stagnation point.

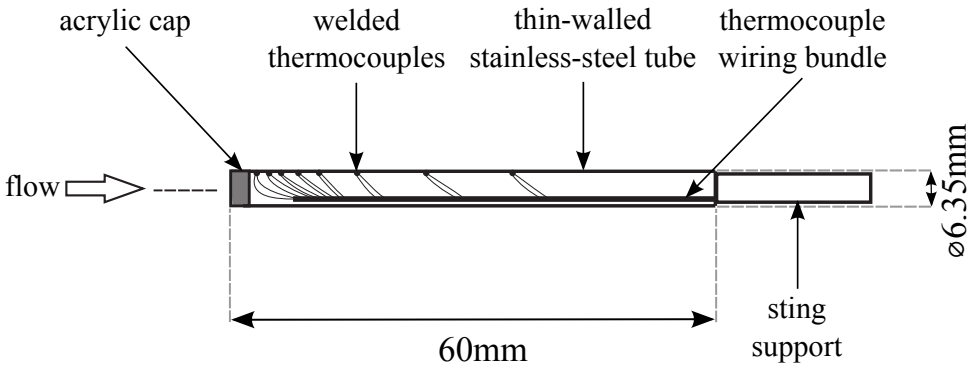

Figure 6.7: A schematic diagram of the thin-walled stainless-steel cylinder used for determining gas recovery temperatures near the outer surfaces of stagnation tubes.

6.4.2 Cylinder adiabatic wall temperature

Measurements of the cylinder adiabatic wall temperature (gas recovery temperature) have been acquired over a range of free-stream Mach numbers using the Loughborough University probe aerodynamic calibration facility. These measurements have been gathered under atmospheric conditions ($T_{o,\infty} \approx 300\,K$ and $P_\infty \approx 1\,bar$), with the calibration facility operating in a free-jet configuration. The cylinder has been tested in a sting-mounted arrangement, at zero flow incidence angle.

Figure 6.8 shows measurements of the cylinder adiabatic wall temperature plotted in terms of the wall temperature recovery factor, $R_{w,T}$. The recovery factor has been determined from equation 6.2, using knowledge of the free-stream static and stagnation temperatures.

$$R_{w,T} = \frac{T_w - T_\infty}{T_{o,\infty} - T_\infty} \tag{6.2}$$

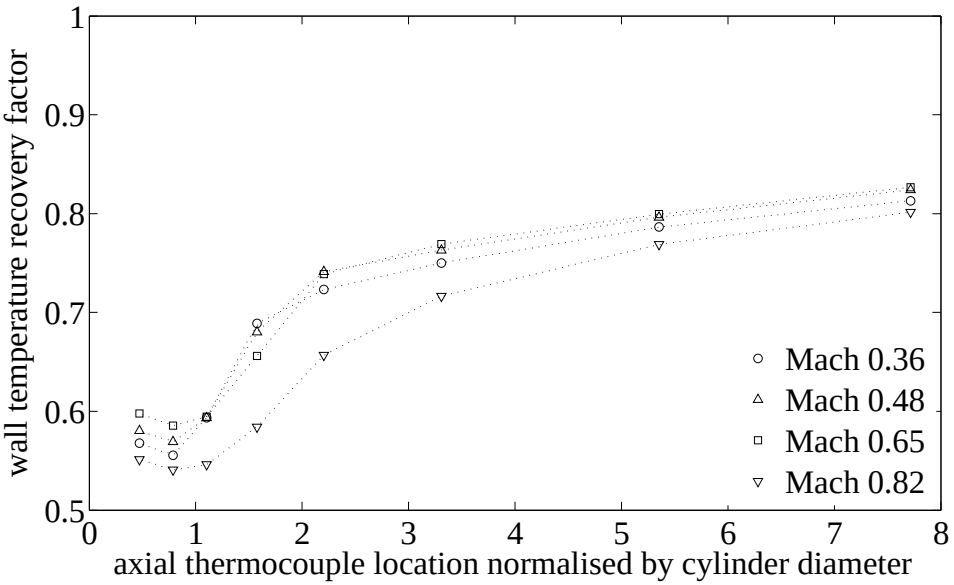

Figure 6.8: A graph showing measurements of the temperature recovery factor on the wall of the thin-walled stainless-steel cylinder as a function of axial position.

From this data, a significant variation in adiabatic wall temperature along the length of the cylinder can be observed. Close to the leading edge, there is a low wall temperature that corresponds to a recovery factor of approximately 0.6. Further downstream, the wall temperature increases, eventually yielding a recovery factor of approximately 0.82. Based on the schlieren photograph shown in Figure 6.9, the region of particularly low adiabatic wall temperature appears to correspond to the leading edge separation. Downstream of the separation, the adiabatic wall temperature rises to a level that is characteristic of flow over a flat plate (Benedict, 1984).

6.4.3 Tapered leading edge modification

To eliminate the region of particularity low adiabatic wall temperature at the leading edge of the cylinder, a 10^o taper was added to the acrylic cap in order to prevent separation. Figure 6.10 shows measurements of the cylinder adiabatic

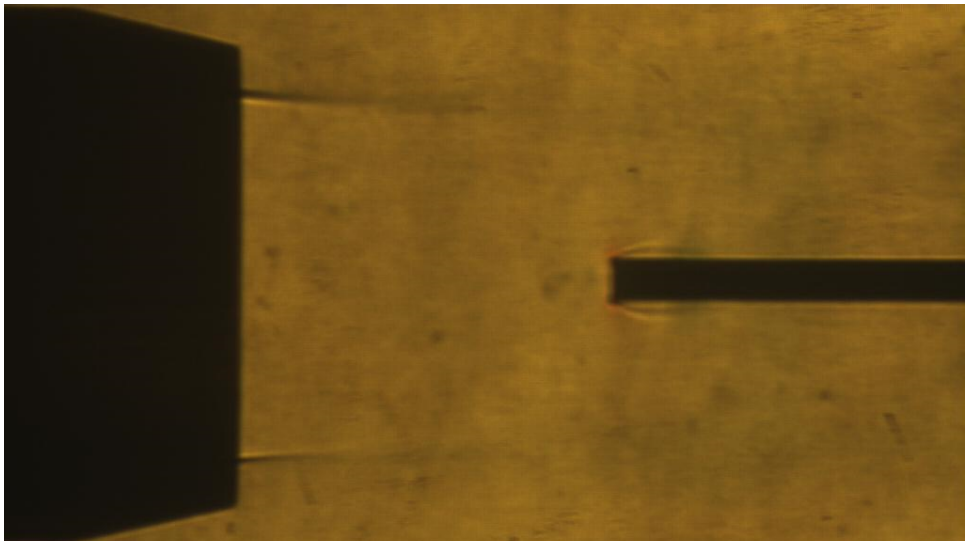

Figure 6.9: A schlieren photograph showing the thin-walled cylinder at a free-stream Mach number of 0.8.

wall temperature following this modification.

By comparing the results in Figure 6.10 to those shown in Figure 6.8, it is clear that the addition of the leading edge taper has resulted in a local increase in adiabatic wall temperature. At the cylinder leading edge, recovery factors increase from 0.6 in the blunt case to 0.8 in the tapered case. Since separation is circumvented in the tapered case, this outcome supports the hypothesis that the region of particularly low adiabatic wall temperature towards the leading edge of the blunt cylinder is associated with separation effects.

For both geometries tested, the recovery factors are indicative of substantial differences between the cylinder wall temperature and the free-stream stagnation temperature. At a free-stream Mach number of 0.6, the average temperature difference along the length of the cylinder corresponds to $6.95\,K$ in the blunt case and $4.04\,K$ in the tapered case (for $T_{o,\infty} = 300\,K$). In stagnation temperature probes, these temperature differences would drive conductive heat transfer between the sensor and the stagnation tube (see section 2.2.3.1). Both blunt

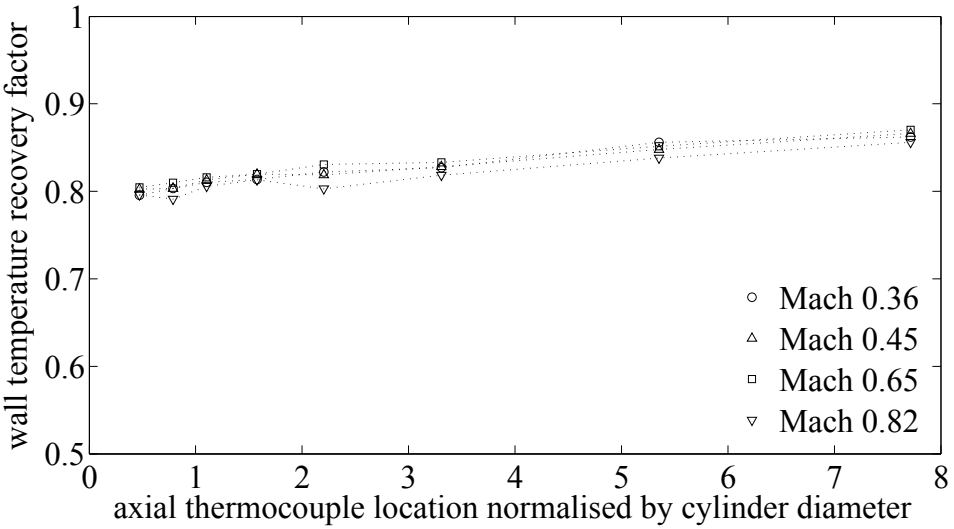

Figure 6.10: A graph showing measurements of the temperature recovery factor on the wall of the thin-walled stainless-steel cylinder, following the addition of a 10^o taper to the acrylic cap.

and tapered probe geometries would therefore be associated with high levels of conduction, which would ultimately lead to significant shortfalls in indicated stagnation temperature. In seeking to decrease the magnitude of these shortfalls, methods of reducing conductive heat transfer must therefore be explored.

6.5 Acrylic PRT probe

Section 6.4 has described the thermal boundary conditions that are responsible for the detrimental effects of conductive heat transfer in stagnation temperature probes. In order to reduce the impact of these conduction effects, a common approach is to increase the rate convective heat transfer to the temperature sensor (see for example Moffat, 1962). This is achieved by increasing the flow velocity in the stagnation tube by enlarging the vent hole area. Unfortunately, the benefits of this approach are eventually negated by temperature recovery effects acting on the sensor, which worsen with increasing flow velocity (see section 2.2.3.3).

An alternative method to reduce the impact of thermal conduction is to construct the probe from materials of low thermal conductivity (see for example Mullikin, 1941). To demonstrate the potential benefits of this approach, a version of the *Baseline* PRT probe has been constructed with an acrylic stagnation tube. This acrylic probe is geometrically identical to the *Baseline* probe (pictured in Figure 6.1), differing only in regard to the thermal conductivity of the probe body. The thermal conductivity of acrylic ($k = 0.2\,W/mK$) is approximately 80 times lower than the thermal conductivity of stainless-steel ($k = 16\,W/mK$). The acrylic probe will therefore permit less conductive heat transfer through the probe body in comparison with the *Baseline* probe.

In order to investigate the impact of this low conductive heat transfer on probe temperature recovery performance, the two sensitivity studies described in section 6.3 have been repeated using the acrylic PRT probe. The results of these studies are reported in sections 6.5.1 and 6.5.2 for free-stream Mach and Reynolds number sensitivities. The practical limitations of the acrylic PRT probe are described in section 6.5.3.

6.5.1 Mach number sensitivity

Figure 6.11 shows the temperature recovery factor of the acrylic PRT probe, plotted alongside the temperature recovery factor of the *Baseline* PRT probe (also shown in Figure 6.5). Both data sets have been gathered under atmospheric conditions ($T_{o,\infty} \approx 300\,K$ and $P_\infty \approx 1\,bar$), with the calibration facility operating in a free-jet configuration. The probes have both been tested in a sting-mounted arrangement, at zero flow incidence angle.

Over the free-stream Mach number range considered, the temperature recovery

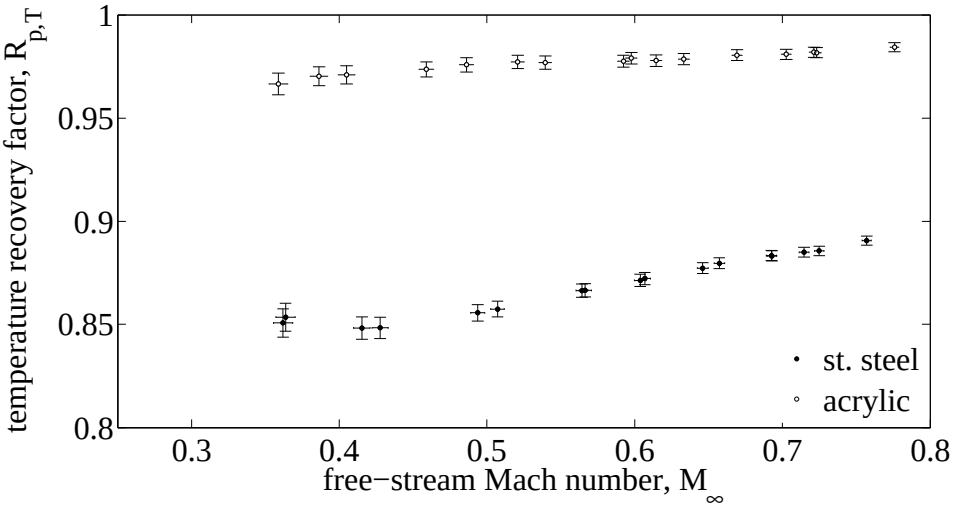

Figure 6.11: A graph showing the measured temperature recovery factor, $R_{p,T}$ of the Baseline PRT probe as a function of free-stream Mach number for both stainless-steel and acrylic bodied probes (sting-mounted, zero flow incidence, ambient static pressure).

factor of the acrylic probe varies between 0.96 and 0.98. These values correspond to stagnation temperature measurement shortfalls of $0.21\,K$ and $0.78\,K$ respectively. These shortfalls are sufficiency small that low levels of post-test measurement correction are required. This is beneficial to the overall accuracy of the corrected stagnation temperature, since the uncertainty introduced by the measurement correction will remain small.

Due to the considerable difference in the magnitude of post-test measurement corrections, the acrylic PRT probe will deliver a higher level of stagnation temperature accuracy compared to the *Baseline* PRT probe (see section 6.3.1). Since the two probes are geometrically identical and differ only in the thermal properties of the stagnation tube, this outcome is attributed to a reduction in conductive heat transfer effects. In seeking to achieve the target absolute stagnation temperature uncertainty of $0.1\,\%$, the adoption of a low thermal conductivity probe design is therefore recommended.

6.5.2 Reynolds number sensitivity

Figure 6.12 shows the temperature recovery factor of the acrylic PRT probe plotted as a function of free-stream Reynolds number. This data has been gathered with the calibration facility operating in an enclosed-jet configuration, using four different nozzle to restrictor plate area ratios (A_N/A_E). The probe has been tested in a sting-mounted arrangement, at zero flow incidence angle.

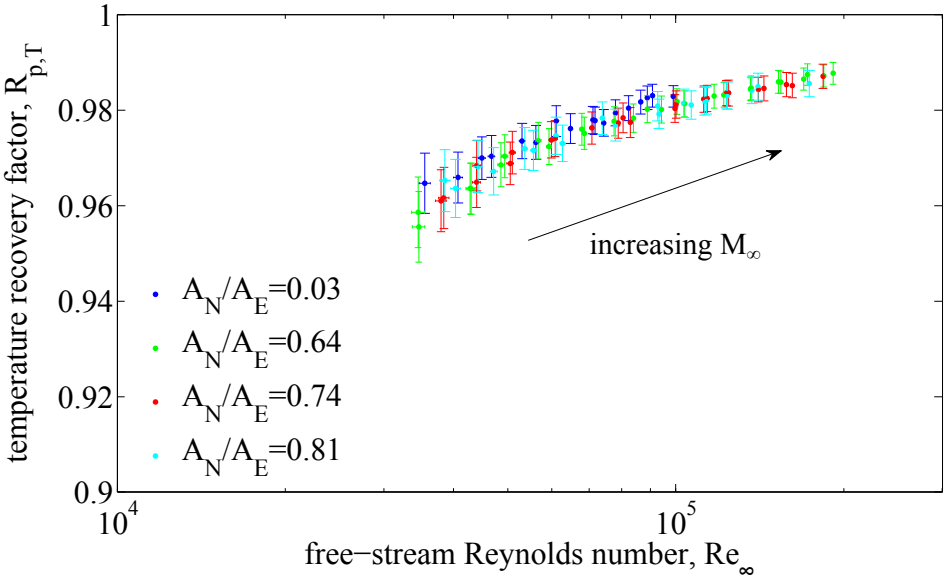

Figure 6.12: A graph showing the measured temperature recovery factor, $R_{p,T}$ of the acrylic-bodied PRT probe as a function of free-stream Reynolds number (sting-mounted, zero flow incidence).

The acrylic PRT probe exhibits low sensitivity to free-stream Reynolds number, with the temperature recovery factor varying between values of 0.96 at $Re_\infty = 35,000$ and 0.99 at $Re_\infty = 190,000$. This result indicates that the performance of the probe is insensitive to the rate of convective heat transfer to the PRT sensor, which is proportional to the free-stream Reynolds number. At higher Reynolds number conditions, the convective heat transfer coefficient, h, at the surface of the PRT is necessarily greater. Accordingly, there is an increase in the rate of heat

transfer to the sensor from the surrounding (near-stagnated) gas. In this instance, a high rate of convective heat transfer has little impact on probe temperature recovery performance, since the detrimental effects of conductive heat transfer to the probe body have been reduced to a low level. As a consequence, the temperature recovery factor of the acrylic PRT probe remains approximately constant with variations in Reynolds number. In contrast to the *Baseline* PRT probe, this suggests that the temperature recovery performance of the acrylic probe is not governed by the balance between convective and conductive heat transfer mechanisms. Rather, it is determined by temperature recovery effects of the flow over the sensor.

6.5.3 Practical limitations

The acrylic PRT probe demonstrates the importance of limiting conductive heat transfer effects in order to attain high levels of stagnation temperature accuracy. Unfortunately, in an engine test environment, the application of the acrylic PRT probe would be impractical. Due to the harsh engine operating conditions, the materials used in probe construction must possess a high temperature capability (acrylic $\leq 440\,K$). The materials must also be sufficiently robust to withstand engine vibration and foreign object damage. As a consequence, an alternative probe design is required that will limit conductive heat transfer effects without the application of low thermal conductivity materials. This has led to the development of the dual-skin PRT probe, which is described in chapter 7.

CHAPTER 7

New Dual-skin PRT Probes

7.1 Introduction

The preceding two chapters have considered the impact of temperature sensor performance and probe temperature recovery performance on the accuracy of stagnation temperature measurements. In order to approach the target absolute stagnation temperature uncertainty of 0.1 %, the application of thin-film PRT sensors (chapter 5) and the adoption of low conductivity probe designs (chapter 6) have both been recommended. This chapter presents details of new dual-skin PRT probes, which have been specifically developed in response to these recommendations. Firstly, attention is focussed on a dual-skin probe that is intended solely to acquire stagnation temperature measurements. This probe offers superior temperature recovery performance relative to the *Baseline* PRT probe, exhibiting a high temperature recovery factor that is insensitive to variations in Mach number, Reynolds number and installation arrangement. Secondly, attention is shifted to a dual-skin probe that is intended to acquire simultaneous

stagnation pressure and temperature measurements. This probe delivers high levels of pressure and temperature recovery performance, whilst also offering higher spatial measurement resolution compared to the *Baseline* combination probe.

7.2 Dual-skin PRT probe

The design of the dual-skin PRT probe has sought to minimise conductive heat transfer from the thin-film PRT sensor to the probe body. This has been achieved through the provision of an annular passage within the probe that is continuously purged with low velocity (near-stagnated) gas. This gas is fed from the sensing chamber and is consequently at a temperature close to the stagnation value. The conduction of heat away from the temperature sensor to the relatively cold probe outer body is therefore impeded (see section 6.4). This approach allows the probe to be constructed entirely from stainless-steel, which has suitable material properties (high temperature rating, robust) for use in an engine test environment. A schematic diagram of the dual-skin PRT probe is shown in Figure 7.1. A photograph featuring the dual-skin PRT probe at various stages during construction is shown in Figure 7.2.

The dual-skin probe is essentially comprised of two concentric stainless-steel cylinders that surround a thin-film PRT sensor. The outer cylinder forms the external body of the probe whilst the inner cylinder acts as the stagnation tube. The respective diameters of the inner and outer cylinders are approximately $2\,mm$ and $5\,mm$. The two cylinders are separated by an annular gap of $1.5\,mm$, which is sealed at the probe tip. The annular gap between the cylinders forms the passage within the probe that is purged with low velocity gas. This gas enters the passage through a set of vent holes in the inner cylinder and exits the passage

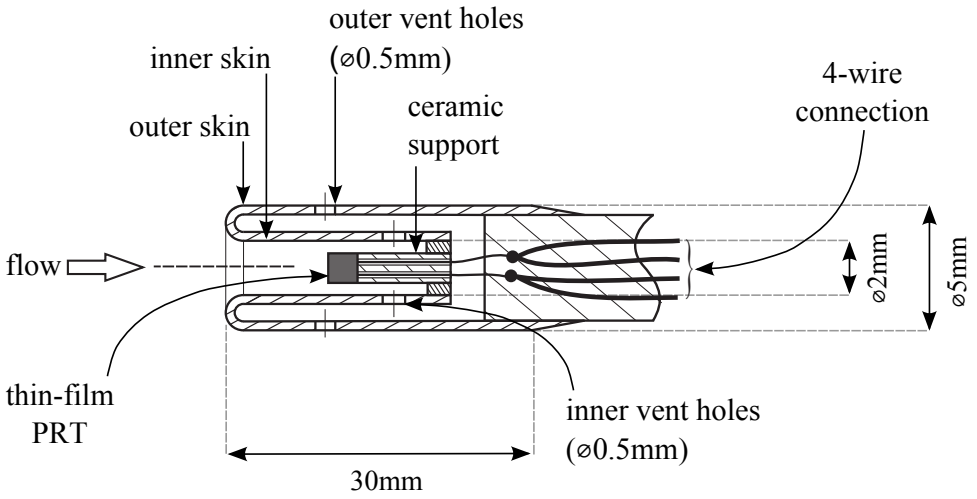

Figure 7.1: A schematic diagram of the dual-skin PRT probe.

through a further set of vent holes in the outer cylinder. The ratios of probe inlet area to cylinder vent area are approximately 1.3 and 2.6, these values being for the inner and outer cylinders respectively.

In the dual-skin design, the temperature sensor is mounted to the inner cylinder using a similar arrangement to that utilised in the *Baseline* PRT probe (see section 6.2.1). The thin-film PRT is bonded to a short ceramic (mullite) support, which contains two fine-bore holes that accommodate the sensor lead wires. At the rear of the ceramic support, the lead wires traverse the cavity between the two stainless-steel cylinders. The lead wires are then routed into the probe support, where a pair of extensions are attached to each leg to create a 4-wire connection.

The key aspect of the dual-skin design is the restriction of thermally conducting paths between the temperature sensor and the probe outer body. In comparison with the *Baseline* design, this approach will result in a significant reduction in conductive heat transfer away from the temperature sensor. The potential benefits of such a reduction have been demonstrated by the acrylic PRT probe, which exhibits a high temperature recovery factor ($R_{p,T} \approx 0.97$) that is insensitive to

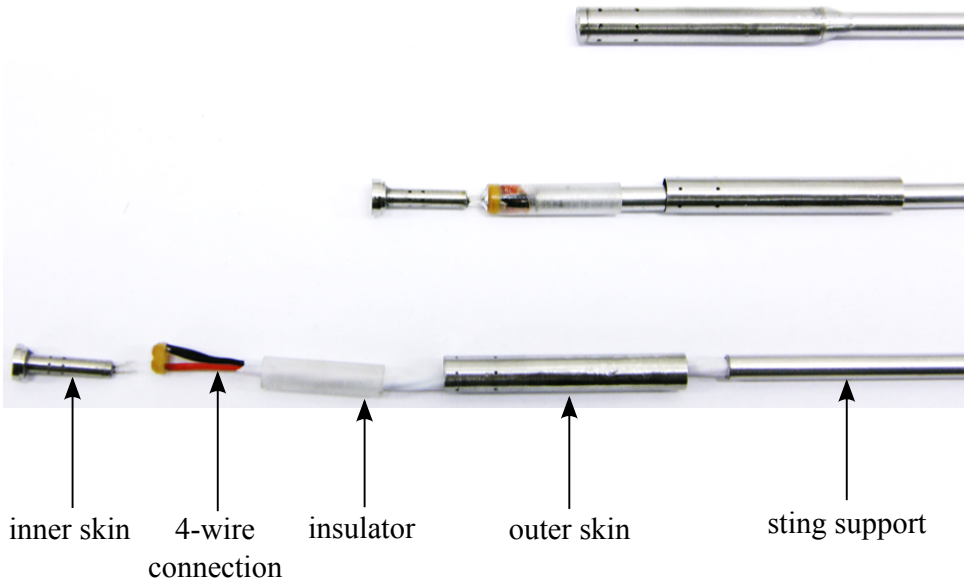

Figure 7.2: A photograph showing the dual-skin PRT probe at various stages during construction.

Mach and Reynolds number (see section 6.5). These probe performance characteristics are beneficial to stagnation temperature accuracy, since low levels of post-test measurement correction are required. The dual-skin design is expected to exhibit similar performance to the acrylic PRT probe, which will lead to an improvement in stagnation temperature accuracy compared to the *Baseline* design. This expectation has been verified through a series of trials in the Loughborough University probe aerodynamic calibration facility, which are reported in sections 7.2.1 to 7.2.3.

7.2.1 Incidence angle sensitivity

Figure 7.3 shows the temperature recovery factor of the dual-skin PRT probe as a function of both free-stream Mach number and flow incidence angle. This data has been gathered under atmospheric conditions ($T_{o,\infty} \approx 300\,K$ and $P_{\infty} \approx 1\,bar$), with the calibration facility operating in a free-jet configuration. The probe has

been tested in a sting-mounted arrangement, of the type shown in Figure 3.4.

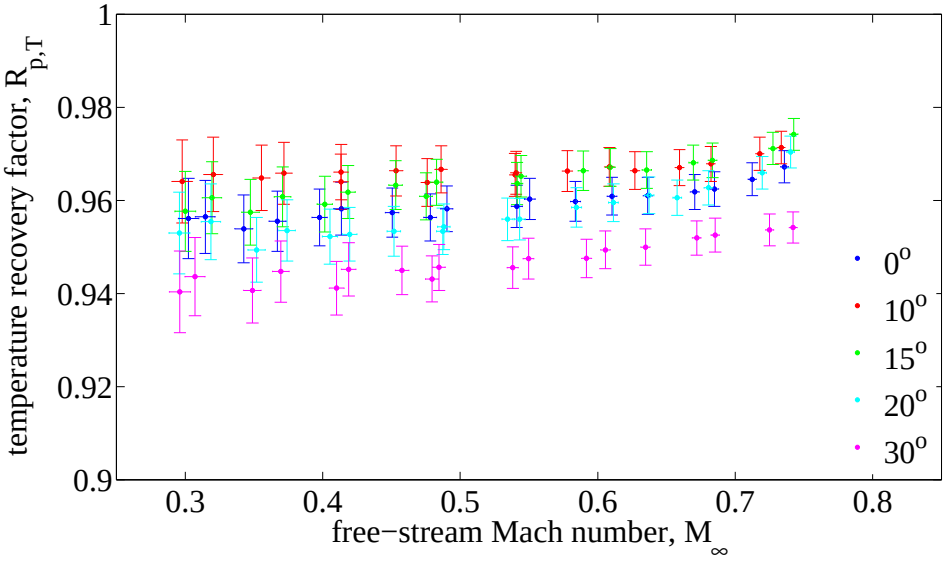

Figure 7.3: Temperature recovery factor of the dual-skin PRT probe as a function of flow incidence angle and free-stream Mach number (sting-mounted, ambient static pressure).

At zero flow incidence angle, the temperature recovery factor of the dual-skin probe varies between 0.95 and 0.97 over the Mach number range investigated. These values correspond to shortfalls in the measured stagnation temperature of $0.29\,K$ and $0.82\,K$ respectively. This performance is comparable to that reported for the acrylic PRT probe in section 6.5.1. For both probes, the high temperature recovery factors are attributed to a low level of conductive heat transfer from the PRT sensor. This leads to probe indicated temperatures that are close to the *true* stagnation temperature of the flow.

From Figure 7.3, it is apparent that the zero incidence performance of the dual-skin PRT probe is maintained up to a flow incidence angle of $20\,^o$ (within the bounds of measurement uncertainty). At angles beyond $20\,^o$, a reduction in the magnitude of the probe temperature recovery factor is observed. This reduction is associated with differences in the way gas enters the sensing chamber. At

high flow incidence angles, the gas is directed onto the side-wall of the sensing chamber rather than onto the leading edge of the thin-film PRT. This alters the rate of convective heat transfer between the gas and the sensor, as well as temperature recovery effects of the flow over the sensor (see sections 2.2.3.3 and 2.2.3). Since both of these phenomena are reported to influence the probe indicated temperature, they are regarded as being responsible for the reductions observed in probe temperature recovery factor.

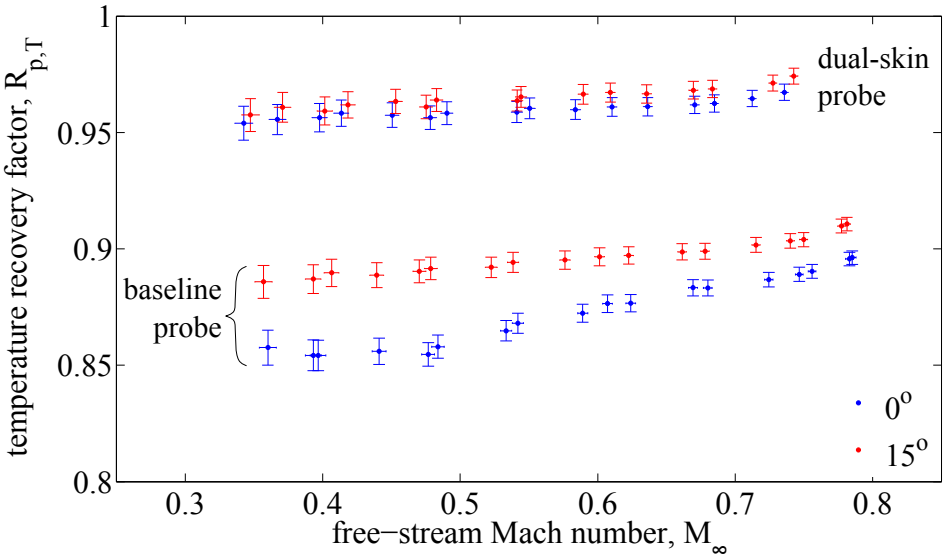

Figure 7.4: Temperature recovery factor of the dual-skin PRT probe compared to the Baseline PRT probe for flow incidence angles of 0^o and 15^o (sting-mounted, ambient static pressure).

Figure 7.4 shows temperature recovery factor data for the dual-skin PRT probe, plotted with equivalent data for the *Baseline* PRT probe. From this comparison, three important observations can be made. Firstly, the dual-skin PRT probe exhibits a temperature recovery factor that is much higher than that of the *Baseline* PRT probe. As a consequence, a low level of post-test measurement correction is required. This is beneficial to the accuracy of the corrected stagnation temperature, since the impact of uncertainties associated with the correction will be small. Secondly, the temperature recovery factor of the dual-skin PRT probe ex-

hibits less sensitivity to free-stream Mach number than the *Baseline* PRT probe. In fact, the performance of the dual-skin probe suggests that a single recovery factor ($R_{p,T}$) may used to correct measured temperature data. This implies that uncertainties in the value of $R_{p,T}$ will no longer arise from interpolation of the aerodynamic calibration curve. Thirdly, the temperature recovery factor of the dual-skin probe displays a much lower sensitivity to flow incidence angle than the *Baseline* PRT probe. The flow incidence angle must increase beyond 20^{o} before a change in temperature recovery factor is observed. As a consequence, it is improbable that uncertainties in the value of $R_{p,T}$ will arise from small misalignments of the probe with the flow direction. In summary, the uncertainty associated with corrected stagnation temperature measurements is likely to be significantly lower for the dual-skin PRT probe than for the *Baseline* PRT probe. To approach the target absolute stagnation temperature uncertainty of $\pm 0.1\,\%$, the adoption of the dual-skin design is therefore considered advantageous.

7.2.2 Reynolds number sensitivity

To allow the effects of Reynolds number to be investigated, the temperature recovery factor of the dual-skin PRT probe has been determined over a range of Mach numbers at different static pressure conditions. This data has been gathered with the calibration facility operating in an enclosed-jet configuration at atmospheric temperature conditions ($T_{o,\infty} \approx 300\,K$). Four different ratios of nozzle area to restrictor plate area (A_N/A_E) have been utilised, corresponding to values of 0.03 (ambient static pressure), 0.64, 0.74 and 0.81. In each instance, the probe has been tested in a sting-mounted arrangement at zero flow incidence angle.

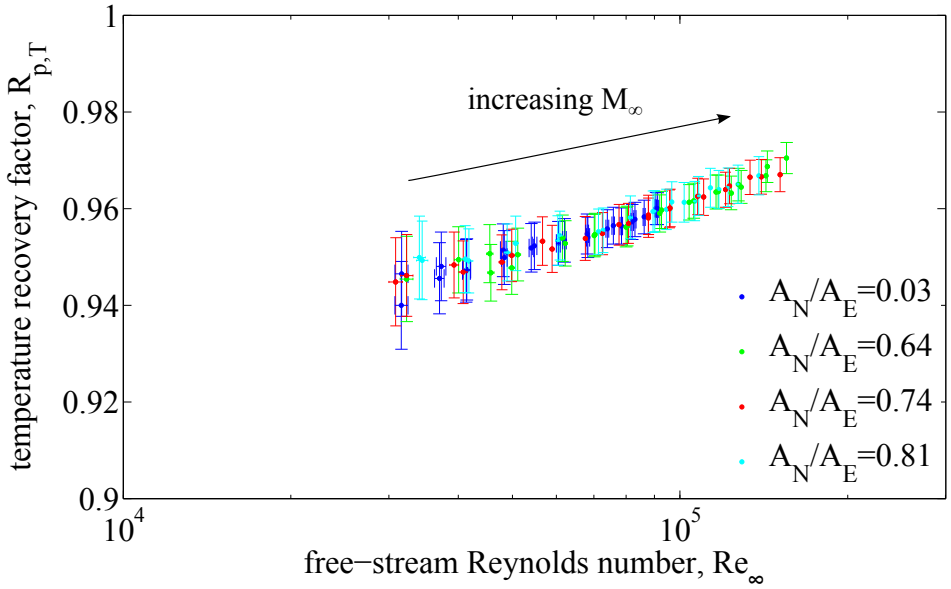

Figure 7.5: Temperature recovery factor of the dual-skin PRT probe as a function of free-stream Reynolds number (sting-mounted, zero flow incidence angle, various static pressure conditions).

Figure 7.5 shows the probe temperature recovery factor plotted as a function of free-stream Reynolds number for each value of A_N/A_E tested. From this data, it is clear that the dual-skin probe exhibits low sensitivity to Reynolds number, with the temperature recovery factor varying between values of 0.95 at $Re_\infty = 30,000$ and 0.97 at $Re_\infty = 150,000$. This result indicates that the performance of the probe is insensitive to the rate of convective heat transfer to the PRT sensor, which increases with free-stream Reynolds number.

At high Reynolds numbers, the convective heat transfer coefficient, h, at the surface of the PRT sensor is necessarily greater than at low Reynolds number conditions. Accordingly, there is an increase in the rate of heat transfer to sensor from the surrounding gas. In a conventional probe design, a high rate of convective heat transfer is beneficial to temperature recovery performance, since it counteracts the detrimental impact of conductive heat transfer to the probe body. This is demonstrated by the temperature recover factor of the *Baseline*

PRT probe, which increases with free-stream Reynolds number condition (see Figure 6.6). In the dual-skin design, the thermal isolation of the sensor from the probe body acts to limit the impact of conductive heat transfer to a low level. As a consequence, an increase in the rate of convective heat transfer to the sensor has little effect on probe temperature recovery performance. As free-stream Reynolds number increases, the temperature recovery factor of the dual-skin probe therefore remains approximately constant. In contrast to the *Baseline* device, this suggests that the temperature recovery performance of the dual-skin PRT probe is not governed by the balance between convective and conductive heat transfer mechanisms. Rather, it is determined by temperature recovery effects of the flow over the sensor.

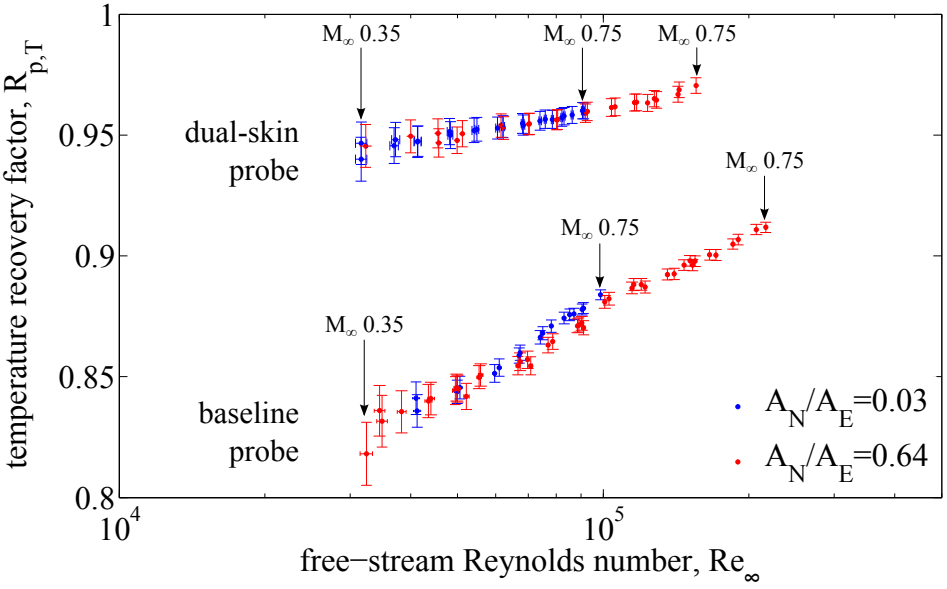

Figure 7.6: Temperature recovery factor of the dual-skin PRT probe compared to the Baseline PRT probe at ambient ($A_N/A_E = 0.03$) and elevated ($A_N/A_E = 0.64$) static pressure conditions (sting-mounted, zero flow incidence angle).

The different Reynolds number sensitivities exhibited by the dual-skin and *Baseline* PRT probes are illustrated in Figure 7.6, which shows temperature recovery factors at ambient ($A_N/A_E = 0.03$) and elevated ($A_N/A_E = 0.64$) static pressure

conditions. For the *Baseline* PRT probe, there is a significant improvement in temperature recovery factor at higher Reynolds numbers, for a fixed free-stream Mach number condition. At Mach 0.75, an increase in $R_{p,T}$ from 0.88 to 0.91 is observed over a Reynolds number range of $100\,000 - 200\,000$. This implies that post-test measurement corrections must be applied as a function of free-stream Reynolds number rather than as a function of free-stream Mach number. This has important implications for the probe aerodynamic calibration procedure, which must consequently be performed over a range of Reynolds numbers that are representative of gas turbine engine operating conditions. The dual-skin PRT probe avoids this requirement by exhibiting a temperature recovery factor that is approximately invariant with both free-stream Mach and Reynolds number. At Mach 0.75, an increase in $R_{p,T}$ of less than 0.01 is observed over a Reynolds number range of $90\,000 - 160\,000$. This implies that post-test measurement corrections may be applied using a single value of $R_{p,T}$. As a consequence, the range of the probe aerodynamic calibration procedure may be restricted, resulting in considerable reductions in complexity, cost and time in comparison with the *Baseline* case.

7.2.3 Probe installation sensitivity

The results presented in sections 7.2.1 and 7.2.2 have been acquired with the dual-skin PRT probe in a sting-mounted configuration. This simulates the aero-thermal boundary conditions experienced by surface-bonded probes, which are commonly found on the fan outlet guide vane and engine section stator (see section 2.1.3). Elsewhere in the engine, probes are either mounted onto rakes that are attached to the engine casing, or installed directly onto the leading edge of turbine nozzle guide vanes (see section 2.1.3). In comparison to surface-bonded

probes, these probes are clearly subject to different aero-thermal boundary conditions. To investigate the impact of these conditions on probe temperature recovery factor, the performance of the dual-skin PRT probe has been assessed using the rake arrangement described in section 3.2.4. This investigation has also considered the impact of probe protrusion length, L, which is defined as the distance between the leading edge of the probe and the leading edge of the rake (see Figure 3.4).

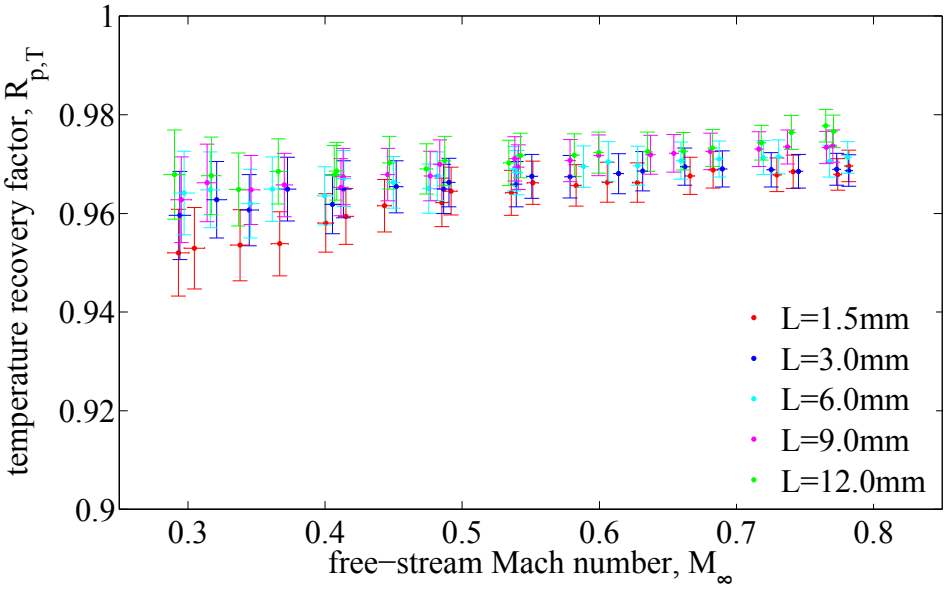

Figure 7.7: Temperature recovery factor of the dual-skin PRT probe as a function of protrusion from the rake body and free-stream Mach number (rake-mounted, zero flow incidence angle, ambient static pressure).

Figure 7.7 shows temperature recovery factors for the dual-skin PRT probe in a rake-mounted configuration at different probe protrusion lengths. This data has been gathered under atmospheric conditions ($T_{o,\infty} \approx 300\,K$ and $P_{\infty} \approx 1\,bar$), with the calibration facility operating in a free-jet configuration. From Figure 7.7, two important observations can be made. Firstly, the temperature recovery performance of the dual-skin PRT probe exhibits low sensitivity to probe protrusion length. At Mach 0.75, the value of $R_{p,T}$ varies between 0.96 at $L = 1.5\,mm$

and 0.97 at $L = 12\,mm$. Secondly, the temperature recovery performance of the rake-mounted probe is comparable to that of the sting-mounted probe, which is shown in Figure 7.3. In both configurations, there is an increase in the value of $R_{p,T}$ from 0.95 to 0.97 over the Mach number range investigated. This suggests that the temperature recovery performance of the dual-skin PRT probe can be considered independent of installation arrangement.

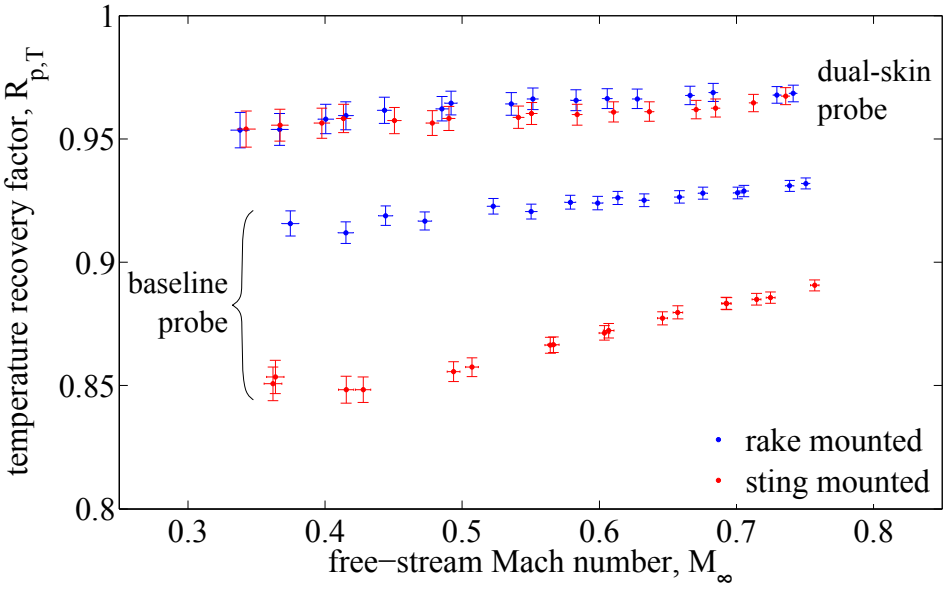

Figure 7.8: Temperature recovery factor of the dual-skin PRT probe compared to the Baseline PRT probe for both sting and rake-mounted configurations (zero flow incidence angle, ambient static pressure)

The different installation sensitivities exhibited by the dual-skin and *Baseline* PRT probes are illustrated in Figure 7.8, which shows data acquired in both sting and rake-mounted ($L = 3\,mm$) configurations. The data essentially indicate the relative significance of thermal conduction to the temperature recovery performance of the two probe designs. For the *Baseline* PRT probe, the additional thermal resistance provided by the rake mount impedes conductive heat transfer from the sensor to the probe body. Since the performance of the probe is driven by the balance between convective and conductive heat transfer mech-

anisms, this leads to an increase in probe temperature recovery factor between the sting and rake-mounted configurations. In order to facilitate the application of post-test measurement corrections, separate aerodynamic calibrations must therefore be performed for different probe mounting arrangements. For the dual-skin PRT probe, the additional thermal resistance provided by the rake mount has little effect on probe temperature recovery performance. This is because the thermal isolation of the sensor from the probe body limits the impact of conductive heat transfer to a low level. The probe temperature recovery factor therefore remains unchanged between the sting and rake-mounted configurations. This implies that post-test measurement corrections applied to different probe mounting arrangements may be based on the same aerodynamic calibration data. As a consequence, calibrations may be restricted to a single probe specimen, leading to significant cost and time savings in comparison with *Baseline* case.

7.3 Combination dual-skin PRT probe

Like the *Baseline* PRT probe, the dual-skin PRT probe can be readily converted into a combined stagnation pressure and temperature measuring device (see section 6.2.2). This conversion simply requires the addition of a Pitot tube to the annular passage that is formed between the sensing chamber and the outer probe body. Since the annular passage is continuously purged with low velocity gas from the sensing chamber, the Pitot tube can register a pressure that is close to the free-stream stagnation pressure. A schematic diagram of the combination dual-skin PRT probe is shown in Figure 7.9. The dimensions of this probe are identical to those of the temperature-only dual-skin PRT probe, which are defined in section 7.2. The diameter of the Pitot tube is approximately $1\,mm$.

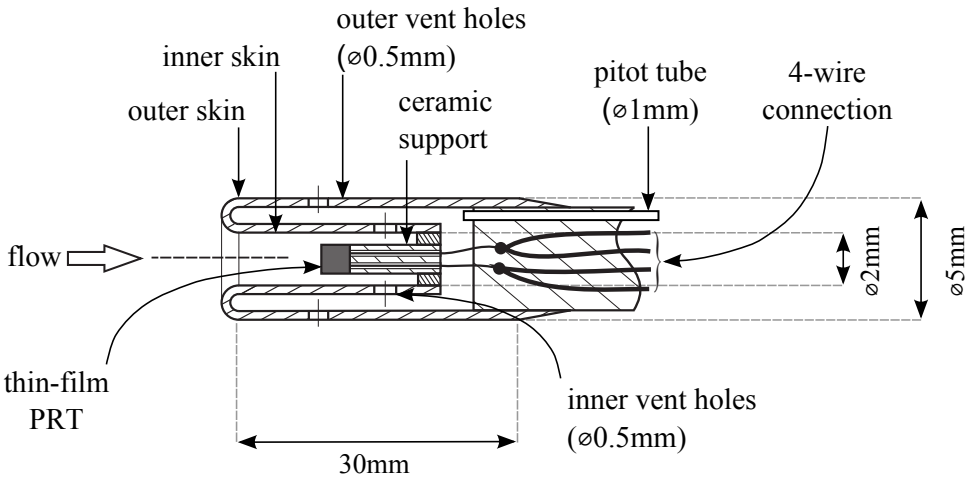

Figure 7.9: A schematic diagram of the combination dual-skin PRT probe.

In contrast to the *Baseline* PRT probe, the dual-skin PRT probe is capable of accommodating a Pitot tube without an increase in overall probe diameter (see section 6.2.2). As a consequence, the dual-skin probe can provide stagnation pressure and temperature measurements at comparatively higher spatial resolution. This is an important advantage in an engine test environment, since it facilitates a more detailed survey of the stagnation pressure and temperature variations across the annulus. Ultimately, details of these variations can be incorporated into engine performance calculations to yield more accurate estimates of turbomachinery efficiency.

7.3.1 Probe stagnation pressure loss

As gas travels through the combination dual-skin PRT probe, viscous effects cause a loss of stagnation pressure. This loss occurs as a consequence of friction between the gas and the solid surfaces of the probe, as well as due to separation as gas passes through the inner and outer vent hole arrays. Since the internal surfaces of the probe have low wetted area, the pressure loss due to frictional

effects will be small. Accordingly, the dominant pressure loss will be associated with flow through the two vent hole arrays. In order to estimate the magnitude of this loss, it is useful to simplify the complex probe geometry using the 1-D network model shown in Figure 7.10. In this model, the probe is approximated by a smooth pipeline of variable cross sectional area. The sensing chamber (1) is represented by an initial intake length of equal sectional area. The inner (2) and outer (3) vent holes are represented by two in-line contractions, which have sectional areas equal to the total area of each vent hole array. It is assumed that the Pitot tube is located in region between the two contractions, which is representative of the annular passage.

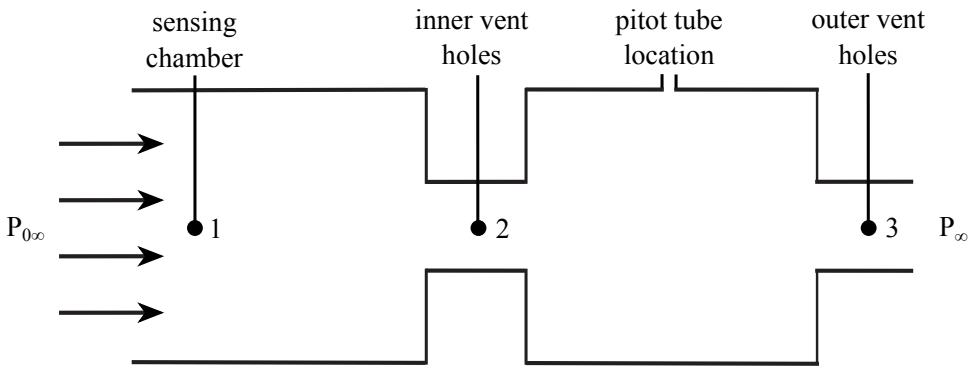

Figure 7.10: 1-D network model of the combination dual-skin PRT probe.

Assuming stagnation conditions at the inlet and static conditions at the outlet, the overall stagnation pressure loss across the pipeline, ΔP_{tot}, can be expressed as the difference between the free-steam stagnation and static pressure (equation 7.1).

$$\Delta P_{tot} = P_{0,\infty} - P_{\infty} \tag{7.1}$$

This overall loss is comprised of the elemental stagnation pressure losses that occur as gas passes through the two pipeline contractions. As a first order ap-

proximation, the stagnation pressure loss across each contraction, ΔP, can be equated to the local dynamic pressure, q (equation 7.2). This assumes that the gas is able to expand freely upon exiting the contraction, and that the flow within the pipeline is incompressible. The incompressible assumption is valid since flow velocities inside the probe must be $\leq$ Mach 0.25 in order to provide an accurate indication of stagnation quantities (see section 2.1.2).

$$\Delta P = q = \frac{1}{2}\rho V^2 \tag{7.2}$$

The overall stagnation pressure loss across the pipeline can therefore be related to the sum total of the local dynamic pressure in each contraction (equation 7.3).

$$\Delta P_{tot} = P_{0,\infty} - P_{\infty} = \frac{1}{2}\rho {V_2}^2 + \frac{1}{2}\rho {V_3}^2 \tag{7.3}$$

Using the continuity equation, an expression may be derived to relate the local flow conditions at each point in the pipeline (equation 7.4). Constant density can be assumed in this expression, since the flow inside the pipeline is incompressible

.

$$\dot{m} = \rho A_1 V_1 = \rho A_2 V_2 = \rho A_3 V_3 \tag{7.4}$$

As a consequence of separation, the effective flow area through each contraction is reduced relative to the geometric area. To account for this reduction, the sectional area of the contraction must be multiplied by a discharge coefficient, C_D. After including this coefficient, equation 7.4 transforms to equation 7.5.

$$\dot{m} = \rho A_1 V_1 = \rho C_{D_2} A_2 V_2 = \rho C_{D_3} A_3 V_3 \tag{7.5}$$

Rearrangements of equation 7.5 can be substituted into equation 7.3 to yield an alternative expression (equation 7.6) for the overall stagnation pressure loss across the pipeline. This expression is a unique function of the inlet velocity, V_1, and the sectional area ratio between the inlet and the two contractions, A_1/A_2 and A_1/A_3. The two terms in this expression relate to the stagnation pressure loss across first and last contractions, respectively.

$$\Delta P_{tot} = \frac{1}{2}\rho \left(V_1 \frac{A_1}{C_{D_2} A_2} \right)^2 + \frac{1}{2}\rho \left(V_1 \frac{A_1}{C_{D_3} A_3} \right)^2 \tag{7.6}$$

Since the Pitot tube is located in the region between the two contractions, it is minimum pressure loss across the first contraction that is necessary in order to acquire an accurate stagnation pressure measurement. In terms of the geometry of the combination dual-skin PRT probe, this corresponds to minimum pressure loss across the inner vent hole array. According to equation 7.6, this requires two important criteria to be satisfied. Firstly, the total area of the inner vent hole array, A_2, must be large relative to the sectional area of the sensing chamber, A_1. This criterion can be readily satisfied through the specification of a large vent hole diameter, d_2. Secondly, the gas velocity within the sensing chamber, V_1, must be low. Satisfaction of this criterion relies on knowledge of the factors that influence flow conditions inside the probe.

In the work of Saravanamuttoo (1990), equation 7.7 is used to relate the sensing chamber velocity to the free-stream Mach number, M_∞, and the sectional area ratio between the sensing chamber and vent hole array, A_1/A_{vent}. In the

derivation of this equation, free-stream static conditions are assumed at the vent holes and stagnation stream conditions are assumed within the sensing chamber. The relationship between these two conditions is expressed using the formula for isentropic density ratio (Anderson, 1990).

$$M_1 = \frac{V_1}{a_1} = M_\infty \left(\frac{A_{vent}}{A_1} \right) [1 + \frac{\gamma - 1}{2} {M_\infty}^2]^{\frac{-1}{\gamma - 1}} \tag{7.7}$$

Equation 7.7 is valid for a conventional Kiel probe, of the type described in sections 2.1.2 and 6.2.1. However, for a dual-skin probe the area of both the inner and outer vent hole arrays may impact the sensing chamber velocity. In the case of the combination dual-skin PRT probe, the flow area through the inner vent hole array, A_2, must be large in order to minimise stagnation pressure loss (see equation 7.6). As a consequence, the inner vent holes will have a second order effect on flow conditions inside the probe. The comparatively smaller area of the outer vent hole array will have the controlling influence on sensing chamber velocity. For the combination dual-skin PRT probe, equation 7.7 must therefore be modified to include the area of the outer vent hole array, A_3 (equation 7.8).

$$M_1 = \frac{V_1}{a_1} = M_\infty \left(\frac{A_3}{A_1} \right) [1 + \frac{\gamma - 1}{2} {M_\infty}^2]^{\frac{-1}{\gamma - 1}} \tag{7.8}$$

According to equation 7.8, at a fixed free-stream Mach number the gas velocity within the sensing chamber is governed by the sectional area ratio between the outer vent hole array and the sensing chamber. For a low gas velocity, the area of the outer vent hole array, A_3, must be small relative to the sectional area of the sensing chamber, A_1. This can be achieved through the specification of a small vent hole diameter, d_3.

7.3.2 Design optimisation study

In order for the combination dual-skin PRT probe to provide an accurate indication of stagnation pressure, the area ratios between the sensing chamber and two vent hole arrays must be carefully selected. Investigations conducted to identify optimum values for these area ratios are described in sections 7.3.2.1 and 7.3.2.2. In each investigation, the area ratio corresponding to one vent hole array has been varied, while the area ratio corresponding to the other vent hole array has been fixed. The optimum values identified are therefore only valid for the particular area ratio combinations tested.

7.3.2.1 Inner vent hole array

To minimise stagnation pressure loss across the inner vent hole array, the total inner vent hole area, A_2, must be large relative to the sectional area of the sensing chamber, A_1 (see equation 7.6). To identify the optimum area ratio, A_2/A_1, the Loughborough University probe aerodynamic calibration facility has been used to assess the performance of probes with inner vent hole arrays of different total area. Table 7.1 summarises the differences between each of the probes that have been investigated, including the vent hole shape, dimension and quantity. For each probe, the area ratio between the outer vent hole array and the sensing chamber, A_3/A_1, is fixed at 0.38.

Figures 7.11 and 7.12 show the pressure and temperature recovery factors that have been determined for each combination dual-skin PRT probe at selected free-stream Mach number conditions. This data has been gathered under atmospheric conditions ($T_{o,\infty} \approx 300\,K$ and $P_\infty \approx 1\,bar$), with the calibration facility operating

Shape	Dimensions (mm)	Number	A_2/A_1
Circular hole	Ø0.5	12	0.77
Circular hole	Ø0.7	12	1.50
Rectangular slot	0.7×1.67	6	2.28
Rectangular slot	0.7×2.75	6	3.75
Rectangular slot	0.7×3.75	6	5.12
Rectangular slot	0.7×4.5	6	6.14
Rectangular slot	0.7×5	6	6.82

Table 7.1: Details of the different inner vent hole geometries that have been trialled in combination dual-skin PRT probes.

in a free-jet configuration. In each instance, the probe has been tested in a sting-mounted arrangement at zero flow incidence angle.

From the data plotted in Figure 7.11, an improvement in the pressure recovery performance of the combination dual-skin PRT probe can be observed as the value of A_2/A_1 is increased. At low area ratios, the pressure recovery factor is limited by stagnation pressure losses incurred as gas passes through the inner vent holes. At higher area ratios, these losses are diminished and hence the pressure recovery factor is increased. This trend persists up to $A_2/A_1 = 5.12$, beyond which the pressure recovery factor converges to a maximum value of approximately 0.97. At a free-stream Mach number of 0.7, this corresponds to a stagnation pressure measurement shortfall of $11\,mbar$. This shortfall is sufficiently small that a low level of post-test measurement correction is required. In order for the probe to provide an accurate indication of stagnation pressure, the optimum sectional area ratio between the inner vent hole array and sensing chamber is therefore ≥ 5.12 (for $A_3/A_1 = 0.38$).

Practically, there is a limit to the maximum value of A_2/A_1 that can be realised in a probe design. Concerns over mechanical integrity restrict the amount of

material that can be removed from the probe in order to enlarge the inner vent hole area, A_2. However, the benefit of increasing A_2 is diminished once a high value of A_2/A_1 has been achieved. This is because the majority of the stagnation pressure drop across the probe has already been transferred to the outer vent hole array. This trend is evident in Figure 7.11, where little improvement in probe pressure recovery factor can be observed beyond $A_2/A_1 = 5.12$. At this area ratio, less than 1% of the overall pressure loss occurs across the inner vent hole array (for $A_3/A_1 = 0.38$).

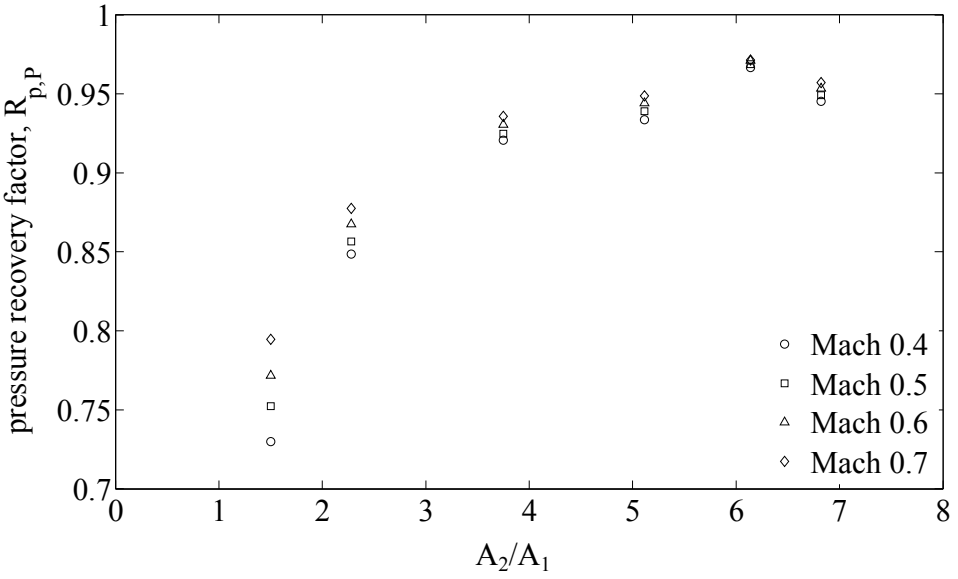

Figure 7.11: Pressure recovery factor of several combination dual-skin PRT probes with different inner vent hole areas (sting-mounted, zero flow incidence, ambient static pressure). $A_3/A_1 = 0.38$.

Based on the data plotted in Figure 7.12, the temperature recovery performance of the combination dual-skin PRT probe demonstrates low sensitivity to the value of A_2/A_1. At a free-stream Mach number of 0.7, the temperature recovery factor varies by approximately 0.02 over the range of area ratios investigated. Accordingly, the sectional area ratio between the inner vent hole array and sensing chamber can be selected to optimise pressure recovery performance, without compromising temperature recovery performance.

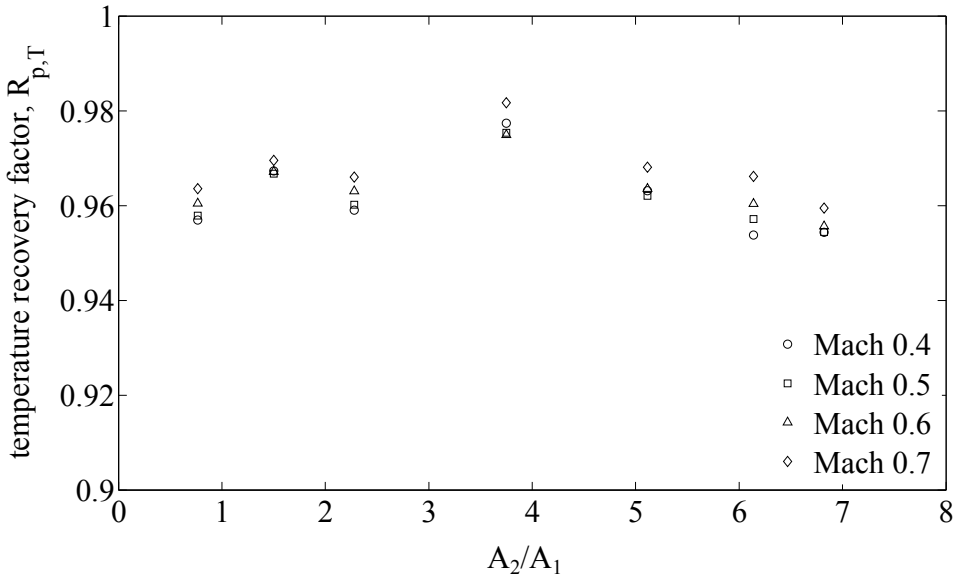

Figure 7.12: Temperature recovery factor of several combination dual-skin PRT probes with different inner vent hole areas (sting-mounted, zero flow incidence, ambient static pressure). $A_3/A_1 = 0.38$.

Section 2.2.3 describes the relationship between probe temperature recovery factor and temperature recovery effects of the flow over the sensor. This relationship is governed by the gas velocity within the sensing chamber, V_1. The consistent recovery factors plotted in Figure 7.12 suggest that the value of A_2/A_1 has no impact on temperature recovery effects of the flow over the sensor. Accordingly, the sectional area ratio between the inner vent hole array and sensing chamber has no influence on the sensing chamber velocity. This result supports the hypothesis (see section 7.3.1) that the gas velocity within the sensing chamber is controlled by the sectional area ratio between the outer vent hole array and sensing chamber, A_3/A_1. Section 7.3.2.2 describes the impact of this parameter on the pressure and temperature recovery performance of the combination dual-skin PRT probe.

7.3.2.2 Outer vent hole array

In the sensing chamber, a low gas velocity is necessary in order to minimise the stagnation pressure loss across the inner vent hole array (see equation 7.6). According to equation 7.8, this requires the total area of the outer vent hole array, A_3, to be small relative to the sectional area of the sensing chamber, A_1. To determine the optimum area ratio, A_3/A_1, the Loughborough University probe aerodynamic calibration facility has been used to evaluate the performance of probes with outer vent hole arrays of different total area. The probes investigated each feature an outer array of six circular vent holes, with hole diameters that vary between $0.35\,mm$ and $1.0\,mm$. These details are summarised in Table 7.2. Each of the probes feature an identical inner vent hole array, which is comprised of six $0.7 \times 5\,mm$ slots ($A_2/A_1 = 6.82$). This corresponds to the best performing geometry reported in section 7.3.2.1 (for $A_3/A_1 = 0.38$).

Diameter (mm)	Number	A_3/A_1
0.35	6	0.19
0.4	6	0.24
0.5	6	0.38
0.6	6	0.65
0.7	6	0.75
0.8	6	0.98
1.0	6	1.53

Table 7.2: Details of the different outer vent hole geometries that have been trialled in combination dual-skin PRT probes.

Figures 7.13 and 7.14 show pressure and temperature recovery factors for each of the combination dual-skin PRT probes at selected free-stream Mach number conditions. This data has been obtained under atmospheric conditions ($T_{o,\infty} \approx 300\,K$ and $P_\infty \approx 1\,bar$), with the calibration facility operating in a free-jet con-

figuration. The probes have each been tested in a sting-mounted arrangement, at zero flow incidence angle.

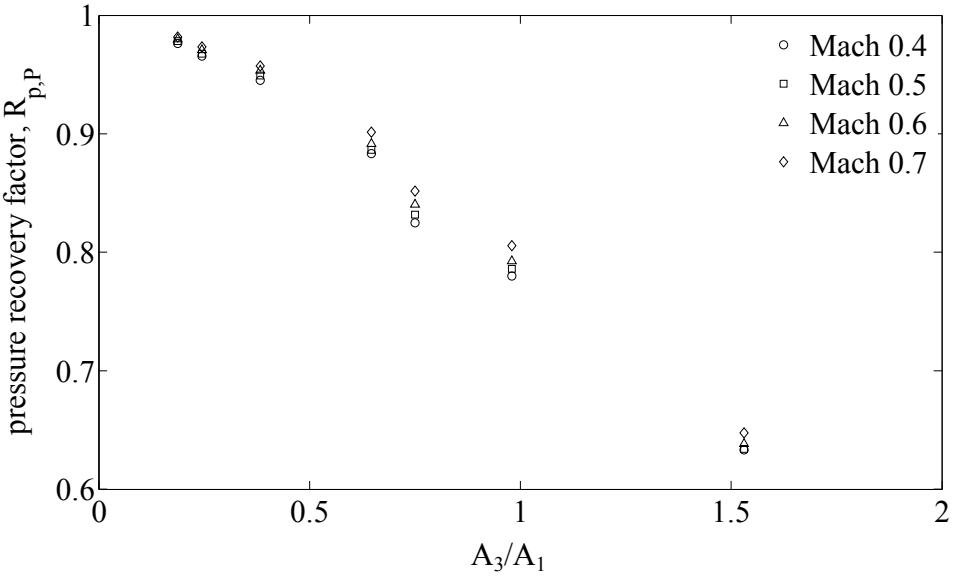

Figure 7.13: Pressure recovery factor of several combination dual-skin PRT probes with different outer vent hole areas (sting-mounted, zero flow incidence, ambient static pressure). $A_2/A_1 = 6.82$

From Figure 7.13, it can be observed that the pressure recovery performance of the combination dual-skin PRT probe worsens as the value of A_3/A_1 is increased. At a free-stream Mach number of 0.7, the probe pressure recovery factor reduces from 0.96 at an area ratio of 0.38 to 0.65 at an area ratio of 1.53. This trend is caused by increases in the gas velocity within the sensing chamber, which result in greater stagnation pressure loss across the inner vent holes (see equation 7.6). Below an area ratio of 0.38, the probe pressure recovery factor converges to a maximum value of approximately 0.98. At a free-stream Mach number of 0.7, this corresponds to a relatively small stagnation pressure measurement shortfall of $7\,mbar$. In order for the probe to deliver an accurate indication of stagnation pressure, the optimum sectional area ratio between the outer vent hole array and the sensing chamber is therefore ≤ 0.38 (for $A_2/A_1 = 6.82$).

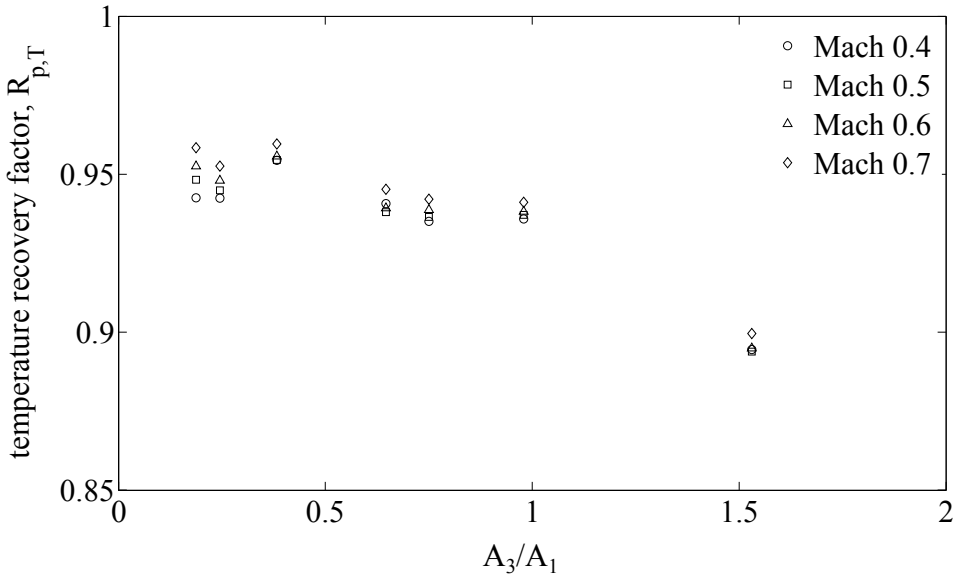

Figure 7.14: Temperature recovery factor of several combination dual-skin PRT probes with different outer vent hole areas (sting-mounted, zero flow incidence, ambient static pressure). $A_2/A_1 = 6.82$.

By examining the results presented in Figure 7.14, it is clear that the temperature recovery performance of the combination dual-skin PRT probe deteriorates as the value of A_3/A_1 is increased. At an area ratio 1.53, the probe temperature recovery factor is limited to 0.89 due to a high gas velocity within the sensing chamber. This gas velocity governs temperature recovery effects of the flow over the sensor, which have a direct impact on probe temperature recovery performance (see section 2.2.3). At an area ratio 0.38, the sensing chamber velocity is significantly reduced and a higher temperature recovery factor of 0.96 is attained. This is consistent with the performance of the temperature-only dual-skin PRT probe, which is described in section 7.2. In order to obtain an accurate indication of stagnation temperature, the optimum sectional area ratio between the outer vent hole array and the sensing chamber is therefore ≤ 0.38 (for $A_2/A_1 = 6.82$). This corresponds to the same area ratio that is necessary to achieve high pressure recovery performance.

Practically, there is a limit to the minimum value of A_3/A_1 that can be utilised in a probe design. In order to maintain convective heat transfer between the gas and the PRT sensor (see section 2.2.3.3), some continuous flow through the probe is required. According to equation 7.8, this necessitates the outer vent hole area, A_3, to be > 0. Additionally, the diameter of the outer vent holes, d_3, must be sufficiently large to prevent blockage of the probe by air-borne particulate. This places a further restriction on the smallest outer vent hole area, A_3, that can be realised. In regard to probe pressure recovery performance, the benefit of reducing A_3 is diminished once a low value of A_3/A_1 has been attained. This is because the majority of the overall stagnation pressure drop already occurs across the outer vent hole array. This trend is evident in Figure 7.13, where little improvement in probe pressure recovery factor can be observed beyond $A_3/A_1 = 0.38$. At this area ratio, more than 99% of the overall pressure loss occurs across the outer vent hole array (for $A_2/A_1 = 6.82$).

7.3.3 Pressure and temperature recovery performance

Based on the findings presented in section 7.3.2, a combination dual-skin PRT probe has been produced that is optimised for pressure and temperature recovery performance. The probe features an inner vent hole array that is comprised of six $0.7 \times 5\,mm$ slots ($A_2/A_1 = 6.82$) and an outer vent hole array that consists of six $0.5\,mm$ diameter holes ($A_3/A_1 = 0.38$). These values are within the optimum ranges identified in sections 7.3.2.1 and 7.3.2.2. Concerns over mechanical robustness have prevented the use of higher values of A_2/A_1, which would require further removal of material from the internal surfaces of the probe. Similarly, potential blockages due to air-borne particulate have discouraged the use of lower values of A_3/A_1, which would necessitate a reduction in outer vent hole diameter

to $< 0.5\,mm$.

In order to investigate the pressure and temperature recovery performance of the optimised combination dual-skin PRT probe, a series of sensitivity studies have been conducted using the Loughborough University probe aerodynamic calibration facility. Figures 7.15 and 7.16 show the results of a Mach number sensitivity study, which has been performed under atmospheric conditions ($T_{o,\infty} \approx 300\,K$ and $P_{\infty} \approx 1\,bar$) with the calibration facility operating in a free-jet configuration. The probe has been tested in a sting-mounted arrangement, at zero flow incidence angle. Appendix B contains the results of three further sensitivity studies, which consider the influence of flow incidence angle, free-stream Reynolds number and probe installation arrangement.

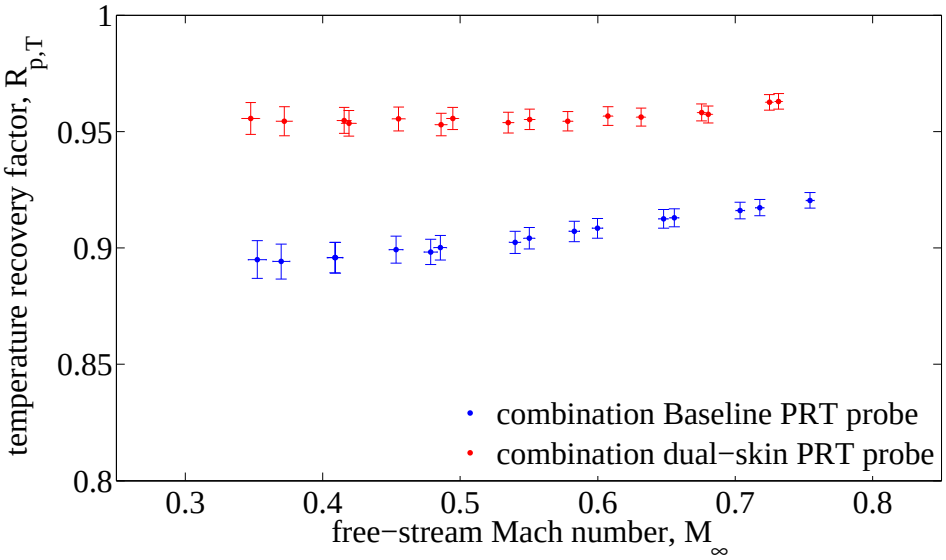

Figure 7.15: Temperature recovery of the optimised combination dual-skin PRT probe compared to the combination Baseline PRT probe (sting-mounted, zero flow incidence angle, ambient static pressure).

Figure 7.15 shows the temperature recovery factor of the optimised combination dual-skin PRT probe, plotted alongside the temperature recovery factor of the combination *Baseline* PRT probe (see section 6.2.2). Over the free-stream Mach

number range investigated, the temperature recovery factor of the combination dual-skin probe varies between 0.95 and 0.97. These values correspond to stagnation temperature measurement shortfalls of $0.25\,K$ and $0.80\,K$ respectively. These shortfalls are comparable to those reported for the temperature-only dual-skin PRT probe in section 7.2.1. The dual-skin PRT probe can therefore be successfully adapted to provide simultaneous pressure and temperature measurements, without compromising temperature recovery performance.

In comparison to the optimised combination dual-skin PRT probe, the combination *Baseline* PRT probe exhibits inferior temperature recovery performance. The probe temperature recovery factor varies between 0.90 and 0.92 over the free-stream Mach number range considered. These values correspond to shortfalls in the measured stagnation temperature of $0.56\,K$ and $2.26\,K$ respectively. This result is attributed to the increased sensitivity of the *Baseline* probe design to thermal conduction (see section 6.4). This causes heat to be transferred away from the PRT sensor, leading to a reduction in the probe indicated temperature. In comparison to the combination dual-skin PRT probe, a larger post-test measurement correction is therefore required. This is detrimental to the accuracy of the corrected stagnation temperature, since the uncertainties associated with the correction will be increased. To achieve the highest stagnation temperature measurement accuracy, adoption of the combination dual-skin PRT probe is consequently recommended.

Figure 7.16 shows the pressure recovery performance of both the optimised combination dual-skin PRT probe and the combination *Baseline* PRT probe (see section 6.2.2). At a free-stream Mach number of 0.75, a pressure recovery factor of 0.95 is recorded for the dual-skin probe, whereas a pressure recovery factor of 0.99 is recorded for the *Baseline* probe. These values correspond to shortfalls

in the measured stagnation pressure of 18 $mbar$ and 4 $mbar$ respectively. For the dual-skin probe, the comparatively larger shortfall is attributed to the loss of stagnation pressure as gas travels through complex passages inside the probe head. These losses are diminished in the *Baseline* probe as the gas is required to traverse a much simpler route (see Figure 6.3). Since lower uncertainties are associated with the correction of smaller measurement shortfalls, higher accuracy can be achieved with the combination *Baseline* PRT probe compared to the combination dual-skin PRT probe. In order to benefit from the enhanced temperature recovery performance offered by the dual-skin device, some stagnation pressure measurement accuracy must consequently be sacrificed.

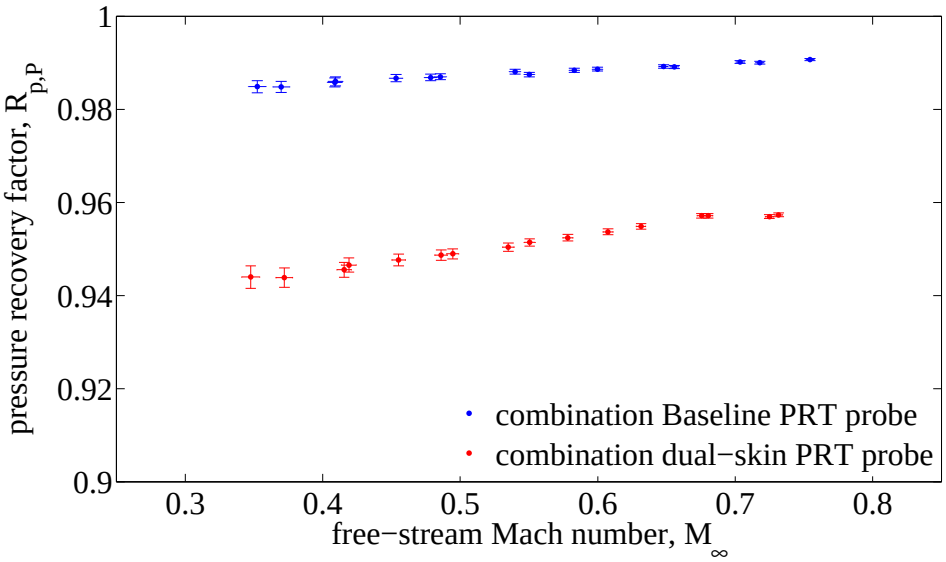

Figure 7.16: Pressure recovery of the optimised combination dual-skin PRT probe compared to the combination Baseline PRT probe (sting-mounted, zero flow incidence angle, ambient static pressure). $A_2/A_1 = 6.82$.

CHAPTER 8

Conclusions

8.1 Overall summary

This thesis has captured work undertaken towards the development of a more accurate stagnation temperature probe for use in gas turbine engines. This work has involved the creation of a facility at Loughborough University for aerodynamic probe calibration. The performance of this facility has been assessed, and the uncertainty in the calibration data has been established. The facility has subsequently been used to investigate the topics of temperature sensor performance and probe temperature recovery performance, both of which have an important influence on stagnation temperature measurement accuracy. The findings of these two investigations have informed the design of a new dual-skin PRT probe, which is intended to achieve an absolute stagnation temperature measurement uncertainty close to $\pm 0.1\,\%$. Finally, the performance of the new probe design has been studied in different installation arrangements, over a range of engine representative free-stream Mach and Reynolds numbers.

8.2 Individual chapter summaries

The work presented in this thesis has been divided into 6 main chapters. Sections 8.2.1 to 8.2.6 provide brief summaries of the work reported in each chapter.

8.2.1 Stagnation temperature measurement

In gas turbine engines, measurements of the gas-path temperature are required in order to assess the efficiency of individual components of turbomachinery. These measurements are acquired using fixed intrusive probes, which are typically comprised of a thermocouple sensor surrounded by a ventilated stagnation tube. Probes are installed at various axial locations in the gas-path that correspond to the inlet/outlet of the main components of turbomachinery. At each location, probes are either bonded to the surface of aerofoils, mounted onto rakes that are attached to the engine casing, or installed directly onto the leading edge of nozzle guide vanes. Across the measurement locations, there are significant variations in local flow conditions. For example, pressures and temperatures increase from ambient conditions at fan inlet, to values in excess of $55\,bar$ and $1020\,K$ at core compressor outlet. Similarly, Mach numbers differ from values > 1 at fan outlet, to approximately 0.3 in the combustor.

Accurate gas-path stagnation temperature measurements are vital in order to establish whether individual turbomachinery components are operating as intended, or whether design requirements are required. To enable the assessment of turbomachinery efficiency to an uncertainty of $\pm 0.5\%$, an absolute stagnation temperature measurement uncertainty of $\pm 0.1\%$ must be achieved. Presently, the realisable uncertainty in stagnation temperature measurements is limited to

approximately ±0.5%. This is related to problems that affect the measurement performance of the temperature sensor and the temperature recovery performance of the probe assembly. Two distinct strategies can be employed in order to improve the accuracy of gas-path stagnation temperature measurements. Firstly, attempts can be made to enhance probe measurement performance through better design. This requires careful consideration of both the temperature sensor and the probe assembly. Secondly, probe measurement performance can be characterised in sufficient detail to allow the application of post-test corrections. This necessitates the development of detailed probe models, or the execution of probe aerodynamic calibrations.

8.2.2 Probe aerodynamic calibration facility

To facilitate the investigation of stagnation temperature probe performance, an aerodynamic calibration facility has been created as part of this work. This facility incorporates an existing high-pressure nozzle test rig, which generates flows with stagnation pressures up to $8\,bar$ at stagnation temperatures close to ambient. Two different configurations for the facility working section have been developed for the purpose of this work. In the first configuration, the nozzle issues directly into the laboratory under atmospheric static pressure conditions. This allows an assessment of probe temperature recovery performance as a function of jet Mach number. In the second configuration, the nozzle issues into a confinement tube that operates at elevated static pressure conditions ($\leq 4\,bar$). This enables variations in Reynolds number to be considered in addition to jet Mach number. Together, these two working section configurations facilitate the aerodynamic calibration of stagnation temperature probes at Mach and Reynolds numbers that are representative of the gas-path between the inlet and intermediate pressure

compressor of a gas turbine engine.

In order to establish the facility operating conditions, systems for the measurement of flow pressure and temperature have also been developed as part of this work. The pressure measurement system utilises a Pitot tube to monitor jet stagnation pressure, as well as a working section tapping to monitor nozzle-exit static pressure. These measurements are used to determine the jet Mach number using isentropic relations. The temperature measurement system employs a bespoke passively ventilated thin-film PRT probe that monitors jet stagnation temperature. This probe has been specifically designed to pass flow over the sensor at a sufficiently low velocity ($\leq$ Mach 0.25) to negate temperature recovery effects. Accordingly, the indicated temperature provides an accurate reference against which to assess the performance of a probe under test.

8.2.3 Measurement uncertainty analysis

To establish confidence in results obtained from the probe aerodynamic calibration facility, a detailed uncertainty analysis has been performed. The first stage of this analysis has involved estimating the random and systematic uncertainties associated with each measured variable. The random uncertainty has been calculated using the standard deviation of a measurement sample comprised of the results of repeat static calibrations. A factor of 2 has been applied to the standard deviation to yield a 95 % confidence estimate. The systematic uncertainty has been computed from the root-sum-square of three individual systematic uncertainty components. These individual components relate to the static calibration procedure, the probe installation within the test environment and experimental approximation. Each uncertainty has been estimated at 95 % confidence, us-

ing data from manufacturer specifications, analytical calculations and previous experimental experience.

The second stage of the uncertainty analysis has involved estimating the random and systematic uncertainties associated with each derived experimental result. This has been accomplished using the Taylor series method of uncertainty propagation. The Taylor series method impresses the effect of individual measurement uncertainties on a derived result using an appropriate data reduction equation. The random and systematic uncertainties established using this method have subsequently been combined to yield an expanded uncertainty estimate for each experimental result. Under typical operating conditions, expanded uncertainties of 3.634×10^{-3} and 3.882×10^{-3} have been calculated for jet Mach number and probe temperature recovery factor, respectively. These values constitute 95 % confidence estimates of the overall error in the two most commonly reported aerodynamic calibration results.

8.2.4 Temperature sensor performance

Temperature sensor performance has been recognised as an important factor in determining the accuracy of measurements obtained from stagnation temperature probes. Traditionally, temperature sensing in gas turbine engines has relied on the extensive use of thermocouples. Thermocouples suffer from a range of problems that place limitations on the realisable measurement accuracy. These include errors introduced by the reference junction, signal corruption caused by electrical noise and static calibration drift induced by exposure to high temperature and stress. As an alternative, consideration has been given to the use of thin-film PRTs for temperature sensing in gas turbine engines. In certain applica-

tions, thin-film PRTs are known to offer a relative improvement in measurement accuracy compared to thermocouples. This is due to elimination of the reference junction, low sensitivity to electrical noise and reduced susceptibility to calibration drift. However, the maximum operating temperature of thin-film PRTs (typically $\leq 673\,K$) must restrict their application to low temperature regions of a gas turbine engine.

To evaluate the suitability of thin-film PRTs for use in gas turbine engines, two preliminary investigations have been performed. The first investigation has considered sensor calibration retention over a period of four months. This study has revealed a maximum temperature deviation of $0.015\,K$, signifying excellent stability and repeatability. The second investigation has studied the response of the sensor to engine representative vibration levels. This study has indicated little sensitivity to vibration, with a maximum temperature deviation of $0.014\,K$ after 9 hours of exposure. Based on these two results, the application of thin-film PRTs has been recommended in high accuracy probes, intended for use in low temperature ($\leq 673\,K$) regions of a gas turbine engine.

8.2.5 Probe temperature recovery performance

Probe temperature recovery performance has also been recognised as an important factor in determining the accuracy of stagnation temperature measurements. To account for temperature recovery effects, post-test corrections have traditionally been applied to stagnation temperature measurements using probe temperature recovery factors. However, these corrections are associated with uncertainties that are known to compromise the accuracy of the corrected temperatures. In order to realise high measurement accuracy, the necessary level of measurement

correction must therefore remain small. This requires the probe to be designed to deliver high temperature recovery performance ($R_{p,T} \approx 1$).

Using the aerodynamic calibration facility, two investigations have been conducted to determine the temperature recovery performance of stagnation temperature probes that incorporate thin-film PRT sensors. The first investigation considered a stainless-steel probe, similar to the passively ventilated thermocouple probes commonly used in gas turbine engines. This probe displayed relatively low temperature recovery factors ($0.85 \leq R_{p,T} \leq 0.89$) that varied with both Mach and Reynolds number condition. The second investigation considered a similar probe manufactured from acrylic. This probe exhibited comparatively higher temperature recovery factors ($R_{p,T} \approx 0.97$) that remained approximately constant with both Mach and Reynolds number condition. These results indicate that measurements acquired from the acrylic probe require smaller post-test corrections compared to measurements acquired from the stainless-steel probe. Since small corrections are associated with low levels of uncertainty, the acrylic probe has been identified as the more suitable of the two devices for high accuracy measurement applications.

The improved temperature recovery performance demonstrated by the acrylic probe has been attributed to reduced sensitivity to thermal conduction effects. Stainless-steel bodied (conventional) probes are known to experience conductive heat loss from the temperature sensor, driven by a thermal gradient between warmer gas ($T \approx T_{0,\infty}$) surrounding the sensor and cooler gas ($T \ll T_{0,\infty}$) flowing over the outer surfaces of the stagnation tube. This conductive heat loss reduces the temperature indicated by the sensor, resulting in a low probe temperature recovery factor. The acrylic bodied probe experiences comparatively less conductive heat loss from the temperature sensor, since the stagnation tube has a lower

thermal conductivity. Accordingly, the sensor indicates an increased temperature that corresponds to a higher probe temperature recovery factor. Based on this reasoning, there is confidence that the high temperature recovery performance demonstrated by the acrylic probe can be replicated with alternative low thermal conductivity stagnation temperature probe designs. Such designs require further investigation, since material limits (including temperature and strength) prevent the use of acrylic probes in gas turbine engines.

8.2.6 New dual-skin PRT probes

The findings of the investigations into sensor measurement performance and probe temperature recovery performance have been used to inform the design of a new stagnation temperature probe that is intended to achieve an absolute measurement uncertainty close to $\pm 0.1\%$. This new probe features a thin-film PRT sensor and a low thermal conductivity stagnation tube. A thin-film PRT sensor has been selected for its excellent static calibration retention and low sensitivity to electrical noise. A low thermal conductivity stagnation tube has been chosen to limit the detrimental impact of sensor conductive heat loss on probe temperature recovery performance. This has been achieved with a double-walled stagnation tube arrangement, in which an annular passage is formed between the sensing chamber and the outer probe body. The annular passage is filled with near-stagnated gas ($T \approx T_{0,\infty}$), which acts to restrict thermally conducting paths around the temperature sensor. This double-walled arrangement has lent its name to the new probe design, which is known as the dual-skin PRT probe.

To evaluate the performance of the dual-skin PRT probe, a series of investigations have been conducted using the probe aerodynamic calibration facility. These in-

vestigations have considered sensitivity to jet Mach and Reynolds number, as well as the influence of probe installation arrangement and flow incidence angle. The probe exhibited a high temperature recovery factor ($R_{p,T} \approx 0.96$) that remained appropriately constant over the range of conditions tested. These performance characteristics render the dual-skin PRT probe ideal for high accuracy measurement applications. The high temperature recovery factor implies that a low level post-test measurement correction is required. This benefits the accuracy of the corrected stagnation temperature, since the uncertainty introduced by the measurement correction remains small. The consistent probe temperature recovery performance also implies that a single recovery factor may be used to correct measured temperature data. This has two particular benefits. Firstly, uncertainties will no longer arise from the interpolation of the aerodynamic calibration curve. Secondly, the range of the probe aerodynamic calibration procedure may be restricted, resulting in considerable reductions in complexity, cost and time.

The suitability of the dual-skin PRT probe for conversion into a combined stagnation temperature and pressure measurement device has also been considered. This has involved the addition of a Pitot tube to the annular passage that is formed between the sensing chamber and the outer probe body. Since this passage is continuously purged with near-stagnated gas from the sensing chamber, the Pitot tube can register a pressure that is close to the stagnation pressure. However, this requires minimal pressure loss to be sustained as gas travels through the probe head. In order to identify the probe design features that are necessary to minimise pressure loss, a series of design optimisation studies have been performed. These studies have considered the relative flow area between the vent hole arrays and the sensing chamber. This has led to the identification of two important geometric design criteria. Firstly, the area of the inner vent

hole array must be large compared to the sectional area of the sensing chamber ($A_2/A_1 \geq 5.12$). Secondly, the area of the outer vent hole array must be small compared to the sectional area of the sensing chamber ($A_3/A_1 \leq 0.38$). Based on these two criteria, an optimum design has been defined for a combination dual-skin PRT probe.

The pressure and temperature recovery performance of an optimised combination dual-skin PRT probe has been examined using the probe aerodynamic calibration facility. Tests have been conducted to evaluate sensitivities to jet Mach and Reynolds number, as well as the influence of probe installation arrangement and flow incidence angle. The optimised combination probe exhibited a high temperature recovery factor ($R_{p,T} \approx 0.96$) that remained approximately constant over the range of conditions tested. This result was comparable with the temperature recovery performance demonstrated by the temperature-only dual-skin PRT probe. The device can therefore be successfully adapted to provide simultaneous pressure and temperature measurements, without compromising temperature recovery performance. The optimised combination probe also displayed a high pressure recovery factor ($R_{p,P} \approx 0.95$) that was approximately invariant with test condition. However, this represented slightly inferior pressure recovery performance compared to a conventional Pitot probe ($R_{p,P} \approx 0.99$). In order to utilise the combination probe design, some pressure recovery performance must consequently be sacrificed.

8.3 Proposals for future work

The research presented in this thesis has resulted in numerous proposals for future work. Descriptions of these proposals are provided in sections 8.3.1 to 8.3.4.

8.3.1 High temperature probes

The present work has involved the development of a high accuracy stagnation temperature probe for application in low temperature ($\leq 390\,K$) regions of a gas turbine engine. These are the measurement locations in which the target absolute stagnation temperature uncertainty of $\pm 0.1\%$ is most difficult to achieve. Subsequent work should now focus on the development of a high accuracy probe for use in hotter regions of the engine. It is envisaged that the successful design of this probe will be complicated by the harsh local operating conditions. This will result in a very different probe design compared to that developed for low temperature measurement applications. For instance, the high temperature environment is likely to constrain the choice of temperature sensor to a thermocouple. Thermocouples are renowned for their susceptibility to measurement errors, caused by phenomena including static calibration drift and electrical noise contamination. The magnitude of these errors must be reduced for high measurement accuracy to be attained. Additionally, provision for active cooling of the probe assembly may be necessary to ensure adequate service life. It is acknowledged that such cooling can adversely influence the probe indicated temperature, due to thermal conduction between the sensor and the probe body. To realise accurate measurements, the design of the probe must consequently limit conduction effects. Finally, consideration should be given to the radiant heat transfer that is driven by a temperature gradient between the sensor and the surroundings. This can have an important impact on the temperature indicated by the probe, particularly in a high temperature environment. Accordingly, the probe must be designed to restrict radiant effects in order to achieve high measurement accuracy.

8.3.2 Temporal measurement effects

The performance of stagnation temperature probes is typically studied under steady velocity and temperature conditions. However, these steady conditions are unrepresentative of the flows encountered by probes installed in a gas turbine engine. Probes are typically located behind rotating stages of turbomachinery, where the wakes shed from passing blades create an unsteady flow field. This unsteadiness is characterised by period fluctuations in velocity and temperature that persist at the blade passing frequency. It is typically assumed that stagnation temperature probes exposed to such unsteadiness will indicate the time average temperature of the flow. However, now that more accurate estimates of turbomachinery efficiency must be obtained, it is necessary to verify the validity of this assumption. This requires an investigation to be undertaken to evaluate the performance of stagnation temperature probes in flows with prescribed velocity and temperature fluctuations. It is proposed that this investigation could be performed experimentally, using a reconfigured version of the existing probe aerodynamic calibration facility. This would facilitate a comparison of probe performance in steady and unsteady flows with the same time average temperature. Any variation would indicate a relative measurement offset, which is currently overlooked when deriving turbomachinery efficiency estimates.

8.3.3 Spatial measurement effects

In a gas turbine engine, stagnation temperature probes are used to perform measurements at various axial locations that correspond to the main components of turbomachinery. At each axial location, probes are installed across the height of the engine annulus at selected radial locations. The discrete point measurements

acquired from these probes are typically combined to produce an estimate of the turbomachinery efficiency. However, now that the accuracy of this estimate must be improved, it is necessary to conduct a more detailed appraisal of the spatial temperature distribution. Unfortunately, to perform such an appraisal using solely experimental techniques would be practically difficult to achieve. Concerns over blockage effects limit the number of intrusive probe measurements that can be acquired, while access restrictions challenge the feasibility of non-intrusive acoustic and optical measurements. As a consequence, it is proposed that an approach utilising a combination of experimental and computational techniques should be explored. This combined approach would use computational data to establish the form of the spatial temperature distribution, and employ experimental data to determine the appropriate temperature magnitude.

8.3.4 Thermal conduction effects

It has been demonstrated that the performance of a stagnation temperature probe can be adversely affected by thermal conduction within the probe head. This driven by a temperature difference between near-stagnated ($T \approx T_{0,\infty}$) gas surrounding the sensor and high velocity gas ($T \ll T_{0,\infty}$) flowing over the outer surfaces of the probe. In an attempt to quantify the gas temperature close to the probe surface, an experiment has been conducted to measure the adiabatic wall temperature of a plain cylinder. This has revealed an axial variation in temperature, which is evidently related to regions of separated and attached flow. To develop an understanding of the fundamental physics that are responsible for this temperature variation, computational analyses of the flow field around a plain cylinder should be performed. These analyses are unlikely to be trivial, since accurate simulations of the leading edge impingement, separation and reattachment

will be difficult to achieve.

8.4 Closing remarks

During the development a gas turbine engine, work is carried out to determine the efficiency of the main components of turbomachinery. This involves measurements of the stagnation temperature at various locations within the gas-path. In the past, extensive engine development programs have delivered considerable gains in turbomachinery efficiency. Today, the remarkable success of these programs has placed limits on further realisable efficiency gains. As a consequence, engine manufacturers now require the capability to gauge small ($\leq 1\%$) increments of turbomachinery efficiency during engine test campaigns. To facilitate the assessment of small changes in turbomachinery efficiency, increases in the accuracy of stagnation temperature measurements are required. This raises questions regarding the measurement performance of the temperature sensor and the temperature recovery performance of the probe assembly. These factors presently constrain the achievable absolute stagnation temperature uncertainty to $\pm 0.5\%$.

Engine test experience has demonstrated that the fundamental measurement accuracy achievable with thermocouples is limited by problems including static calibration drift and signal corruption from electrical noise. As a consequence, consideration has been given to the use of thin-film PRTs for stagnation temperature measurements in low temperature ($\leq 673\,K$) regions of a gas turbine engine. Thin-film PRTs offer improved fundamental measurement accuracy compared to thermocouples, since they are inherently more stable and less sensitive to electrical noise. In addition, PRT measurements do not require a temperature reference junction, which contributes a further source of uncertainty to thermo-

couple measurements.

Initial experiments with a simple PRT probe have revealed that thermal conduction plays an important role in determining probe temperature recovery performance. Thermal conduction causes heat to be transferred away from the PRT sensor towards the relativity cold surfaces of the probe body. This reduces the probe indicated temperature to a value that is significantly below the *true* stagnation temperature of the flow. A substantial post-measurement correction is therefore necessary, which will result in a considerable increase in stagnation temperature uncertainty. In response to this problem, a new probe design has been developed that is intended to reduce the impact of thermal conduction effects. This probe features a double-walled arrangement, in which the PRT sensor is thermally isolated from the probe body using an annular passage filled with near-stagnated gas.

The performance of the double-walled PRT probe has been investigated experimentally using the newly developed Loughborough University probe aerodynamic calibration facility. In these experiments, the probe has exhibited two performance characteristics that promote high stagnation temperature accuracy. Firstly, the temperature recovery factor is sufficiently high ($R_{p,T} \approx 0.96$) that a low level of post-test measurement correction is required. This implies that uncertainties in the corrected stagnation temperature will remain small. Secondly, the temperature recovery factor is invariant with changes in Mach and Reynolds number, as well as flow incidence angle (up to 20^o) and installation arrangement (rake/sting). This reduces the uncertainty associated with the temperature recovery factor applied in the correction process.

In conclusion, an improvement in stagnation temperature accuracy can be re-

alised using the new double-walled PRT probe. This improvement is attributed to the fundamental measurement accuracy of the thin-film PRT sensor, as well as the high probe temperature recovery performance. These factors allow the absolute stagnation temperature uncertainty to approach the target value of $\pm 0.1\%$.

References

Anderson, J. D. (1990). *Modern compressible flow: With a historical perspective*, McGraw Hill Higher Education. 11, 129

Behrouzi, P. and McGuirk, J. (2010). Thermocouple probe calibration, *Technical report*, Loughborough University. xiv, 52, 54, 74

Behrouzi, P. and McGuirk, J. J. (2014). Underexpanded jet development from a rectangular nozzle with aft-deck, *AIAA Journal* pp. 1–12. 39

Benedict, R. P. (1984). *Fundamentals of temperature, pressure and flow measurements*, John Wiley & Sons. 105

Bentley, R. E. (1998a). *Handbook of Temperature Measurement Vol. 2: Resistance and Liquid-in-Glass Thermometry*, Vol. 2, Springer Science & Business Media. 86, 88

Bentley, R. E. (1998b). *Handbook of Temperature Measurement Vol. 3: The Theory and Practice of Thermoelectric Thermometry*, Vol. 3, Springer Science & Business Media. 21, 84

BIPM, I., IFcc, I. and IuPAc, I. (1995). Guide to the expression of uncertainty in measurement, *International Organization for Standardisation* pp. 92–67. 59

Callendar, H. L. (1887). On the practical measurement of temperature: Experiments made at the Cavendish Laboratory, Cambridge, *Philosophical Transactions of the Royal Society of London* pp. 161–230. 85

Childs, P., Greenwood, J. and Long, C. (2000). Review of temperature measurement, *Review of Scientific Instruments* **71**(8): 2959–2978. 22, 84, 85, 86, 87, 88

Chue, S. (1975). Pressure probes for fluid measurement, *Progress in Aerospace Sciences* **16**(2): 147–223. 75

Coleman, H. W. and Steele, W. G. (1995). Engineering applications of experimental uncertainty analysis, *The American Institute of Aeronautics and Astronautics Journal* **33**(10): 1888–1896. 59, 60, 62, 63, 64, 69, 77, 79

Dahl, A. and Fiock, E. (1949). Thermocouple pyrometers for gas turbines, *Transactions of the American Society of Mechanical Engineers* **71**: 153. 31

Dareck, M., Edelstenn, C., Ender, T., Fernande, E., Hartman, P., Herteman, J., Kerkloh, M., King, I., Ky, P., Mathieu, M. *et al.* (2011). Flightpath 2050: Europe's vision for aviation, *Report of the High Level Group on Aviation Research, European Commission* . 5

Dieck, R. H. (2007). *Measurement uncertainty: Methods and applications*, The International Society for Automation. 65, 78

Erlund, M. E. (2012). Advances in engine cold end temperature measurements, *European Virtual Institute for Gas Turbine Instrumentation*, number 010. ix, 89, 90, 91

Flock, E. F. (1953). The measurement of gas temperature by immersion-type instruments, *Journal of the American Rocket Society* **23**(3): 155–164. 32, 33

Folsom, R. G. (1955). Review of the pitot tube, *Technical report*, University of Michigan. 48, 74, 179

Gam, K., Yang, I. and Kim, Y.-G. (2011). Thermal hysteresis in thin-film platinum resistance thermometers, *International Journal of Thermophysics* **32**(11-12): 2388–2396. 86, 88

Gorton, R. E. (1969). Temperature measurement for aircraft-turbine-engine development, *Experimental Mechanics* **9**(5): 27N–34N. 29

Hottel, H. and Kalitinsky, A. (1945). Temperature measurements in high-velocity air streams, *Journal of Applied Mechanics* **12**(1): A25–A31. vii, 11, 24, 25

Kiel, G. (1935). Total-head meter with small sensitivity to yaw, *Technical report*, National Advisory Committee for Aeronautics. 13

King, W. (1943). Measurement of high temperatures in high-velocity gas streams, *Transactions of the American Society of Mechanical Engineers* **65**(5): 421. viii, 30, 31

Langley, M., Roberts, J., Leroux, A., Flohr, P., Brouckaert, J. and Zenkic, S. (2012). Sensors towards advanced control and monitoring of gas turbine engines, *Technical report*, European Commission. xiv, 15

Markowski, S. and Moffatt, E. (1948). Instrumentation for development of aircraft powerplant components involving fluid flow, *Technical report*, SAE International. 13, 37, 96

Massini, M., Miller, R. J., Hodson, H. P. and Collings, N. (2010). A novel technique for measuring stagnation quantities and gas composition in high temperature flows, *ASME Turbo Expo 2010: Power for Land, Sea, and Air*, American Society of Mechanical Engineers, pp. 223–233. 12

McAdams, W. H. (1954). *Heat transmission*, Vol. 3, McGraw-Hill New York. 27, 30, 32

Moffat, R. J. (1962). Gas temperature measurement, *Temperature: Its Measurement and Control in Science and Industry*, Vol. 1, p. 553. 20, 22, 24, 26, 27, 29, 30, 31, 32, 107

Moffat, R. J. (1988). Describing the uncertainties in experimental results, *Experimental Thermal and Fluid Science* **1**(1): 3–17. 63, 65, 69, 71, 76, 78

Moffatt, E. M. (1952). Multiple-shielded high-temperature probes: Comparison of experimental and calculated errors, *Technical report*, SAE International. 36

Mullikin, H. (1941). Gas-temperature measurement and the high-velocity thermocouple, *Temperature: Its measurement and control in science and industry* p. 775. viii, 28, 29, 108

Rolls-Royce (2005). *The Jet Engine*, Wiley-Blackwell. 4

Saravanamuttoo, H. (1990). Recommended practices for measurement of gas path pressures and temperatures for performance assessment of aircraft turbine engines and components, *Technical report*, Defense Technical Information Centre. viii, 12, 32, 34, 35, 88, 90, 128

Scadron, M. D., Gettelman, C. C. and Pack, G. J. (1950). *Performance of three high-recovery-factor thermocouple probes for room-temperature operation*, National Advisory Committee for Aeronautics. 32

Scadron, M. D., Warshawsky, I. and Gettelman, C. C. (1952). Thermocouples for jet-engine gas temperature measurement, *Proceedings of the American Institute of Physics* (52-12): 3. 15, 25, 28

Seebeck, T. (1823). Evidence of thermal current of the combination Ti-Cu by its action on magnetic needle, *Royal Academy of Science of Berlin* p. 265. 20, 83

Shaw, R. (1960). The influence of hole dimensions on static pressure measurements, *Journal of Fluid Mechanics* **7**(04): 550–564. 75

Simmons, F. S. (1957). Recovery corrections for butt-welded, straight-wire thermocouples in high-velocity, high-temperature gas streams, *Technical report*, National Aeronautics and Space Administration. 24

Stanworth, C. (1962). Suction pyrometers, *Proceedings of the Symposium on Some Developments in Techniques for Temperature Measurement*, Vol. 1. viii, 28, 33

Wilson, A., Ireland, P., Stevenson, R., Thorpe, S. and Martin, D. (2012). A robust radial traverse temperature probe for application to a gas turbine HP/IP stage, *ASME Turbo Expo 2012: Turbine Technical Conference and Exposition*, American Society of Mechanical Engineers, pp. 63–71. vii, viii, 27, 28, 36, 52, 53, 76

Zeisberger, A. (2007). Total temperature probes for turbine and combustor applications, *American Institute of Aeronautics and Astronautics* . 30, 36

APPENDIX A

Uncertainty Calculations

A.1 Introduction

This appendix documents the use of the Taylor series method to propagate uncertainties in experimentally measured variables to each of the experiential results derived for probe aerodynamic calibration (see section 4.4). In each case, the components of random and systematic uncertainty are dealt with separately, using the measurement uncertainties defined in Tables 4.4 and 4.8 respectively. The individual measurement uncertainties are specified at the typical experimental conditions outlined in Table 4.1, using a 95 % confidence limit. Accordingly, each propagated uncertainty corresponds to a 95 % confidence estimate of the error in the derived result, at these experimental conditions.

A.2 Free-stream Mach number

The free-stream Mach number may be established from measurements of the jet static and stagnation pressure, via equation 3.2. The propagation of random and systematic uncertainties from these measured variables to the derived result is illustrated in Figure A.1.

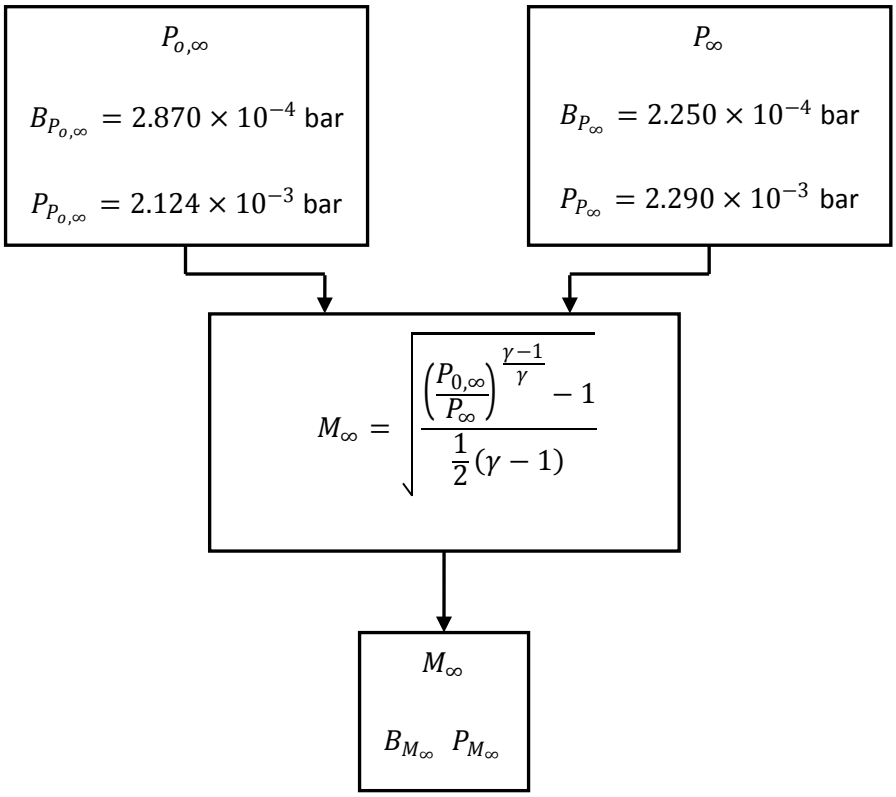

Figure A.1: Uncertainty propagation: Mach number.

Using the Taylor series method, the random and systematic uncertainties in the derived free-stream Mach number may be determined from equations A.1 and A.2.

$$P_{M_\infty}{}^2 = \sum_{i=1}^{2} \left(\frac{\partial M_\infty}{\partial X_i}\right)^2 P_i^2 = \left(\frac{\partial M_\infty}{\partial P_{o,\infty}}\right)^2 P_{P_{o,\infty}}{}^2 + \left(\frac{\partial M_\infty}{\partial P_\infty}\right)^2 P_{P_\infty}{}^2 \qquad \text{(A.1)}$$

$$B_{M_\infty}{}^2 = \sum_{i=1}^{2} \left(\frac{\partial M_\infty}{\partial X_i} \right)^2 B_i^2 = \left(\frac{\partial M_\infty}{\partial P_{o,\infty}} \right)^2 B_{P_{o,\infty}}{}^2 + \left(\frac{\partial M_\infty}{\partial P_\infty} \right)^2 B_{P_\infty}{}^2 \qquad \text{(A.2)}$$

The evaluation of these equations leads to the expressions represented by equations A.3 and A.4.

$$P_{M_\infty}{}^2 = \left(\frac{1}{2} \frac{\left[\left(\frac{P_{o,\infty}}{P_\infty} \right)^{\frac{\gamma-1}{\gamma}} - 1 \right]^{-1/2}}{\left[\frac{1}{2}(\gamma-1) \right]^{1/2}} \cdot \frac{\gamma-1}{\gamma} \cdot \left(\frac{P_\infty}{P_{o,\infty}} \right)^{\frac{1}{\gamma}} \cdot \frac{1}{P_\infty} \right)^2 P_{P_{o,\infty}}{}^2 + \left(-\frac{1}{2} \frac{\left[\left(\frac{P_{o,\infty}}{P_\infty} \right)^{\frac{\gamma-1}{\gamma}} - 1 \right]^{-1/2}}{\left[\frac{1}{2}(\gamma-1) \right]^{1/2}} \cdot \frac{\gamma-1}{\gamma} \cdot \left(\frac{P_\infty}{P_{o,\infty}} \right)^{\frac{1}{\gamma}} \cdot \frac{P_{o,\infty}}{P_\infty^2} \right)^2 P_{P_\infty}{}^2 \qquad \text{(A.3)}$$

$$B_{M_\infty}{}^2 = \left(\frac{1}{2} \frac{\left[\left(\frac{P_{o,\infty}}{P_\infty} \right)^{\frac{\gamma-1}{\gamma}} - 1 \right]^{-1/2}}{\left[\frac{1}{2}(\gamma-1) \right]^{1/2}} \cdot \frac{\gamma-1}{\gamma} \cdot \left(\frac{P_\infty}{P_{o,\infty}} \right)^{\frac{1}{\gamma}} \cdot \frac{1}{P_\infty} \right)^2 B_{P_{o,\infty}}{}^2 + \left(-\frac{1}{2} \frac{\left[\left(\frac{P_{o,\infty}}{P_\infty} \right)^{\frac{\gamma-1}{\gamma}} - 1 \right]^{-1/2}}{\left[\frac{1}{2}(\gamma-1) \right]^{1/2}} \cdot \frac{\gamma-1}{\gamma} \cdot \left(\frac{P_\infty}{P_{o,\infty}} \right)^{\frac{1}{\gamma}} \cdot \frac{P_{o,\infty}}{{P_\infty}^2} \right)^2 B_{P_\infty}{}^2 \qquad \text{(A.4)}$$

Based on the individual measurement uncertainties detailed in Figure A.1, these equations yield random (P_{M_∞}) and systematic (B_{M_∞}) uncertainties of 3.611 x 10^{-3} and 4.057 x 10^{-4} respectively. These values represent 95 % confidence estimates of the random and systematic errors in the free-stream Mach number.

A.3 Static temperature

To determine the temperature recovery factor for a probe under test, knowledge of the free-stream static temperature is required. This may be obtained from equation 3.1, using the free-stream Mach number and free-stream stagnation temperature. The propagation of random and systematic uncertainties from these two variables to the derived static temperature result is illustrated in Figure A.2.

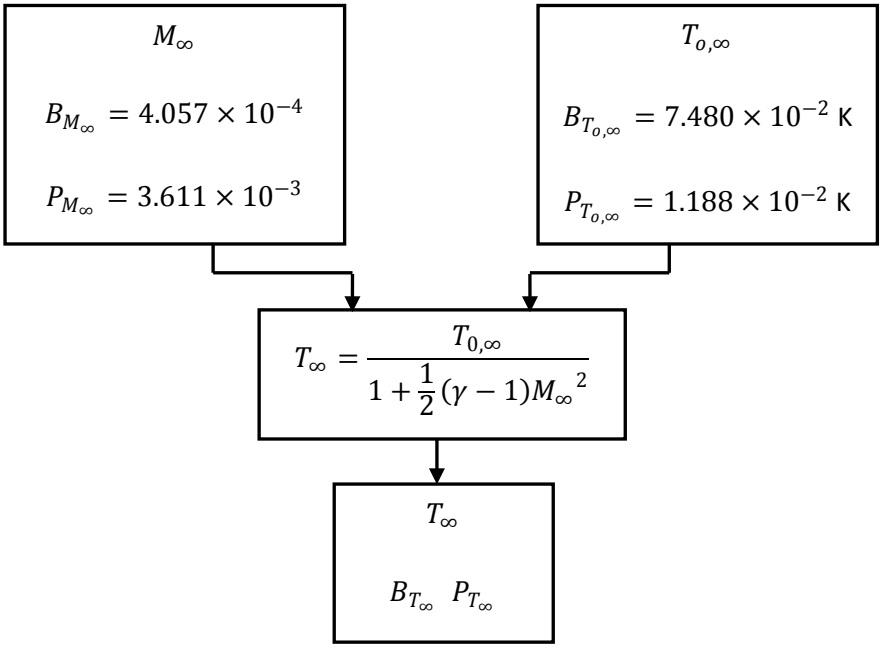

Figure A.2: Uncertainty propagation: Static temperature.

Using the Taylor series method, the random and systematic uncertainties associated with the free-stream static temperature may be ascertained from equations A.5 and A.6.

$$ {P_{T_\infty}}^2 = \sum_{i=1}^{2} \left(\frac{\partial T_\infty}{\partial X_i} \right)^2 P_i^2 = \left(\frac{\partial T_\infty}{\partial M_\infty} \right)^2 {P_{M_\infty}}^2 + \left(\frac{\partial T_\infty}{\partial T_{o,\infty}} \right)^2 {P_{T_{o,\infty}}}^2 \qquad \text{(A.5)} $$

$$B_{T_\infty}{}^2 = \sum_{i=1}^{2} \left(\frac{\partial T_\infty}{\partial X_i} \right)^2 B_i^2 = \left(\frac{\partial T_\infty}{\partial M_\infty} \right)^2 B_{M_\infty}{}^2 + \left(\frac{\partial T_\infty}{\partial T_{o,\infty}} \right)^2 B_{T_{o,\infty}}{}^2 \tag{A.6}$$

The evaluation of these equations leads to the expressions represented by equations A.7 and A.8.

$$P_{T_\infty}{}^2 = \left(\frac{-T_{o,\infty} (\gamma - 1) M_{o,\infty}}{\left[1 + \frac{1}{2} (\gamma - 1) M_{o,\infty}{}^2 \right]^2} \right)^2 P_{M_\infty}{}^2 + \left(\frac{1}{1 + \frac{1}{2} (\gamma - 1) M_{o,\infty}{}^2} \right)^2 P_{T_{o,\infty}}{}^2 \tag{A.7}$$

$$B_{T_\infty}{}^2 = \left(\frac{-T_{o,\infty} (\gamma - 1) M_{o,\infty}}{\left[1 + \frac{1}{2} (\gamma - 1) M_{o,\infty}{}^2 \right]^2} \right)^2 B_{M_\infty}{}^2 + \left(\frac{1}{1 + \frac{1}{2} (\gamma - 1) M_{o,\infty}{}^2} \right)^2 B_{T_{o,\infty}}{}^2 \tag{A.8}$$

Based on the individual measurement uncertainties detailed in Figure A.2, these equations yield random (P_{T_∞}) and systematic (B_{T_∞}) uncertainties of 2.176 x $10^{-1}\,K$ and 7.392 x $10^{-2}\,K$ respectively. These values correspond to 95 % confidence estimates of the random and systematic errors in the static temperature.

A.4 Probe temperature recovery factor

The probe temperature recovery factor may be determined from equation 2.4 using three key variables: the probe indicated temperature, the free-stream stagnation temperature and the free-stream static temperature. The propagation of random and systematic uncertainties from these variables to the derived result is illustrated in Figure A.3.

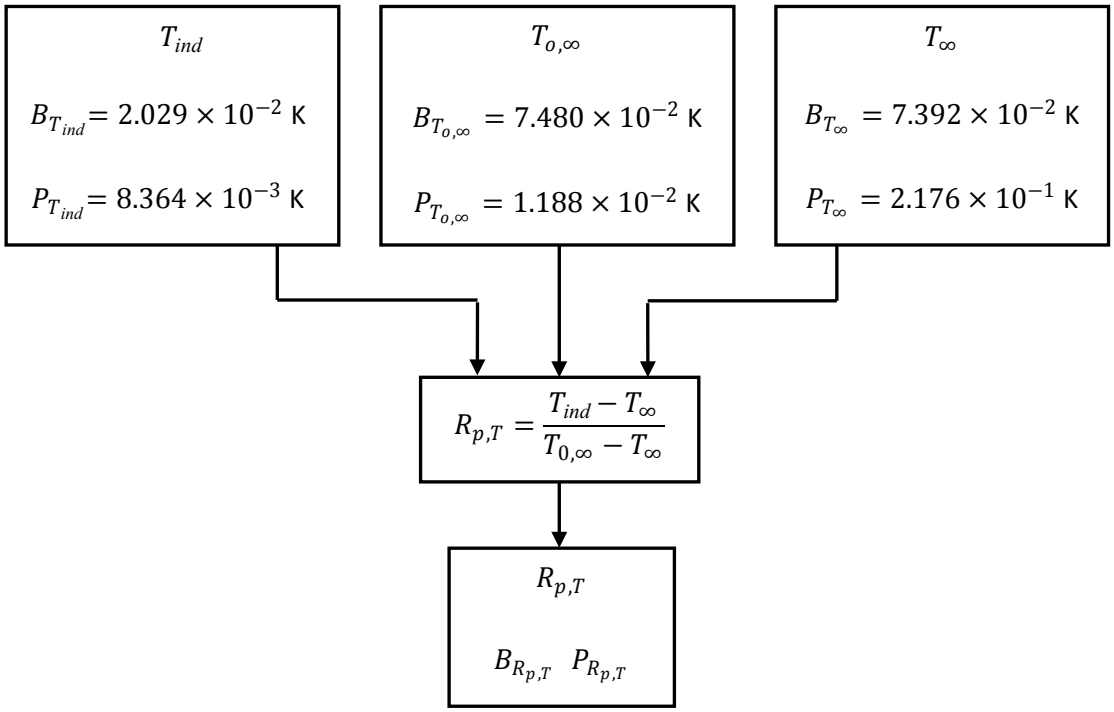

Figure A.3: Uncertainty propagation: Probe temperature recovery factor.

Using the Taylor series method, the random and systematic uncertainties in the probe temperature recovery factor may be established from equations A.9 and A.10.

$$P_{R_{p,T}}{}^2 = \sum_{i=1}^{3} \left(\frac{\partial R_{p,T}}{\partial X_i} \right)^2 P_i^2 = \left(\frac{\partial R_{p,T}}{\partial T_{ind}} \right)^2 P_{T_{ind}}{}^2 + \left(\frac{\partial R_{p,T}}{\partial T_{o,\infty}} \right)^2 P_{T_{o,\infty}}{}^2 + \left(\frac{\partial R_{p,T}}{\partial T_{\infty}} \right)^2 P_{T_{\infty}}{}^2 \tag{A.9}$$

$$B_{R_{p,T}}{}^2 = \sum_{i=1}^{3} \left(\frac{\partial R_{p,T}}{\partial X_i} \right)^2 B_i^2 = \left(\frac{\partial R_{p,T}}{\partial T_{ind}} \right)^2 B_{T_{ind}}{}^2 + \left(\frac{\partial R_{p,T}}{\partial T_{o,\infty}} \right)^2 B_{T_{o,\infty}}{}^2 + \left(\frac{\partial R_{p,T}}{\partial T_{\infty}} \right)^2 B_{T_{\infty}}{}^2 \tag{A.10}$$

The evaluation of these equations leads to the expressions represented by equations A.11 and A.12.

$$P_{R_{p,T}}{}^2 = \left(\frac{1}{T_{o,\infty} - T_\infty}\right)^2 P_{T_{ind}}{}^2 + \left(\frac{[T_\infty - T_{ind}]}{[T_{o,\infty} - T_\infty]^2}\right)^2 P_{T_{o,\infty}}{}^2 + \left(\frac{[T_{ind} - T_{o,\infty}]}{[T_{o,\infty} - T_\infty]^2}\right)^2 P_{T_\infty}{}^2 \tag{A.11}$$

$$B_{R_{p,T}}{}^2 = \left(\frac{1}{T_{o,\infty} - T_\infty}\right)^2 B_{T_{ind}}{}^2 + \left(\frac{[T_\infty - T_{ind}]}{[T_{o,\infty} - T_\infty]^2}\right)^2 B_{T_{o,\infty}}{}^2 + \left(\frac{[T_{ind} - T_{o,\infty}]}{[T_{o,\infty} - T_\infty]^2}\right)^2 B_{T_\infty}{}^2 \tag{A.12}$$

Based on the individual measurement uncertainties detailed in Figure A.3, these equations yield random ($P_{R_{p,T}}$) and systematic ($B_{R_{p,T}}$) uncertainties of 1.354 x 10^{-3} and 3.639 x 10^{-3} respectively. These values constitute 95 % confidence estimates of the random and systematic errors in the temperature recovery factor.

A.5 Probe pressure recovery factor

The probe pressure recovery factor may be determined from equations 3.3 and 3.4 using knowledge of the relative probe indicated pressure, the free-stream stagnation pressure and the free-stream static pressure. The propagation of random and systematic uncertainties from these measured variables to the pressure recovery factor result is illustrated in Figure A.4.

Using the Taylor series method, the random and systematic uncertainties in the probe pressure recovery factor may be determined from equations A.13 and A.14.

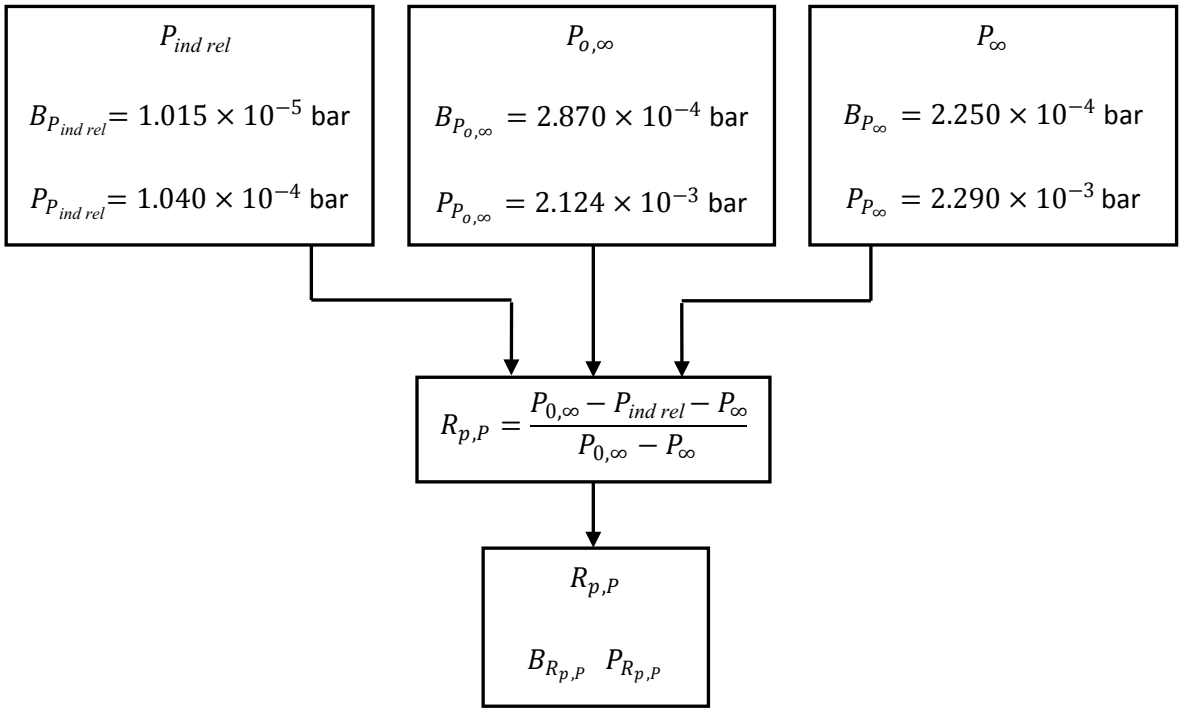

Figure A.4: Uncertainty propagation: Probe pressure recovery factor.

$$P_{R_{p,P}}{}^2 = \sum_{i=1}^{3} \left(\frac{\partial R_{p,P}}{\partial X_i}\right)^2 P_i^2 = \left(\frac{\partial R_{p,P}}{\partial P_{ind\,rel}}\right)^2 P_{P_{ind\,rel}}{}^2 + \left(\frac{\partial R_{p,P}}{\partial P_{o,\infty}}\right)^2 P_{P_{o,\infty}}{}^2 + \left(\frac{\partial R_{p,P}}{\partial P_{\infty}}\right)^2 P_{P_{\infty}}{}^2 \tag{A.13}$$

$$B_{R_{p,P}}{}^2 = \sum_{i=1}^{3} \left(\frac{\partial R_{p,P}}{\partial X_i}\right)^2 B_i^2 = \left(\frac{\partial R_{p,P}}{\partial P_{ind\,rel}}\right)^2 B_{P_{ind\,rel}}{}^2 + \left(\frac{\partial R_{p,P}}{\partial P_{o,\infty}}\right)^2 B_{P_{o,\infty}}{}^2 + \left(\frac{\partial R_{p,P}}{\partial P_{\infty}}\right)^2 B_{P_{\infty}}{}^2 \tag{A.14}$$

The evaluation of these equations leads to the expressions represented by equations A.15 and A.16.

$$P_{R_{p,P}}{}^2 = \left(\frac{-1}{P_{o,\infty} - P_\infty}\right)^2 P_{P_{ind\,rel}}{}^2 + \left(\frac{P_{ind\,rel}}{[P_{o,\infty} - P_\infty]^2}\right)^2 P_{P_{o,\infty}}{}^2 + \left(\frac{-P_{ind\,rel}}{[P_{o,\infty} - P_\infty]^2}\right)^2 P_{P_\infty}{}^2 \tag{A.15}$$

$$B_{R_{p,P}}{}^2 = \left(\frac{-1}{P_{o,\infty} - P_\infty}\right)^2 B_{P_{ind\,rel}}{}^2 + \left(\frac{P_{ind\,rel}}{[P_{o,\infty} - P_\infty]^2}\right)^2 B_{P_{o,\infty}}{}^2 + \left(\frac{-P_{ind\,rel}}{[P_{o,\infty} - P_\infty]^2}\right)^2 B_{P_\infty}{}^2 \tag{A.16}$$

Based on the individual measurement uncertainties detailed in Figure A.4, these equations yield random ($P_{R_{p,P}}$) and systematic ($B_{R_{p,P}}$) uncertainties of 3.963 x 10^{-4} and 3.948 x 10^{-5} respectively. These values constitute 95 % confidence estimates of the random and systematic errors in the probe pressure recovery factor.

A.6 Free-stream Reynolds number

To determine the free-stream Reynolds number from equation A.17, knowledge of the free-stream velocity, density and viscosity is required. These parameters are described in sections A.6.1 to A.6.3.

$$Re_\infty = \frac{\rho_\infty d V_\infty}{\mu_\infty} \tag{A.17}$$

A.6.1 Velocity

The free-stream velocity may be established from equation A.18, based on the free-stream Mach number and free-stream static temperature. The propagation of random and systematic uncertainties from these variables to the derived result is illustrated in Figure A.5.

$$V_\infty = M_\infty \cdot \sqrt{\gamma R T_\infty} \tag{A.18}$$

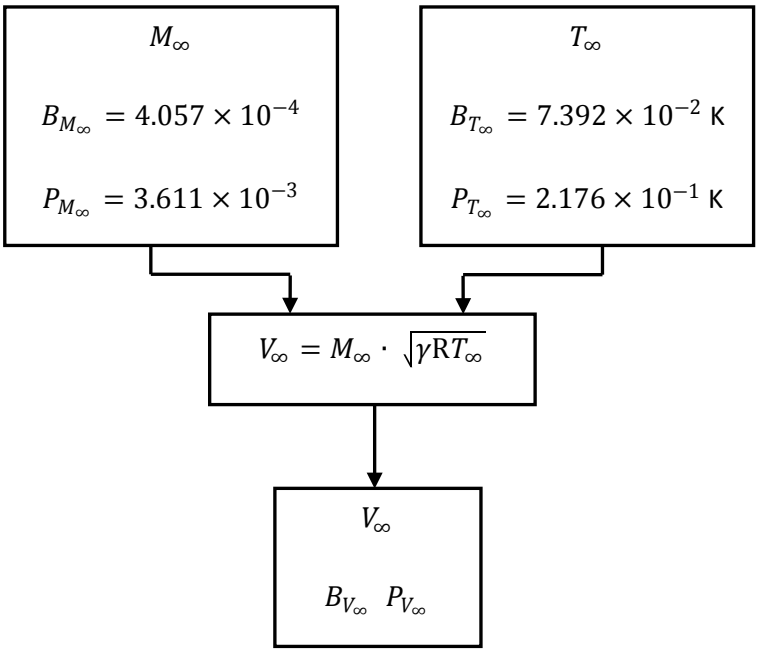

Figure A.5: Uncertainty propagation: Velocity.

Using the Taylor series method, the random and systematic uncertainties in the free-stream velocity may be determined from equations A.19 and A.20.

$$P_{V_\infty}{}^2 = \sum_{i=1}^{2} \left(\frac{\partial V_\infty}{\partial X_i} \right)^2 P_i^2 = \left(\frac{\partial V_\infty}{\partial M_\infty} \right)^2 P_{M_\infty}{}^2 + \left(\frac{\partial V_\infty}{\partial T_\infty} \right)^2 P_{T_\infty}{}^2 \tag{A.19}$$

$$B_{V_\infty}{}^2 = \sum_{i=1}^{2} \left(\frac{\partial V_\infty}{\partial X_i} \right)^2 B_i^2 = \left(\frac{\partial V_\infty}{\partial M_\infty} \right)^2 B_{M_\infty}{}^2 + \left(\frac{\partial V_\infty}{\partial T_\infty} \right)^2 B_{T_\infty}{}^2 \tag{A.20}$$

The evaluation of these equations leads to the expressions represented by equations A.21 and A.22.

$$P_{V_\infty}{}^2 = \left(\sqrt{\gamma R T_\infty} \right)^2 P_{M_\infty}{}^2 + \left(\frac{M_\infty \gamma R}{2\sqrt{\gamma R T_\infty}} \right)^2 P_{T_\infty}{}^2 \tag{A.21}$$

$$B_{V_\infty}{}^2 = \left(\sqrt{\gamma R T_\infty} \right)^2 B_{M_\infty}{}^2 + \left(\frac{M_\infty \gamma R}{2\sqrt{\gamma R T_\infty}} \right)^2 B_{T_\infty}{}^2 \tag{A.22}$$

Based on the individual measurement uncertainties detailed in Figure A.5, these equations yield random (P_{V_∞}) and systematic (B_{V_∞}) uncertainties of 1.189 m/s and 1.360 x 10^{-1} m/s respectively. These values correspond to 95 % confidence estimates of the random and systematic errors in the free-stream velocity.

A.6.2 Density

The gas density may be determined from equation A.23, using knowledge of the static pressure and temperature, alongside the specific gas constant ($R = 287\, J/kgK$). The propagation of random and systematic uncertainties from these variables to the derived result is illustrated in Figure A.6.

$$\rho_\infty = \frac{P_\infty}{R T_\infty} \tag{A.23}$$

Using the Taylor series method, the random and systematic uncertainties associ-

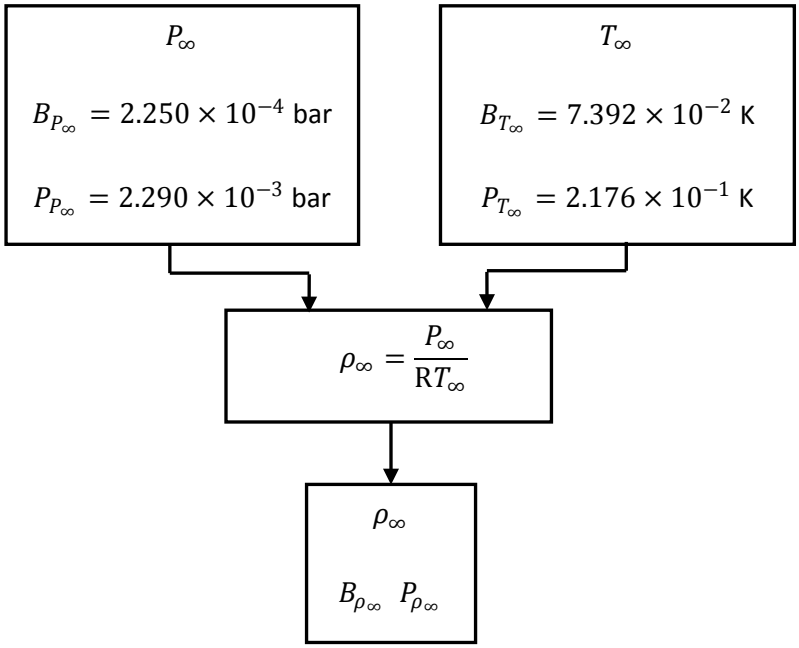

Figure A.6: Uncertainty propagation: Density.

ated with the derived result may be determined from equations A.24 and A.25.

$$P_{\rho_\infty}{}^2 = \sum_{i=1}^{2} \left(\frac{\partial \rho_\infty}{\partial X_i}\right)^2 P_i^2 = \left(\frac{\partial \rho_\infty}{\partial P_\infty}\right)^2 P_{P_\infty}{}^2 + \left(\frac{\partial \rho_\infty}{\partial T_\infty}\right)^2 P_{T_\infty}{}^2 \tag{A.24}$$

$$B_{\rho_\infty}{}^2 = \sum_{i=1}^{2} \left(\frac{\partial \rho_\infty}{\partial X_i}\right)^2 B_i^2 = \left(\frac{\partial \rho_\infty}{\partial P_\infty}\right)^2 B_{P_\infty}{}^2 + \left(\frac{\partial \rho_\infty}{\partial T_\infty}\right)^2 B_{T_\infty}{}^2 \tag{A.25}$$

The evaluation of these equations leads to the expressions represented by equations A.26 and A.27.

$$P_{\rho_\infty}{}^2 = \left(\frac{1}{RT_\infty}\right)^2 P_{P_\infty}{}^2 + \left(\frac{-P_\infty}{RT_\infty{}^2}\right)^2 P_{T_\infty}{}^2 \tag{A.26}$$

$$B_{\rho_\infty}{}^2 = \left(\frac{1}{RT_\infty}\right)^2 B_{P_\infty}{}^2 + \left(\frac{-P_\infty}{RT_\infty{}^2}\right)^2 B_{T_\infty}{}^2 \tag{A.27}$$

Based on the individual measurement uncertainties detailed in Figure A.6, these equations yield random (P_{ρ_∞}) and systematic (B_{ρ_∞}) uncertainties of 1.051 x $10^{-3}\,kg/m^3$ and 3.569 x $10^{-4}\,kg/m^3$ respectively. These values represent 95 % confidence estimates of the random and systematic errors in the gas density.

A.6.3 Viscosity

The gas viscosity may be established from equation A.28, using knowledge of the free-stream static temperature, alongside a number of pre-defined constants (μ_{ref}, T_{ref}, S). The propagation of random and systematic uncertainties from the static temperature to the derived viscosity result is illustrated in Figure A.7.

$$\mu_\infty = \mu_{ref}\left(\frac{T_\infty}{T_{ref}}\right)^{3/2} \cdot \left(\frac{T_{ref}+S}{T_\infty+S}\right) \tag{A.28}$$

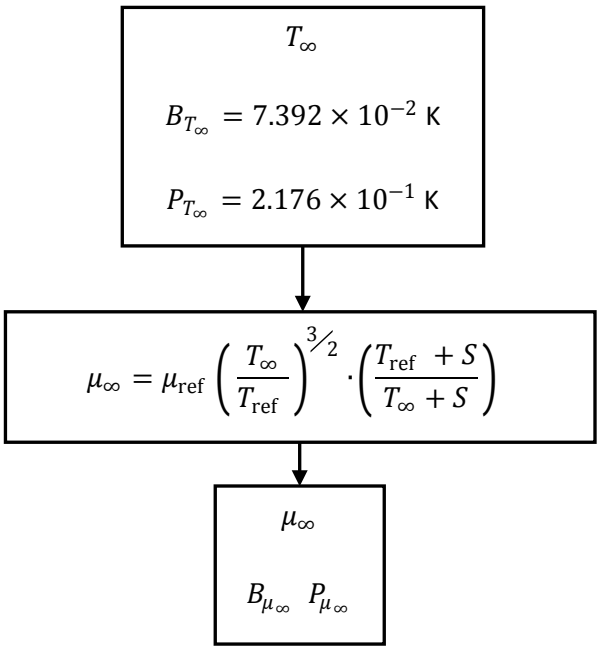

Figure A.7: Uncertainty propagation: Viscosity.

Using the Taylor series method, the random and systematic uncertainties in the derived result may be determined from equations A.29 and A.30.

$$P_{\mu_\infty}{}^2 = \sum_{i=1}^{1} \left(\frac{\partial \mu_\infty}{\partial X_i} \right)^2 P_i^2 = \left(\frac{\partial \mu_\infty}{\partial T_\infty} \right)^2 P_{T_\infty}{}^2 \tag{A.29}$$

$$B_{\mu_\infty}{}^2 = \sum_{i=1}^{1} \left(\frac{\partial \mu_\infty}{\partial X_i} \right)^2 B_i^2 = \left(\frac{\partial \mu_\infty}{\partial T_\infty} \right)^2 B_{T_\infty}{}^2 \tag{A.30}$$

The evaluation of these equations leads to the expressions represented by equations A.31 and A.32.

$$P_{\mu_\infty}{}^2 = \left(\left[\left(\frac{T_{ref} + S}{T_\infty + S} \right) \cdot \frac{3}{2} \cdot \mu_{ref} \cdot \left(\frac{T_\infty}{T_{ref}} \right)^{1/2} \cdot \frac{1}{T_{ref}} \right] - \left[\mu_{ref} \cdot \left(\frac{T_\infty}{T_{ref}} \right)^{3/2} \cdot \left(\frac{T_{ref} + S}{(T_\infty + S)^2} \right) \right] \right)^2 P_{T_\infty}{}^2 \tag{A.31}$$

$$B_{\mu_\infty}{}^2 = \left(\left[\left(\frac{T_{ref} + S}{T_\infty + S} \right) \cdot \frac{3}{2} \cdot \mu_{ref} \cdot \left(\frac{T_\infty}{T_{ref}} \right)^{1/2} \cdot \frac{1}{T_{ref}} \right] - \left[\mu_{ref} \cdot \left(\frac{T_\infty}{T_{ref}} \right)^{3/2} \cdot \left(\frac{T_{ref} + S}{(T_\infty + S)^2} \right) \right] \right)^2 B_{T_\infty}{}^2 \tag{A.32}$$

Based on the individual measurement uncertainties detailed in Figure A.7, these equations yield random (P_{μ_∞}) and systematic (B_{μ_∞}) uncertainties of 1.085 x $10^{-8}\, kg/ms$ and 3.687 x $10^{-9}\, kg/ms$ respectively. These values represent 95 % confidence estimates of the random and systematic errors in the gas viscosity.

A.6.4 Reynolds number

The random and systematic uncertainties that have been derived in sections A.6.1 to A.6.3 may now be used to establish the random and systematic uncertainties associated with the free-stream Reynolds number. This propagation of uncertainties is illustrated in Figure A.8

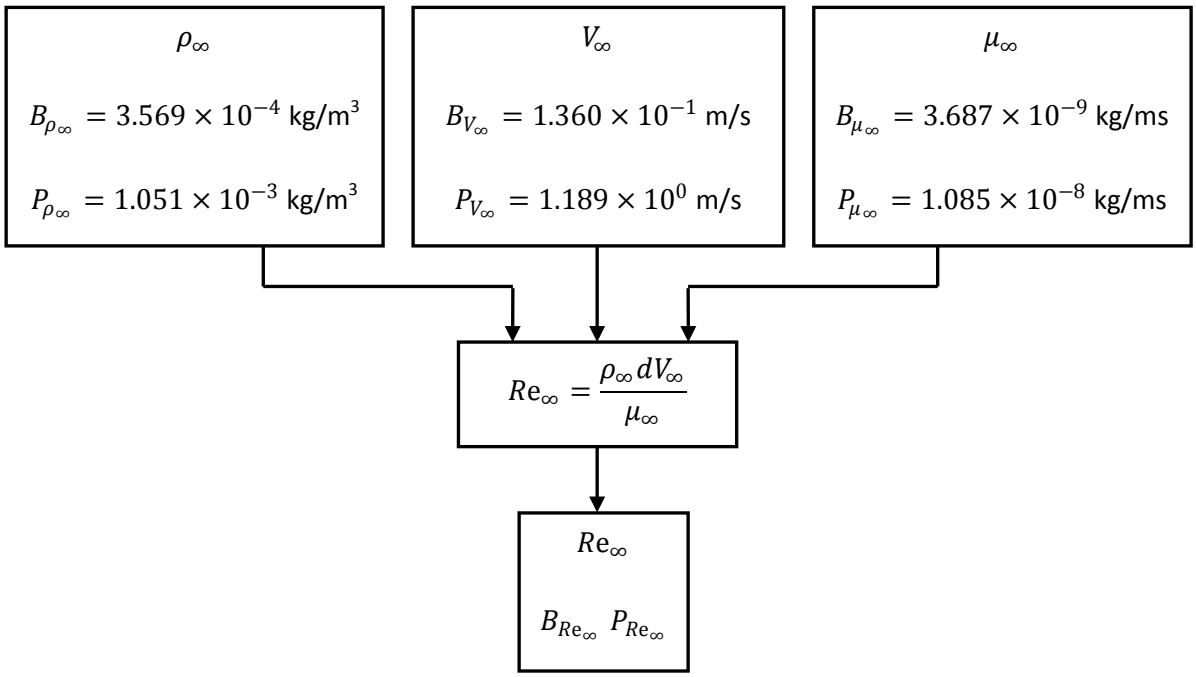

Figure A.8: Uncertainty propagation: Reynolds number.

Using the Taylor series method, the random and systematic uncertainties in the free-stream Reynolds number may be determined from equations A.33 and A.34.

$$P_{Re_\infty}{}^2 = \sum_{i=1}^{3} \left(\frac{\partial Re_\infty}{\partial X_i} \right)^2 P_i^2 = \left(\frac{\partial Re_\infty}{\partial V_\infty} \right)^2 P_{V_\infty}{}^2 + \left(\frac{\partial Re_\infty}{\partial \rho_\infty} \right)^2 P_{\rho_\infty}{}^2 + \left(\frac{\partial Re_\infty}{\partial \mu_\infty} \right)^2 P_{\mu_\infty}{}^2 \tag{A.33}$$

$$B_{Re_\infty}{}^2 = \sum_{i=1}^{3} \left(\frac{\partial Re_\infty}{\partial X_i} \right)^2 B_i^2 = \left(\frac{\partial Re_\infty}{\partial V_\infty} \right)^2 B_{V_\infty}{}^2 + \left(\frac{\partial Re_\infty}{\partial \rho_\infty} \right)^2 B_{\rho_\infty}{}^2 + \left(\frac{\partial Re_\infty}{\partial \mu_\infty} \right)^2 B_{\mu_\infty}{}^2 \tag{A.34}$$

The evaluation of these equations leads to the expressions represented by equations A.35 and A.36.

$$P_{Re_\infty}{}^2 = \left(\frac{\rho_\infty d}{\mu_\infty} \right)^2 P_{V_\infty}{}^2 + \left(\frac{d\, V_\infty}{\mu_\infty} \right)^2 P_{\rho_\infty}{}^2 + \left(\frac{-\rho_\infty d\, V_\infty}{{\mu_\infty}^2} \right)^2 P_{\mu_\infty}{}^2 \tag{A.35}$$

$$B_{Re_\infty}{}^2 = \left(\frac{\rho_\infty d}{\mu_\infty} \right)^2 B_{V_\infty}{}^2 + \left(\frac{d\, V_\infty}{\mu_\infty} \right)^2 B_{\rho_\infty}{}^2 + \left(\frac{-\rho_\infty d\, V_\infty}{{\mu_\infty}^2} \right)^2 B_{\mu_\infty}{}^2 \tag{A.36}$$

Based on the individual measurement uncertainties detailed in Figure A.8, these equations yield random (P_{Re_∞}) and systematic (B_{Re_∞}) uncertainties of 4.158 x 10^2 and 5.261 x 10^1 respectively. These values correspond to 95 % confidence estimates of the random and systematic errors in the free-stream Reynolds number.

APPENDIX B

Combination Dual-skin PRT Probe

This appendix contains the results of three sensitivity studies that have been conducted to investigate the pressure and temperature recovery performance of the optimised combination dual-skin PRT probe. The studies are essentially repetitions of those reported in section 7.2 for the temperature-only dual-skin PRT probe.

B.1 Incidence angle sensitivity

Figures B.1 and B.2 show the recovery performance of the optimised combination dual-skin PRT probe as a function of free-stream Mach number and flow incidence angle. This data has been gathered under atmospheric conditions ($T_{o,\infty} \approx 300\,K$ and $P_{\infty} \approx 1\,bar$), with the calibration facility operating in a free-jet configuration. The probe has been tested in a sting-mounted arrangement.

At zero flow incidence angle, the temperature recovery factor of the optimised combination dual-skin PRT probe varies between 0.95 and 0.97 over the Mach number range investigated. This is consistent with the performance reported for the temperature-only dual-skin PRT probe in section 7.2.1. However, the temperature recovery factor of the optimised combination dual-skin PRT probe exhibits some minor variation with flow incidence angle. This contrasts with the performance of the temperature-only dual-skin PRT probe, which remains constant at flow incidence angles up to approximately $20\,^{o}$. The explanation for this inconsistency is unknown.

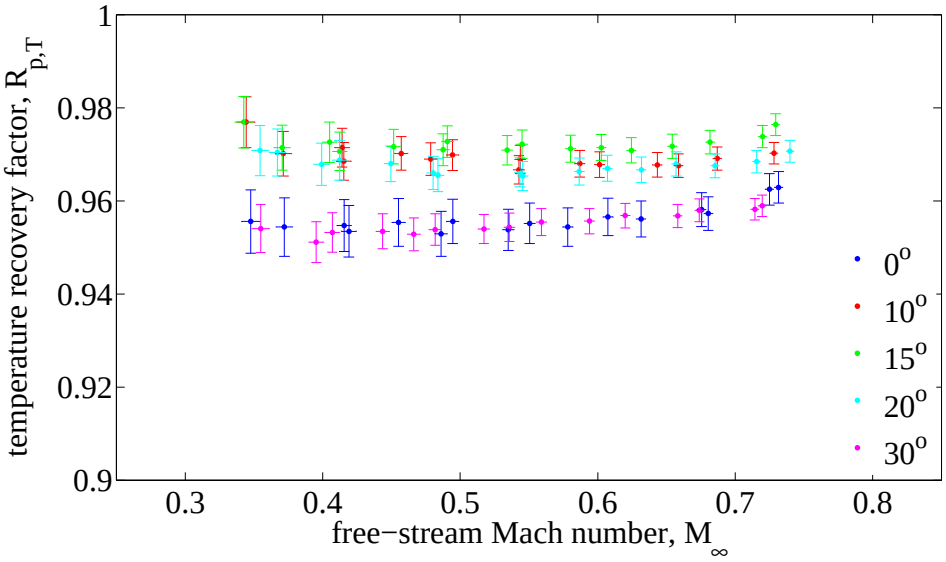

Figure B.1: Temperature recovery factor of the combination dual-skin PRT probe as a function of flow incidence angle and free-stream Mach number (sting-mounted, ambient static pressure).

At zero flow incidence angle, the pressure recovery factor of the optimised combination dual-skin PRT probe varies between 0.94 and 0.96 over the Mach number range investigated. This performance is maintained up to a flow incidence angle of approximately $15\,^{o}$, beyond which a reduction in the pressure recovery factor is observed. This range of angular insensitivity is consistent with that typically reported for Pitot probes (Folsom, 1955).

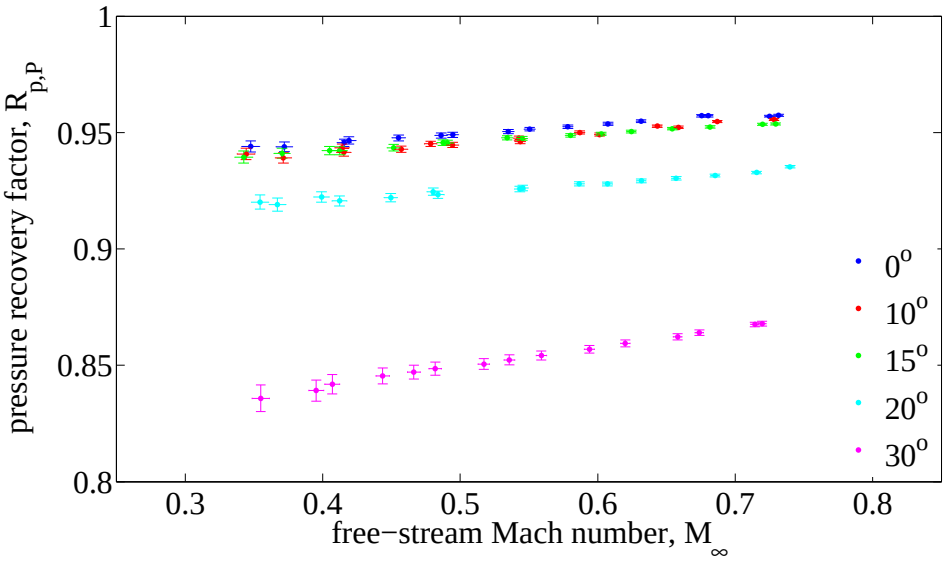

Figure B.2: Pressure recovery factor of the combination dual-skin PRT probe as a function of flow incidence angle and free-stream Mach number (sting-mounted, ambient static pressure).

B.2 Reynolds number sensitivity

Figures B.3 and B.4 show the recovery performance of the optimised combination dual-skin PRT as a function of free-stream Reynolds number. This data has been gathered with the calibration facility operating in an enclosed-jet configuration at atmospheric temperature conditions ($T_{o,\infty} \approx 300\,K$). Four different ratios of nozzle area to restrictor plate area have been utilised, corresponding to values of 0.03 (ambient static pressure), 0.64, 0.74 and 0.81. At each area ratio, the free-stream Mach number has been varied between values of 0.3 and 0.75. The probe has been tested in a sting-mounted arrangement, at zero flow incidence angle.

The temperature recovery factor of the optimised combination dual-skin PRT probe exhibits low sensitivity to free-stream Reynolds number, varying between values of 0.95 at $Re_\infty = 38,000$ and 0.97 at $Re_\infty = 160,000$. This result is

consistent with the performance of the temperature-only dual-skin PRT probe, which is reported in section 7.2.2.

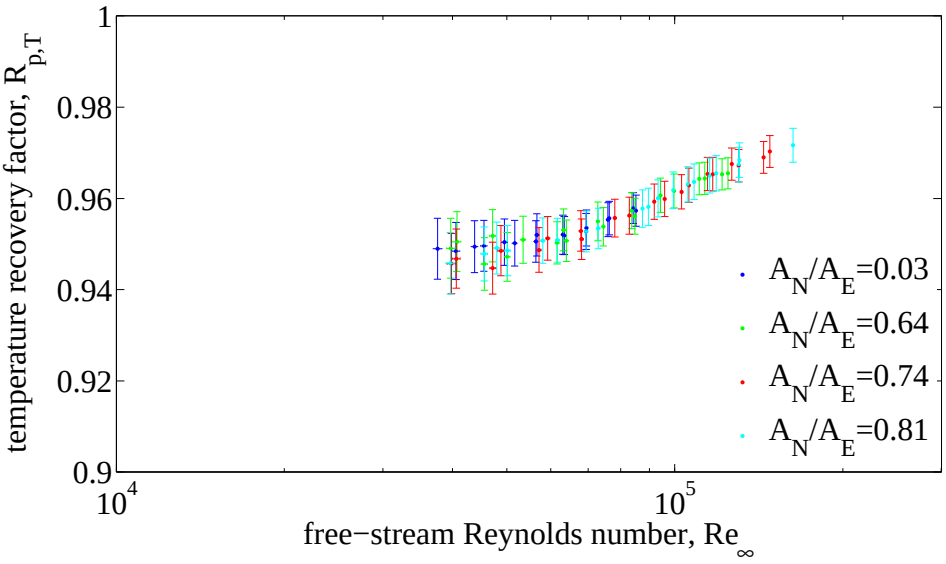

Figure B.3: Temperature recovery factor of the combination dual-skin PRT probe as a function of free-stream Reynolds number (sting-mounted, zero flow incidence angle, various static pressure conditions).

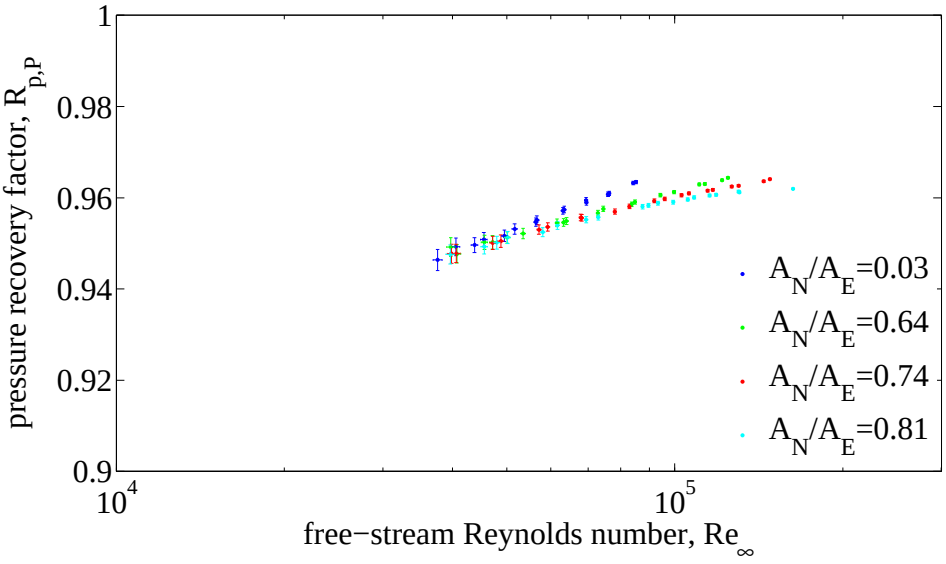

Figure B.4: Pressure recovery factor of the combination dual-skin PRT probe as a function of free-stream Reynolds number (sting-mounted, zero flow incidence angle, various static pressure conditions).

The pressure recovery factor of the optimised combination dual-skin PRT probe also exhibits low sensitivity to free-stream Reynolds number, varying between values of 0.94 at $Re_\infty = 38,000$ and 0.96 at $Re_\infty = 160,000$. However, at higher Reynolds numbers there is some discrepancy between the pressure recovery factors determined at different area ratio conditions. For a fixed Reynolds number of 100,000, temperature recovery factors of 0.96 and 0.95 are recorded at area ratios of 0.03 and 0.64 respectively. This result is indicative of a sensitivity to free-stream Mach number, since this is the primary distinction between the two measurement conditions. Confirmation of this sensitivity is provided by Figure B.5, which shows the data from Figure B.4 plotted as a function of free-stream Mach number. In this instance, the pressure recovery factors collapse on to a single line that is common to all area ratio conditions. This is a sensible outcome, since the probe pressure recovery performance is driven by velocity (Mach number) effects, not Reynolds number effects.

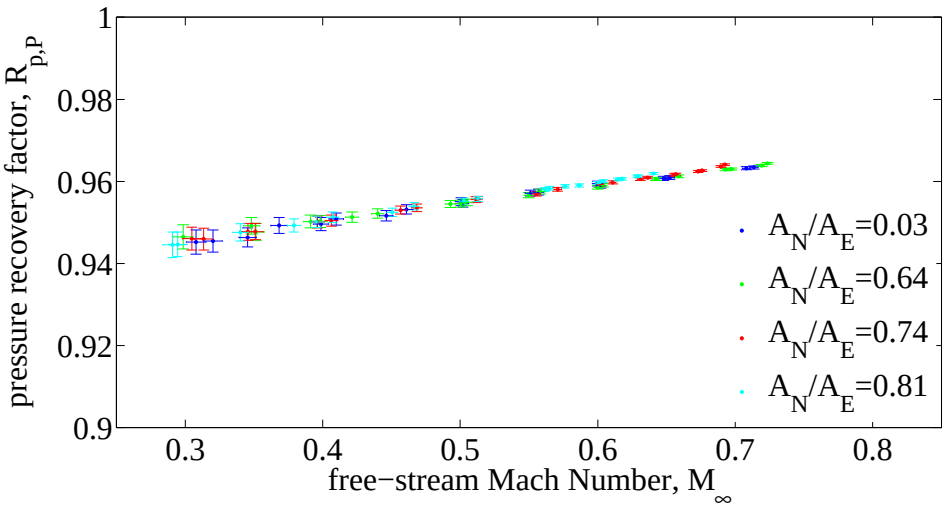

Figure B.5: Pressure recovery factor of the combination dual-skin PRT probe as a function of free-stream Mach number (sting-mounted, zero flow incidence angle, various static pressure conditions).

B.3 Probe installation sensitivity

Figures B.6 and B.7 show the recovery performance of the optimised combination dual-skin PRT probe in a rake-mounted arrangement. This data has been gathered under atmospheric conditions ($T_{o,\infty} \approx 300\,K$ and $P_{\infty} \approx 1\,bar$), with the calibration facility operating in a free-jet configuration. Five different probe protrusion lengths have been studied, corresponding to distances of 1.5, 3.0, 6.0, 9.0 and 12.0 mm from the rake leading edge. The probe has been tested at zero flow incidence angle.

For the various protrusion lengths tested, the temperature recovery factor of the optimised combination dual-skin PRT probe varies between 0.96 and 0.98. These values are comparable to the temperature recovery factors reported in section B.1 for the sting-mounted probe. Based on this result, the performance of the probe can be considered to be insensitive to installation arrangement. This insensitivity is consistent with the performance of the temperature-only dual-skin PRT probe, which is reported in section 7.2.3.

The pressure recovery factor of the optimised combination dual-skin PRT probe also exhibits low sensitivity to installation arrangement. For the various protrusion lengths tested, the pressure recovery factor varies between 0.94 and 0.97. These values are comparable to the pressure recovery factors reported in section B.1 for the sting-mounted probe. This result indicates that the performance of the probe is insensitive to aerodynamic installation effects.

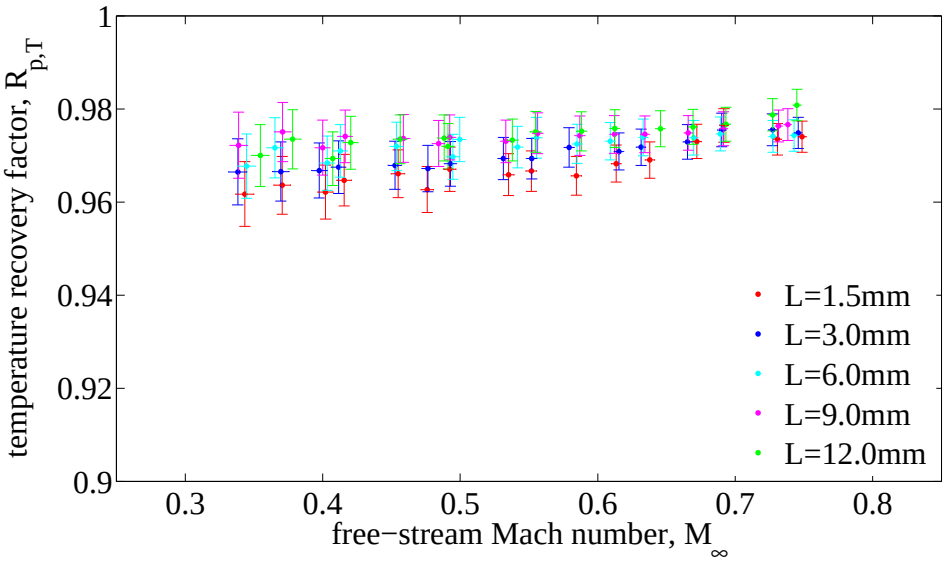

Figure B.6: Temperature recovery factor of the combination dual-skin PRT probe as a function of protrusion from the rake body and free-stream Mach number (rake-mounted, zero flow incidence angle, ambient static pressure).

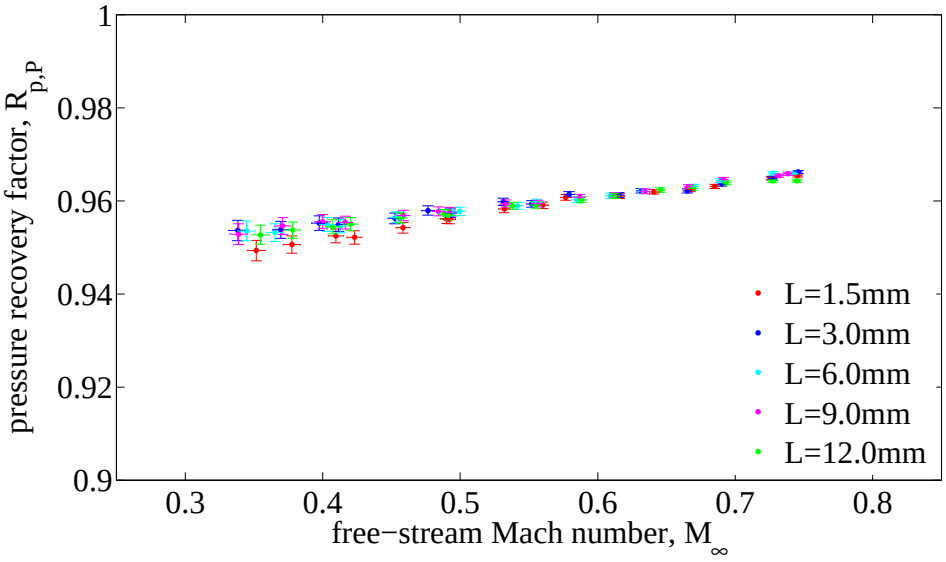

Figure B.7: Pressure recovery factor of the combination dual-skin PRT probe as a function of protrusion from the rake body and free-stream Mach number (rake-mounted, zero flow incidence angle, ambient static pressure).